INFORMATION TO USERS

This manuscript has been reproduced from the microfilm master. UMI films the text directly from the original or copy submitted. Thus, some thesis and dissertation copies are in typewriter face, while others may be from any type of computer printer.

The quality of this reproduction is dependent upon the quality of the copy submitted. Broken or indistinct print, colored or poor quality illustrations and photographs, print bleedthrough, substandard margins, and improper alignment can adversely affect reproduction.

In the unlikely event that the author did not send UMI a complete manuscript and there are missing pages, these will be noted. Also, if unauthorized copyright material had to be removed, a note will indicate the deletion.

Oversize materials (e.g., maps, drawings, charts) are reproduced by sectioning the original, beginning at the upper left-hand corner and continuing from left to right in equal sections with small overlaps.

Photographs included in the original manuscript have been reproduced xerographically in this copy. Higher quality 6" x 9" black and white photographic prints are available for any photographs or illustrations appearing in this copy for an additional charge. Contact UMI directly to order.

Bell & Howell Information and Learning
300 North Zeeb Road, Ann Arbor, MI 48106-1346 USA

UMI®
800-521-0600

Investigation of Unsteady Separated Flow and Heat Transfer Using Direct and Large Eddy Simulations

by

Anotai Suksangpanomrung
B.Eng., University of Cranfield, 1991
M.Sc., University of London, 1992
D.I.C., Imperial College of Science, 1992

A Dissertation Submitted in Partial Fulfillment of the
Requirements for the Degree of
DOCTOR OF PHILOSOPHY
in the
Department of Mechanical Engineering.

We accept this dissertation as conforming
to the required standard

Dr. N. Djilali, Supervisor (Department of Mechanical Engineering)

Dr. J. B. Haddow, Member (Department of Mechanical Engineering)

Dr. A. Suleiman, Member (Department of Mechanical Engineering)

Dr. A. J. Weaver, Outside Member (School of Earth and Ocean Sciences)

Dr. D. J. Bergstrom, External Examiner (University of Saskatchewan)

Supervisors: Dr. Ned Djilali

Abstract

This dissertation presents a numerical analysis of the separated flow and convective heat transfer around a bluff rectangular plate. This geometrically simple "prototype" configuration exhibits all the important features of complex separated and reattaching flow and has the advantage of well defined upstream conditions. The main objective of this work is the investigation of three-dimensional, high Reynolds number, unsteady separated flow using the large eddy simulation technique. However, two-dimensional and three-dimensional low and moderate Reynolds number simulations leading up to this are also of interest.

A staggered grid, finite volume method is used in conjunction with a third order Runge-Kutta temporal algorithm. The linear system for pressure is solved by, depending on the case, either a direct method or an efficient conjugate gradient with preconditioning. Two spatial discretizations are used, QUICK and CDS. In order to avoid the numerical diffusion effect from QUICK and dispersive effect from CDS, a mixed discretization is also introduced at high Reynolds number ($Re_d = 50,000$).

The two-dimensional steady and unsteady simulations are first presented. The predicted flow characteristics are in agreement with those reported in previous numerical studies. The two-dimensional unsteady simulations (Re_d = 1,000) provide good insight into the overall dynamic features of separation process, onset of instabilities and pseudo-periodic pattern of vortex formation, pairing and shedding. The realism of the simulation is however constrained by the artificially high coherence of the flow imposed by two-dimensionality.

The three-dimensional simulations provide a much improved representation of the flow. Three-dimensional instabilities are found to appear soon after the onset of the shear layer roll-up, and result in the rapid break-up of spanwise vortices. Convective heat transfer simulations highlighting the important role of large scale structures in enhancing turbulent transport are also presented.

At high Reynolds number, $Re_d = 50{,}000$, simulations are performed with three subgrid scale models. The selective structure function model, which allows improved localization, yields excellent agreement of the mean flow statistics with available experimental data. The dynamics of the flow is investigated using wavelet transform analysis and coherent structure identification. Characteristic frequencies related to shear layer instability, flapping and vortex shedding are identified consistent with experimental observation. The flow in the reattachment region is highly intermittent and characterized by a complex quasi-cyclic growth and bursting of the separation bubble, and horseshoe structures are identified in the recovery region of the flow.

Examiners:

Dr. N. Djilali, Supervisor (Department of Mechanical Engineering)

Dr. J. B. Haddow, Member (Department of Mechanical Engineering)

Dr. A. Suleman, Member (Department of Mechanical Engineering)

Dr. A. J. Weaver, Outside Member (School of Earth and Ocean Sciences)

Dr. D. J. Bergstrom, External Examiner (University of Saskatchewan)

Table of Contents

List of Tables

List of Figures

Nomenclature

A^+	Empirical constant for damping function
B	Empirical constant for law of the wall
Br	Blockage ratio, $Br = d/H$
C_{ij}	Cross stress tensor
C_f	Wall shear stress coefficient
C_k	Structure function constant
c_p	Specific of heat
C_p	Pressure coefficient
C_s	Smagorinsky constant
C_u	Advective velocity at outlet boundary
d	Thicknees of the plate
ds_i	Cell surface (ds_x, ds_y and ds_z)
dv	Cell volume
dx_i	Grid spacing between velocities nodes (dx, dy and dz)
dx_{ic}	Grid spacing around the leading edge corner(dx_c, dy_c and dz_c)
dx_{ip}	Grid spacing between scalar nodes (dx_p, dy_p and dz_p)
D	Damping function
f	Characteristic frequency
f_n	Nondimensional frequency, $f_n = fd/U_o$ or $f_n = f\overline{X}_r/U_o$
$\overline{F}_2$	Local structure function
G	Filter function
h_x	Local heat transfer coefficient
H	Height of the computational domain
k	Thermal conductivity
K	von Karman constant
L_d	The distance to the outlet boundary from the separation point
L_{ij}	Leonard stress tensor
L_u	The distance to the inlet boundary from the separation point
L_z	The spanwise dimension

Nu_x	Local Nusselt number, $Nu_x = h_x d/k$
Nu_x^*	Normalized mean local Nusselt number
Nu_m	Minimum of mean Nusselt number downstream of the leading edge
Nu_r	Maximum Nusselt number, $Nu_r = 0.0782 Re_d^{0.709}$
p	Local static pressure
$\overline{p}$	Filtered static pressure
$\overline{P}$	Filtered modified static pressure
P_o	Free stream static pressure
Pe	Local Pelet number
Pr	Prandtl number
Pr_t	Turbulent Prandtl number
$\dot{q}$	Constant heat flux
Re_d	Reynolds number based on thicknees of the plate, $Re_d = U_o d/\nu$
Re_l	Reynolds number based on the integral scale, $Re_l = U_o l/\nu$
R_{ij}	True subgrid scale Reynolds stress tensor
t	Time
T	Instantaneous temperature
T_o	Free stream temperature (293K)
T_w	Surface temperature
$\overline{T}$	Filtered temperature
$< u' >$	Root mean square of streamwise velocity fluctuation
u^+	Near-wall nondimensional velocity
u_τ	Friction velocity
$-< u'v' >$	Root mean square of turbulent shear stress
U_o	Free stream velocity
U_i	Instantaneous velocity components
$\overline{U}_i$	Filtered velocity components
x_i	Cartesian coordinate (x, y and z)
X_r	Reattachment length
$\overline{X}_r$	Mean reattachment length
y^+	Near-wall nondimensional vertical distance
y_c	The center of separated shear layer
y_e	The edge of separated shear layer

Greek Symbols

α	Thermal diffusivity
α_t	Thermal turbulent diffusivity
β	Angle between local vorticity and averaged-surrounding vorticity
Δ	Filter width
Δs_i	Local cell surface
Δv	Local cell volume
δ_{ij}	Kronecker delta, (= 1, for i = j; = 0, for 1 $\neq$ j)
ϵ	Dissipation rate
η	Kolmogorov (dissipation) scale
ζ	The selectivity option for the structure function model
θ	Dimensionless temperature, $\theta = (T - T_o)/(T_w - T_o)$
κ	The wavenumber
κ_d	The maximum wavenumber
κ_e	The wavenumber at maximum spectrum energy
l	Integral scale
λ	Eigenvalues
μ	Dynamic molecular viscosity
ν	Kinematic molecular viscosity
ν_t	Kinematic turbulent (eddy) viscosity
v	Velocity scale
ρ	Density
τ	Nondimensional time, $\tau = tU_o/d$
τ_{ij}	Subgrid scale stress tensor
τ_w	Wall shear stress
$\|\omega\|$	Absolute vorticity
ω_z	Spanwise vorticity

Acronynms

CDS	Central Differencing Scheme
CFD	Computational Fluid Dynamics
CG	Conjugate Gradient
DNS	Direct Numerical Simulation
EVM	Eddy Viscosity Models
LES	Large Eddy Simulation
MS	Multiple Scale
QUICK	Quadratic Interpolation for Convective Kinematics
RANS	Reynolds-Averaged Navier-Stokes equations
r.m.s.	Root mean square
RSM	Reynolds Stress Models
SGS	Subgrid Scale models
SM	Smagorinsky Model
SFM	Structure Function Model
SSFM	Selective Structure Function Model
VLES	Very Larged Eddy Simulation

Acknowledgements

I would like to express my sincere appreciation for the patient guidance and consistent encouragement of my supervisor, Dr. Ned Djilali. His friendship and generosity have been invaluable and have inspired me throughout the progress of my study.

I would also like to thank the members of my supervisory committee Dr. J. B. Haddow, Dr. A. Suleman, Dr. A. J. Weaver for their cooperation and assistance, and Dr. D. J. Bergstrom for his kind acceptance as an external examiner. Thanks are extended to Dr. Phillpe Moinat at CERFACES, and Dr. Henri-Claude Boisson at Institut de Mecanique des Fluides de Toulouse, Toulouse, France for their valuable input and discussion.

I would like to thank all my colleagues: Jon Pharoah, Goncalo Pedro, Glen Rutledge, Jean Neumann, Laurent Causse for their friendship and discussion. I give my appreciation to my wife Malinee Chatthai and family members for their moral support through rough times. Most importantly, I owe a debt of gratitude to my mother and father for their encouragement, confidence and unfailing affection.

I gratefully acknowledged the Royal Thai Army and the Natural Science and Engineering Research Council of Canada for financial support through scholarships and grants for this research.

Chapter 1

INTRODUCTION

Flows with large regions of separated and reattaching flows occur in a large variety of environments and engineering situations. These flows have a significant effect on the performance of, for example, heat exchangers, turbine blades, airfoils at higher angles of attack, microelectronic circuit boards and road vehicles. For instance, road vehicles must meet stringent fuel-consumption requirements which translate into a need for reduced aerodynamic drag, heat exchangers need to be designed and developed in order to operate more efficiently, i.e. provide higher heat flux and lower pressure drop. Several two-dimensional laboratory geometries have been devised to isolate particular parameters and investigate flow separation and reattachment. These include the backward and forward facing step, the rib, the fence and the bluff rectangular plate.

These complex flows are characterized by the large scale unsteadiness, complex turbulent structure, curvature effects and large pressure gradients. These features have been challenging to predict using many tools in experimental and numerical predictions including turbulence models. In order to study the main characteristics

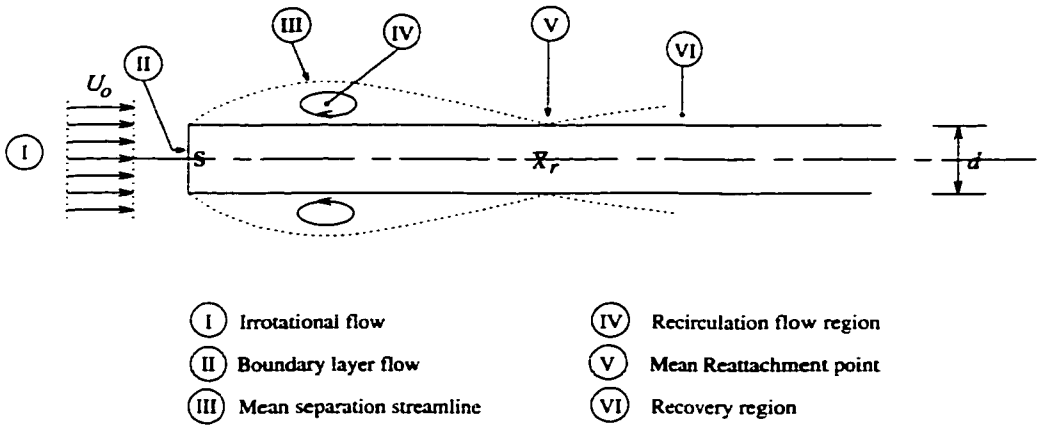

Figure 1.1: Schematic of the mean flow around a two-dimensional rectangular bluff plate

of separated and reattaching flows, the bluff rectangular plate was selected as a "prototype" geometry. This flow configuration simplifies the study of complex separated and reattaching flow. It has the advantage of some fixed and well defined parameters: the location of separation is fixed; the shear layer at separation is thin; and the upstream boundary conditions are simple and unambiguous.

The mean flow features of the flow around a bluff rectangular plate are sketched in Figure 1.1. As the uniform (irrotational) flow approaches the front of the plate, a boundary layer develops above and below the stagnation point, **S**. These boundary layers remain thin, due to the favourable (or negative) pressure gradient from the stagnation point to both sharp corners. Eventually, the flow separates from both corners, forming separated shear layers on the upper and lower sides of the plate. Due to the high curvature and spread rate of the separated shear layers, the flow eventually reattaches to the surfaces of the plate, forming a closed recirculating flow region or "separation bubble". Downstream of the mean reattachment point ($\overline{X}_r$), the flow recovers and forms a new boundary layer. For a sufficiently long plate, there

is no interaction between the upper and lower sides of the plate. Therefore, it is only necessary to consider half of the plate for numerical calculations.

1.1 Literature Review

1.1.1 Flow Over a Bluff Rectangular Plate

Previous experimental studies have shown that the flow over a bluff rectangular plate is strongly influenced by the following parameters: Reynolds number, nose shape, blockage ratio, aspect ratio, free stream turbulence intensity and length scale. The effect of Reynolds number and nose shapes were investigated by Ota *et al.* [1], using flow visualization in a water channel. They classified the flow into three regimes depending on the characteristic behaviors of the separated shear layer:

(i) The laminar separation and laminar reattachment regime, in which, in agreement with Lane and Loehrke [2], the reattachment length increases with the Reynolds number up to $Re_d \simeq 325$. This result was subsequently reproduced by two-dimensional steady numerical calculations [3].

(ii) The laminar separation and turbulent reattachment regime characterized by the appearance of shear layer instabilities (Kelvin-Helmholtz type instability) near separation, and transition to turbulence prior to reattachment, with the formation and shedding of large scale vortices. This regime was later reproduced in the numerical simulations of Tafti and Vanka [4], who performed two-dimensional simulations at $Re_d = 1{,}000$, and found that the reattachment point is not fixed but rather fluctuates about the mean value.

(iii) The turbulent separation and turbulent reattachment regime ($Re_d > 22{,}000$), in which the shear layer becomes turbulent almost immediately after separation. Reynolds number is found to have no effect on the mean reattachment length. To date, most experimental work has focused on this regime.

The effects of free stream turbulence and length scale were investigated experimentally by Hillier and Cherry [5]. They found that the mean flow characteristics such as the mean reattachment length ($\overline{X}_r$), the mean pressure etc. strongly depend on the turbulence intensity. The effect of turbulence length scale on mean pressure distribution and $\overline{X}_r$ in the separation bubble was negligible. However, an increase in turbulence length scale caused the pressure fluctuations to increase in the separation bubble. Similar results were obtained later by Kiya and Sasaki [6] and Saathoff and Melbourne [7]. Djilai and Gartshore [8] studied the effect of leading edge geometry (nose shape) on both mean pressure distribution and $\overline{X}_r$ and found that a decrease of separation angle induces an earlier pressure recovery and a shift of mean pressure distribution toward the leading edge with a corresponding shortening of $\overline{X}_r$.

A number of studies had examined the unsteady structure of the separation bubble formed on a bluff rectangular plate in a low turbulence stream [9, 10, 11, 12]. Results of these studies observed that the unsteady flow is dominated by the following phenomena:

- Throughout the separation bubble, the separated shear layer exhibits a low frequency flapping motion. This low frequency unsteadiness is most significant close to the separation point and appears to be an inherent feature of most separated and reattaching flow, (e.g., the backward facing step flow [13]). The

characteristic frequency ($f \approx 0.125\text{-}0.2U_o/\overline{X}_r$) is lower than those associated with the Kelvin-Helmholtz and the shear layer roll-up frequencies.

- In the reattachment region, the flow is characterized by large scale unsteadiness, pseudo-periodic bursting of the separation bubble, and irregular shedding of large scale vorticity. The average shedding frequency around the reattachment region was measured to be around $0.6\text{-}0.7U_o/\overline{X}_r$.

The structure of the large scale vortices in the reattachment zone was investigated by Kiya and Sasaki [14], who used a conditional sampling of the velocity field with surface pressure fluctuation as a conditioning signal. They concluded that these vortices have a hairpin shape with its ends lying in the $x - y$ plane and each end rotating in opposite direction.

Numerical simulations of this flow have also been performed and analyzed. An earlier two-dimensional simulation at Reynolds number of 1,000 [4], corresponding to the transitional regime, provided insight into the unsteady flow patterns which are difficult to observe experimentally. A subsequent three-dimensional direct numerical simulation (DNS) of the same case [15] clearly showed the importance of intrinsic three-dimensionality and successfully reproduced many aspects of the dynamic of the flow observed experimentally.

The only numerical prediction of the high Reynolds number flow (turbulent regime) was the Reynolds-Averaged Navier-Stokes (RANS) computation performed with a modified $k - \epsilon$ turbulence model [16]. These computations provided an adequate representation of the mean flow characteristics within the separation bubble, but a marked deterioration in the predictions was reported in the recovery region downstream of reattachment. The discrepancies were attributed to the complex turbulence

dynamics of the reattachment process and the associated large scale unsteadiness.

1.1.2 Heat Transfer Over a Bluff Rectangular Plate

The development and design of more efficient compact heat transfer devices has received much attention in recent years. Most investigations have focused on rectangular fins, which are commonly used in compact heat exchangers found in many applications, including electronic cooling modules, air conditioners, aircrafts and automobiles. Rectangular fins can be arranged in a variety of ways [17, 18, 19]. Most arrangements are affected by the complex formation of vortex patterns and their interactions, which significantly influence the prediction of heat transfer coefficients. Consequently, the long rectangular bluff plate has been preferred as a configuration for the understanding of the convection mechanisms and the prediction of heat transfer performance on rectangular fins.

Ota and Kon [20, 21] experimentally investigated heat transfer from a bluff rectangular plate, and found a 30-50% increase in the time averaged heat transfer rate in comparison with a turbulent boundary layer on a flat plate. Additionally, they found that the heat transfer coefficient drops from a sharp peak at the point of separation and then increases gradually, reaching a maximum near the time mean reattachment point. They concluded that the nose shape has a strong effect on the heat transfer characteristics in the separated and reattaching flow regions, but a correlation between the reattachment Nusselt number and the Reynolds number based on the reattachment length could be obtained independently of the nose shape.

Several experimental investigations have shown that enhanced heat(mass) transfer rates in the separated flow around a bluff rectangular plate could be obtained by

acoustic excitation or periodic perturbation of the flow field [22, 23, 24]. Substantial heat(mass) transfer augmentation was reported particularly around the reattachment region.

The convective heat and mass transport has also been the subject of several numerical studies. Djilali [3] performed two-dimensional simulations of the convective heat transfer over a stacked array of rectangular plates with different blockage ratios at low Reynolds number (laminar regime). The location of the maximum heat transfer coefficient was predicted to occur slightly downstream of the reattachment point and found to be strongly dependent on the blockage ratios. Tafti [25] performed a simulation of the transport of a passive scalar at $Re_d = 1{,}000$. The location of the maximum heat transfer coefficient was in agreement with [20, 26]. He analyzed the effect of coherent structures on scalar transport and concluded that these structures act as "large scale mixers".

Calculations of wall heat transfer coefficient in a high Reynolds number turbulent separation bubble ($20{,}000 < Re_d < 75{,}000$) were reported by Djilali *et al.* [27]. They examined the performance of seven near-wall turbulence models, and found that a three-layer wall function in conjunction with modified $k - \epsilon$ equations gave the best overall performance. This study showed that though flow field predictions are not very sensitive to the near-wall treatment, the accurate prediction of wall heat transfer rate is critically dependent on the representation of the low Reynolds number turbulence near the wall.

1.2 Turbulence and Coherent Structures

Most flows occurring in natural environments and in engineering practice are turbulent. Turbulent motion can be found in many applications such as meteorology, aerodynamics, oceanography, shipbuilding, and combustion, etc. The study of the complex and fascinating phenomena associated with turbulence has occupied many engineers and scientists for over a century since the pioneering work of Osborne Reynolds in 1883. Turbulence, however, is not a simple phenomena to be solved. Complete understanding and "universal" modelling of turbulence remain elusive, and this still remains the most difficult and important problem in fluid mechanics [28, 29].

From a computational view point, the most problematic aspect of turbulence is the wide range of turbulent eddy sizes. As in all fluid dynamic processes, the character of the flow is determined by the ratio between the inertial and viscous forces, i.e. the Reynolds number. As the Reynolds number increases, increasingly small turbulent eddies appear in the flow. This occurs via the energy cascade process in which the associated turbulent kinetic energy is extracted via the large eddies from the mean flow. This energy is gradually cascaded to smaller and smaller eddies due to the nonlinear interactions in the flow. Eventually, the turbulent kinetic energy is dissipated at the small scales (high frequencies) due to viscosity. A typical turbulent energy spectrum is shown in Figure 1.2.

The size and structure of the largest eddies depend on the flow condition and configuration (geometry). The medium-size eddies which contain the bulk of the total kinetic energy of turbulence are sometimes called "energy-containing eddies". The characteristic wavenumber for this range is denoted by κ_e. In the range $\kappa >> \kappa_e$, the eddies gain their energy by inertial transfer from the larger eddies and the amount

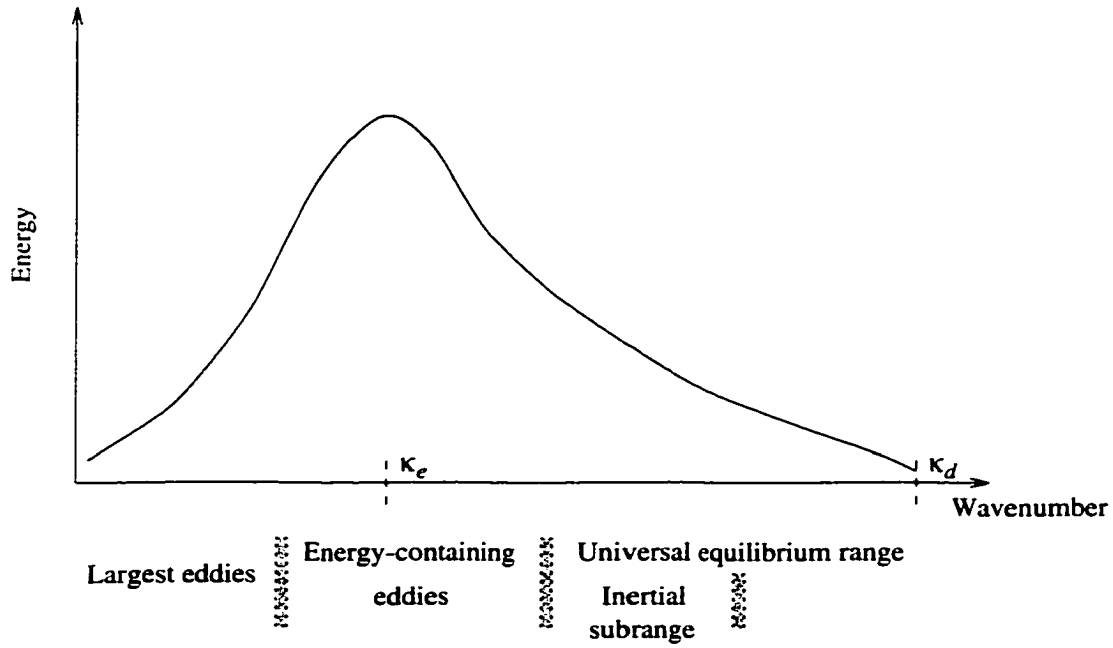

Figure 1.2: Schematic of three-dimensional spectrum in the various eddies (wavenumber) sizes

of energy transferred in this range is large compared with the rate of change of turbulent kinetic energy. So these eddies may consider to be in statistical equilibrium where the energy transferred is equivalent to the energy dissipated. This range is called "universal equilibrium range". In the universal equilibrium range, the dissipation increases strongly as the wavenumber increases. Therefore, at some subranges of equilibrium, the dissipation is considerably small and can be neglected when compared with the energy transferred by inertial effect. This subrange is called "inertial subrange", and it is statistically independent of the energy-containing eddies and the strong dissipation ranges ($\kappa_e << \kappa << \kappa_d$).

The characteristic of turbulence in the "universal equilibrium range" are determined by the parameters ϵ and ν, which can be used to construct the Kolmogorov

(dissipation) length (η) and velocity (v) scales.

Length scale:

$$\eta = \left(\frac{\nu^3}{\epsilon}\right)^{1/4} \tag{1.1}$$

Velocity scale:

$$v = (\nu\epsilon)^{1/4} \tag{1.2}$$

The smallest eddies (η) are very much smaller than the largest eddies, integral scale (l). The separation in both scales widens as the Reynolds number (based on the integral scale) increases, $\eta/l \sim Re_l^{3/4}$ [30]. For a flow with the same integral scale, the size of the smallest eddies for low Reynolds number flow is relatively coarse compared with the size in higher Reynolds number flow.

It has been shown that turbulent flows contain a *coherent structure*, repeatable and essentially quasi-deterministic events which are responsible for a large part of mixing. Such structures can be visualized in many turbulent flows such as the mixing layer, turbulent jet, wakes and boundary layers [31]. A distinction can be make between near-wall and core structures. An example of core structures are the large eddies usually associated with shear layer instability such as Kelvin-Helmholtz type instability [32], or "shedding" type instability. In near-wall region, the concept of coherent structures had lead to a detailed description and mechanism of the phenomena responsible for the production and the transport of turbulence. Typical coherent structures in near-wall region include hairpin (horseshoe) vortices, bursts and streaks. A conceptual model of near-wall structures is shown in Figure 1.3.

Hairpin vortices are generated by the U-shaped distortion of spanwise rolls periodically created by shear in the wall region. By self-induction, the leading edge of the

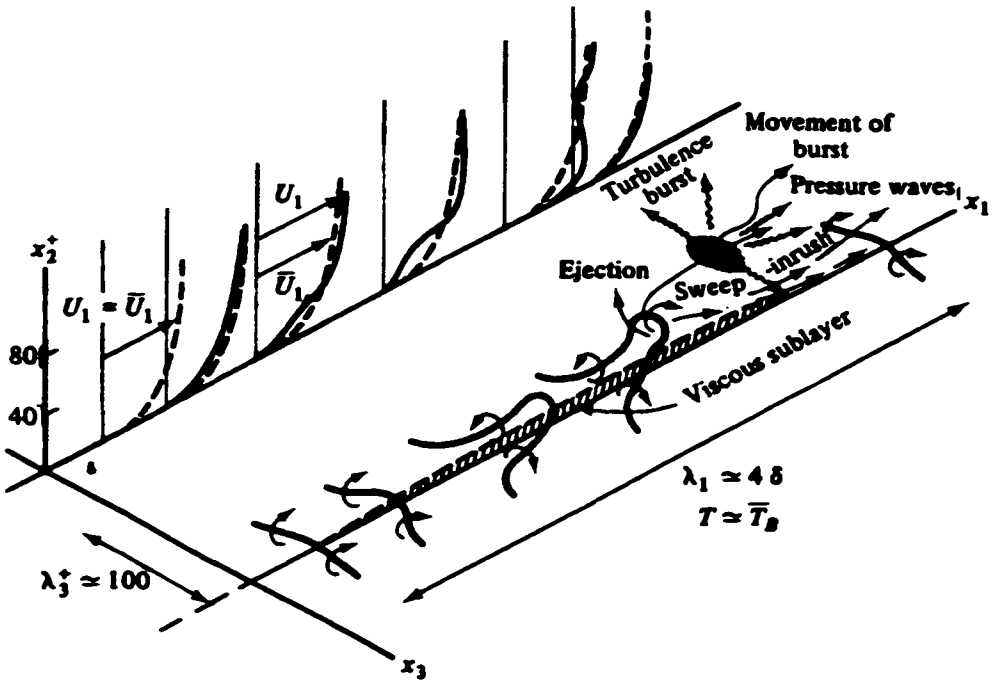

Figure 1.3: Conceptual model of near-wall turbulence structure; after Hinze [33]

U-shaped vortices tends to leave the wall. This in turn brings it into an outer (higher speed) region, resulting in a stretching of the vortex along the flow direction. The deformation proceeds until a breakdown of the vortex line occurs. This is associated with the sudden release of mechanical energy (turbulence burst) which is responsible for most of turbulence production at the wall. In the region confined between the two branches of a hairpin vortex, the streamwise velocity is relatively low and the fluid moves away from the wall. A classical review of this wall turbulence is given by Hinze [33]. In a real wall-bounded turbulent flow, several parallel hairpin vortices exist at any instant on a wall and a pattern of alternating high and low speed region (streak) is established. The existence of these structures had been experimentally confirmed by Kline [34].

1.3 Turbulence modelling, Direct and Large Eddy Simulations

The use of computational methods for predicting turbulent flows started in the sixties. The methods were based on the solution of the Reynolds-Averaged Navier-Stokes (RANS) equations in conjunction with turbulence models. The deficiencies of the turbulence models have however hampered progress in the application of computational methods to complex flows. Furthermore, RANS based methods can not be used as a tool for investigating the physics of complex turbulent flows. With increasing computational power and the development of efficient algorithms, researchers have turned to Direct Numerical Simulation (DNS) and Large Eddy Simulation (LES) in recent years. These computational methods are increasingly being used to investigate fundamental transport processes in turbulence, means of controlling it [35], and finally to help derive more accurate engineering turbulence models that are less costly and that can be used for routine engineering design and analysis.

1.3.1 Direct Numerical Simulation (DNS)

The most exact approach to turbulence simulation is to solve the continuity, Navier-Stokes, and energy equations directly in three-dimensional, time-dependent fashion without averaging or approximation to any turbulence transport process. In such simulations, all scales of motions contained in the flow, ranging from the smallest to largest scales, are resolved numerically. This is the direct numerical simulation (DNS) approach.

In order to solve the field equations directly, the computational domain has to

be at least as large as a few times the integral scale, in order to capture the largest eddies in the flows. The grid size has to be sufficiently small to capture the smallest eddies, which are of the order of Kolmogorov scale (η). As an example, DNS of a plane channel flow requires $\Delta x = 7.5\eta$, $\Delta y = 0.03\eta$, and $\Delta z = 4.4\eta$ [36]. As a rule of thumb, the number of grid points required by DNS has been estimated by Tennekes and Lumley [30] to be proportional to $Re_l^{9/4}$, where Re_l is the Reynolds number based on the integral scale and the r.m.s. velocity fluctuation.

The number of grid points for a simulation are limited by the processing speed, memory capacity, and data transmission of the machine, and DNS is hence only currently possible at low Reynolds number. The rapid development of computers has made it possible to perform DNS with $(512)^3$ grid points on massively parallel Connection Machine-5 [37]. However, the simulation is limited to simple flows. As the flow geometries become more complex, the requirement of computer capacities are necessary. Even with a sustained growth in computational speed and memory, DNS will not be a practical tool for high Reynolds number complex turbulent flow in the near future. An alternative that lies between DNS and classical RANS methods is large eddy simulation.

1.3.2 Large Eddy Simulation (LES)

LES basically consists of resolving directly the three-dimensional, time dependent turbulent motion associated with the larger eddies, while eddies of the order of the grid size and smaller are taken into account using a subgrid scale model.

The rationale for LES [38, 39, 40] is that the large eddies dominate the physics of any turbulent flow. They extract energy from the mean flow and are responsible

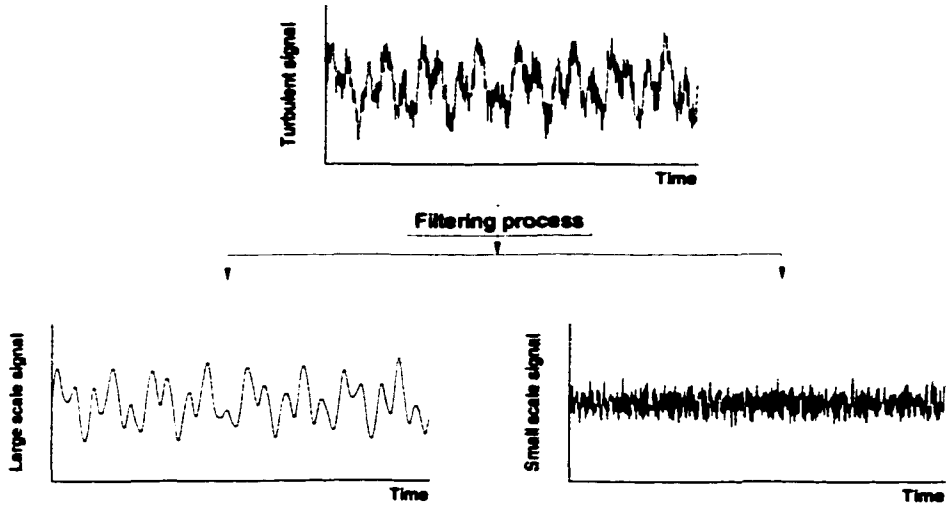

Figure 1.4: Turbulent signal subjected to filtering processes

for most of the transport of mass, momentum and energy. The structure of large eddies is strongly dependent on the geometry and nature of the flows. On the other hand, the small eddies carry a small portion of the total turbulent kinetic energy and are much more universal and nearly isotropic. This leads to the concept of large eddy simulation. Since the small eddies have less impact on the flow, they are less important and it should be possible to represent their effect by simple subgrid scale models, while the large eddies are simulated directly.

The separation of large and small eddies is done by filtering. As mentioned earlier in Figure 1.2, at high Reynolds number, the turbulent energy spectrum contains an inertial subrange, in which there is no turbulence production or viscous dissipation. The concept of filtering in LES is to separate both scales and make the cut-off lie in this subrange. This filtering process is illustrated in Figure 1.4.

LES has been used in various areas of turbulence such as three-dimensional tran-

sitional flow [41, 42], turbulent channel flow [43, 44, 45], and has been found to work well for turbulent free shear flow and homogeneous turbulent flows. Other numerical studies dealing with complex turbulent flows including separation, reattachment and recirculation have been performed in recent years, on the backward facing step flow [46, 47, 48, 49], the surface mounted cube flow [50, 51, 52], the surface square cylinder flow [53], and the circular cylinder flow [54]. In terms of industrial applications, LES is not mature enough, due to the lack of robustness of the subgrid scale models, high computational cost, the difficulty in implementing realistic boundary conditions and stable nondissipate numerical schemes. However, there has been an attempt to apply large eddy simulation to flows encountered in nuclear reactors [55].

Several problems need to be resolved before LES can be applied to engineering flows [56]. The treatment of wall boundary conditions, is a particularly difficult problem since resolution of the flow there almost negates the advantage of LES over DNS, while use of wall functions to circumvent this are known to be inadequate. The other problem is subgrid scale modelling. The potential inadequacies of subgrid scale models become more critical as the proportion of turbulent energy contained in the subgrid scale becomes more important [57]. To address this problem, the dynamic subgrid scale modelling approach was developed [58] and later modified by Lilly [59]. However, Speziale [60] argued recently that the dynamic subgrid scale model is not suitable for turbulent flows in complex geometries, due to the unreliability of the test filtering procedure required for dynamic models. He proposed a Reynolds stress based model for "Very Large Eddy Simulation" (VLES).

The mathematical formulations of LES and subgrid scale models used in the present research, are presented in the next chapter.

1.3.3 Reynolds-Averaged Navier-Stokes (RANS)

Due to the lack of maturity of LES and their prohibitive computational cost, engineering methods still rely on the numerical solution of the Reynolds-Averaged Navier-Stokes (RANS) equations in conjunction with turbulence models. In this approach, all equations of motion are averaged over time and coordinate in which the mean flow does not vary. The time averaged equations are obtained using the statistical approach, first suggested by Reynolds [61]. The averaging process gives rise to additional unknown terms (the averages of products of fluctuating velocities) usually referred to as "Reynolds or turbulent stresses". In order to have a "closed" set of equations, the Reynolds stresses have to be modelled by correlations, algebraic or differential equations, known as "turbulence models" [62].

These models vary in degree of complexity ranging from algebraic eddy viscosity models (EVM) to Reynolds stress models (RSM). EVM's provide adequate predictions of some features of complex flows, but require *ad-hoc* adjustment that restrict their reliability and generality [63]. The most widely used engineering models for computing turbulent flows have been the classical two-equation k - ϵ model and its variants. RSM's [64] are more complex and computationally intensive, but they provide a conceptually more correct representation of turbulence characteristics than EVMs. However, both EVM's and RSM's exhibit deficiencies in complex flows primarily due to the assumption that turbulent transport is based on a single characteristic length and time scale. Additionally, these models do not account for departures from equilibrium and the effects of streamline curvature.

A more satisfactory representation of turbulent transport and dynamics in this approach can be achieved via the Multiple Scale (MS) approach [65], which accounts

for non-equilibrium conditions and in which more than one characteristic length and time scales are used. Such models have been applied to several complex flows include the backward facing step [66] and prismatic obstacles [67].

1.4 Scope of the Dissertation

The main objectives of this research are: (i) to investigate the characteristics of the flow and convective heat transfer for a "prototype" separated flow (bluff rectangular plate) at high Reynolds number, where the flow is completely turbulent using the large eddy simulation (LES) technique, (ii) to gain further insight into the dynamics and structures of the flow, and (iii) to evaluate the performance of the subgrid scale models.

The investigation has been divided into two major parts, flow dynamics and convective heat transfer. The flow is investigated in two-dimensional and three-dimensional simulations covering all three ranges of Reynolds number. Direct numerical simulation is used to simulate the flows at low and moderate Reynolds number. The high Reynolds number case of 50,000, for which reliable mean flow, turbulence statistics and wall data is available, is seleted for comparison and assessment. Convective heat transfer simulations are performed in both two and three dimensions at low and moderate Reynolds number.

The outline of the dissertation is as follows. The mathematical description of large eddy simulation and the subgrid scale models are presented in Chapter 2. The wall treatment for the high Reynolds number flows is also reviewed. In Chapter 3, the computational procedures used in the CFD code are discussed. The two and

three-dimensional flow simulations presented and discussed in Chapters 4 and 5 respectively. Chapter 6 presents the results and the discussions of the convective heat transfer calculations. Finally, in Chapter 7, the conclusions of this investigation are summarized and recommendations for further work are proposed.

Chapter 2

LARGE EDDY SIMULATION

2.1 Introduction

In this chapter, the large eddy simulation methodology is described and the governing equations are presented. These include the filtered flow field equations, the three subgrid scale models used in this study: Smagorinsky (SM), structure function (SFM) and selective structure function (SSFM) models, and the details of the near-wall treatment.

2.2 Governing Equations

Fluid motion is governed by three basic conservations laws: conservation of mass, conservation of momentum and conservation of energy. In this research, the fluid is taken as an incompressible Newtonian fluid with constant fluid properties (ρ and μ). In flows accompanied by heat transfer, the fluid properties are normally functions

of temperature. With the assumption of small temperature variation in the forced convection regime, one can also treat these properties as constant. This allows the decoupling of the hydrodynamic equations from the energy equation.

With these assumptions, the three conservation relations are expressed as [68],

Continuity equations:

$$\frac{\partial U_i}{\partial x_i} = 0 \tag{2.1}$$

Momentum equations:

$$\frac{\partial U_i}{\partial t} + \frac{\partial (U_j U_i)}{\partial x_j} = -\frac{1}{\rho}\frac{\partial p}{\partial x_i} + \frac{\partial}{\partial x_j}\left(\nu \frac{\partial U_i}{\partial x_j}\right) \tag{2.2}$$

Energy equations:

$$\frac{\partial T}{\partial t} + \frac{\partial (U_j T)}{\partial x_j} = \frac{\partial}{\partial x_j}\left(\alpha \frac{\partial T}{\partial x_j}\right) \tag{2.3}$$

where U_i is the instantaneous velocity in the x_i direction (i and j = 1, 2, 3), p is the static pressure and T is the temperature of the fluid.

In large eddy simulation, a filter operation is used to decompose each field of the general variable Φ (where $\Phi = U, V, W, p$ and T) into a large scale (resolved or filtered) component denoted by a bar, $\overline{\Phi}$, and a small scale (subgrid) component denoted by ϕ,

$$\Phi = \overline{\Phi} + \phi \tag{2.4}$$

This decomposition follows an approach similar to the Reynolds-decomposition of a generic field into an average and a fluctuating component, which is the basis for all RANS approaches. In LES, however the large scale component ($\overline{\Phi}$) is time-dependent and is completely resolved on the computational grid, while the small scale component

(ϕ) is unresolved and must be modeled.

Following the general approach described by Leonard [69], the large scale component is the result of applying a filter to the instantaneous variables,

$$\overline{\Phi}(x_i,t) = \int_v G(x_i - x'_i)\Phi(x'_i,t)\, dv'_i \tag{2.5}$$

where G is a filter function with a characteristic length of Δ and x'_i is a dummy variable representing x_i. Several filter functions have been used in LES, including Gaussian, box (top hat) and cut-off filters. For finite difference and finite volume methods, a simple box filter has been commonly used [43]. This box filter function is expressed as,

$$G(x_i - x'_i) = \begin{cases} 1/\Delta & \text{for } |x_i - x'_i| \leq \Delta/2 \\ 0 & \text{elsewhere} \end{cases} \tag{2.6}$$

Applying the filter operation to equations (2.1), (2.2) and (2.3), yields the filtered (large scale) governing equations.

$$\frac{\partial \overline{U}_i}{\partial x_i} = 0 \tag{2.7}$$

$$\frac{\partial \overline{U}_i}{\partial t} + \frac{\partial(\overline{U_j}\overline{U}_i)}{\partial x_j} = -\frac{1}{\rho}\frac{\partial \overline{p}}{\partial x_i} + \frac{\partial}{\partial x_j}\left(\nu \frac{\partial \overline{U}_i}{\partial x_j}\right) \tag{2.8}$$

$$\frac{\partial \overline{T}}{\partial t} + \frac{\partial(\overline{U_j T})}{\partial x_j} = \frac{\partial}{\partial x_j}\left(\alpha \frac{\partial \overline{T}}{\partial x_j}\right) \tag{2.9}$$

These equations include additional subgrid terms which quantify the interaction between the grid (resolved) scales and subgrid (unresolved) scales. These subgrid terms arise due to the non-linearity of the filtering operation applied to $\overline{U_j U}_i$ in (2.8).

Using (2.4), the product of $\overline{U_j U_i}$ expands to,

$$\overline{U_j U_i} = \overline{(\overline{U}_j + u_j)(\overline{U}_i + u_i)} = \overline{\overline{U}_j \overline{U}_i} + \overline{u_j \overline{U}_i} + \overline{\overline{U}_j u_i} + \overline{u_j u_i} \tag{2.10}$$

An important difference for the kind of filtering defined by (2.5) compared to Reynolds averaging is that a second filtering does not reproduce the result of the first filtering, i.e. $\overline{\Phi} \neq \overline{\overline{\Phi}}$. Consequently, $\overline{\overline{U}_j \overline{U}_i} \neq \overline{U}_j \overline{U}_i$. Equation 2.10 can be rearranged as,

$$\overline{U_j U_i} - \overline{U}_j \overline{U}_i = \left(\overline{\overline{U}_j \overline{U}_i} - \overline{U}_j \overline{U}_i \right) + \left(\overline{u_j \overline{U}_i} + \overline{\overline{U}_j u_i} \right) + \overline{u_j u_i} \tag{2.11}$$

The first term on the RHS, usually called the "Leonard stress term" after Leonard [69], represents interactions between eddies within the resolved part of the turbulence spectrum. The second term is a "cross stress term" which quantifies the interaction between the resolved scales and the subgrid scales. The last term is the "true subgrid scale stress term" and represents the interaction among the subgrid scales.

The Leonard stress term is dependent on the large scale component and can be computed in terms of the filtered field. The small scale component of the velocity field is unknown and needs to be modeled in terms of resolved quantities. Several approaches [44, 70, 71] has been made to model each RHS term of (2.11) separately, since they represent different physical phenomena. In recent years, one argues that since SGS modelling is far from exact [39], it seems preferable to model (2.11) as a whole, without splitting it into parts [39, 40]. This approach is to combine all such terms and model them as a single *subgrid scale stress tensor* , τ_{ij}. The models used to approximate this subgrid scale stress tensor are called "subgrid scale" (SGS) models.

$$\tau_{ij} = -(L_{ij} + C_{ij} + R_{ij}) \tag{2.12}$$

where $\tau_{ij} = \overline{U_j}\overline{U_i} - \overline{U_j U_i}$. L_{ij}, C_{ij} *and* R_{ij} represent the Leonard stresses, cross stresses and true subgrid scale Reynolds stresses, respectively.

Substituting the subgrid scale stress tensor, τ_{ij} into (2.8), yields the filtered Navier-Stokes equations.

$$\frac{\partial \overline{U}_i}{\partial t} + \frac{\partial(\overline{U}_j \overline{U}_i)}{\partial x_j} = -\frac{1}{\rho}\frac{\partial \overline{p}}{\partial x_i} + \frac{\partial}{\partial x_j}\left(\nu \frac{\partial \overline{U}_i}{\partial x_j} + \tau_{ij}\right) \tag{2.13}$$

Similarly, the filtered energy equation takes the form,

$$\frac{\partial \overline{T}}{\partial t} + \frac{\partial \overline{U}_j \overline{T}}{\partial x_j} = \frac{\partial}{\partial x_j}\left(\alpha \frac{\partial \overline{T}}{\partial x_j} + \overline{T}\ \overline{U}_j - \overline{T U_j}\right) \tag{2.14}$$

2.3 Subgrid Scale Models

The subgrid scale model is based on a gradient-diffusion hypothesis, similar to the Boussinesq hypothesis of conventional turbulence models. It consists of assuming the deviatoric part of the stress tensor, τ_{ij}, to be proportional to the resolved strain rate tensor, $\overline{S}_{ij}$.

$$\tau_{ij} - \frac{1}{3}\tau_{kk}\delta_{ij} = 2\nu_t \overline{S}_{ij} \tag{2.15}$$

in which,

$$\overline{S}_{ij} = \frac{1}{2}\left(\frac{\partial \overline{U}_i}{\partial x_j} + \frac{\partial \overline{U}_j}{\partial x_i}\right) \tag{2.16}$$

where ν_t is the eddy viscosity, which has to be expressed by the appropriate model, and δ_{ij} is the Kronecker delta. For simplicity the trace $\frac{1}{3}\tau_{kk}$ is lumped with the pressure to form a "modified pressure", $\overline{P} = \overline{p} - \frac{1}{3}\rho\tau_{kk}$. The filtered Navier-Stokes equations become,

$$\frac{\partial \overline{U}_i}{\partial t} + \frac{\partial(\overline{U}_j\overline{U}_i)}{\partial x_j} = -\frac{1}{\rho}\frac{\partial \overline{P}}{\partial x_i} + \frac{\partial}{\partial x_j}\left\{\nu\frac{\partial \overline{U}_i}{\partial x_j} + \nu_t\left(\frac{\partial \overline{U}_i}{\partial x_j} + \frac{\partial \overline{U}_j}{\partial x_i}\right)\right\} \tag{2.17}$$

The same approach can be applied to the filtered energy equation. The last two terms of (2.14) are modeled with an eddy diffusivity (α_t) to yield,

$$\frac{\partial \overline{T}}{\partial t} + \overline{U}_j\frac{\partial \overline{T}}{\partial x_j} = \frac{\partial}{\partial x_j}\left\{(\alpha + \alpha_t)\frac{\partial \overline{T}}{\partial x_j}\right\} \tag{2.18}$$

Equations (2.7), (2.17) and (2.18) are formally identical to the time-dependent version of the governing equations for turbulent flow based on conventional eddy viscosity models such as the $k-\epsilon$ model. In order to solve this set of equations, both ν_t and α_t need to be computed as functions of resolved quantities.

2.3.1 Smagorinsky Model

The first and most widely used subgrid scale model was proposed by Smagorinsky [72]. In this model, a mixing-length type of assumption is made, whereby the eddy viscosity is assumed to be proportional to the characteristic length scale associated with the filter width (Δ) and to the characteristic turbulent velocity based on the second invariant of the resolved strain rate tensor, i.e.

$$\nu_t = (C_s\Delta)^2|\overline{S}| \tag{2.19}$$

where,

$$|\overline{S}| = \sqrt{2\overline{S}_{ij}\overline{S}_{ij}} \tag{2.20}$$

The model parameter (C_s), sometimes called the "Smagorinsky constant", ranges from 0.065 to 0.23 depending on the flow conditions, the grid sizes and the numerical methods used. For homogeneous isotropic turbulence where the filter cutoff is in the inertial subrange, the optimal value is found to be around 0.23 [73]. However, in applications where the mean shear is dominant such as free shear flow and channel flow [44], a smaller value of C_s is necessary to avoid excessive dissipation [40] and value of C_s on the order of 0.1.

The parameter Δ is a length scale and it is generally related to the width of the filter used. In finite difference and finite volume simulations, the common choice of Δ is the average local cell size [43].

$$\Delta = (\Delta_x \Delta_y \Delta_z)^{1/3} \tag{2.21}$$

where Δ_x, Δ_y and Δ_z are the mesh sizes along the three directions.

In the vicinity of solid boundaries (walls), the subgrid scale eddy viscosity should become vanishingly small. One of the approaches used to ensure the correct asymptotic behaviour near walls is to introduce a Van Driest type damping function [74] similar to the approach used in conventional low Reynolds number turbulence modeling. The damping function is given by,

$$D = 1 - e^{-(y^+/A^+)} \tag{2.22}$$

where y^+ is the distance from the wall in "wall units", $y^+ = yu_\tau/\nu$, and A^+ is a

constant usually taken to be approximately 25. The Smagorinsky subgrid scale eddy viscosity becomes:

$$\nu_t = (C_s D\Delta)^2 (2\overline{S}_{ij}\overline{S}_{ij})^{1/2} \tag{2.23}$$

Despite its simplicity, there are many difficulties with Smagorinsky model such as its performance in near-wall regions and transitional flow. Previous LES showed that the Smagorinsky model is too dissipative and does not allow the transition from laminar to turbulent to proceed [75]. In addition, the Smagorinsky model does not account for the energy flow from small scales to large scales which can be significant [41]. Further development has been proposed to overcome these difficulties by locally calculating the eddy viscosity coefficient. This model is known as the dynamic subgrid scale model [58]. Due to the complexity and stability of the model, the present work will focus solely on the Smagorinsky model.

2.3.2 Structure Function Model

In this model, the eddy viscosity is evaluated with the aid of a local kinetic energy spectrum which can be calculated in terms of the local second order velocity structure function, $\overline{F}_2(x_i, \Delta, t)$ [40].

$$\overline{F}_2(x_i, \Delta, t) = \left\langle \| \overline{U}(x_i + r, t) - \overline{U}(x_i, t) \|^2 \right\rangle_{\|r\|=\Delta} \tag{2.24}$$

and

$$\nu_t = 0.105\, C_k^{-3/2} \Delta [\overline{F}_2(x_i, \Delta, t)]^{1/2} \tag{2.25}$$

where Δ is the average cell size, as in equation (2.21), and C_k is typically taken to be approximately 1.4 [40]. From (2.24), $\overline{F}_2$ is calculated from a local statistical average

of the square velocity differences between x_i and the six closest points surrounding x_i on the computational grid. In order to minimize the sensitivity of the model to the mean flow gradients and to avoid difficulties with large grid aspect ratios, $\overline{F}_2$ is evaluated using only four neighbouring points in the given plane following [40]. For an $x-z$ plane, the equivalent average cell size is then defined as $\Delta = (\Delta_x \Delta_z)^{1/2}$.

Similar to Smagorinsky model, the structure function model is still too dissipative, especially for transition in a boundary layer and channel flow [40]. To overcome this difficulty, an improved version of the structure function is developed, and presented in the next section.

2.3.3 Selective Structure Function Model

The selective structure function model refers to the localization of the subgrid scale dissipation to the small scale turbulence only. The idea is to switch off the eddy viscosity when the flow is not sufficiently three-dimensional. The three-dimensionality criterion is based on the angle, β, between the local vorticity and the average vorticity at the six closest neighbouring points (or optionally the four neighbouring points). The eddy viscosity is set to zero when this angle is less than 20° [40].

$$\nu_t = 0.1638\, C_k^{-3/2} \zeta \Delta [\overline{F}_2(x_i, \Delta, t)]^{1/2} \tag{2.26}$$

where ζ is the selectivity option. In the present study rather than using an abrupt cut-off, ζ is evaluated using a smooth function defined as,

$$\zeta = \begin{cases} 0 & \text{for } \beta < 10^\circ \\ e^{-(d\beta/3)^2} & \text{for } 20^\circ \geq \beta \geq 10^\circ \text{ and } d\beta = |\beta - 20| \\ 1 & \text{for } \beta > 20^\circ \end{cases} \tag{2.27}$$

2.4 Wall Treatment

One of the most difficult problems in LES is the correct formulation of boundary conditions for the resolved fields at a solid surface. Near the solid surface, the turbulent structures are small compared to the overall flow dimensions and yet they play an important role in the dynamics of turbulent boundary layers. In order to compute the velocity gradients and to compute the wall shear stress, the grid distribution in the direction normal to the surface needs to be sufficiently small as to extend into the viscous sublayer ($y^+ < 5$) [44]. This dramatically increases the cost of large eddy simulation, and in effect entails a direct numerical simulation of the near-wall region.

In order to avoid large computational efforts for resolving the wall layer directly, several approximate wall boundary conditions have been developed. Further reviews can be found in [76]. One way to overcome this problem is to use approximate wall boundary conditions [77] in which the wall shear stress (τ_w) and the velocity gradient ($\frac{\partial \overline{U}}{\partial x_j}$) are not computed directly, but rather are specified in terms of the resolved velocity in the core of the flow. This approach allows the first grid point to be placed in the logarithmic region and saves simulating the wall layer entirely. Nevertheless, the approximate wall boundary conditions have been only applied to the flat wall with mild pressure gradient and they are not adequate for the flows which include complex separated and reattaching flows [39]. Recently, a two-layer approximate boundary condition has been proposed [76] in which the outer layer is solved with LES and the

inner layer is solved with a simple set of boundary layer equations.

Most near-wall calculations are formulated in terms of a universal velocity profile described with non-dimensional "wall units", $y^+ = yu_\tau/\nu$ and $u^+ = \overline{U}/u_\tau$. The wall shear stress is defined as,

$$\tau_w = \rho u_\tau^2 \tag{2.28}$$

In the present research, the instantaneous velocity profiles near the wall are assumed to follow a classical three layer distributions including inner layer, buffer and logarithmic layer and outer layer [68]. These layers are summarized below and their profiles are represented in Figure 2.1.

Inner layer law: $y^+ < 5$

$$y^+ = u^+ \tag{2.29}$$

Buffer/Log layer law: $5 \leq y^+ \leq 200$

$$y^+ = u^+ + e^{-KB}\left[e^{Ku^+} - 1 - Ku^+ - \frac{(Ku^+)^2}{2} - \frac{(Ku^+)^3}{6}\right] \tag{2.30}$$

Outer layer law: $y^+ > 200$

$$u^+ = \frac{1}{K} ln(y^+) + B \tag{2.31}$$

where K is the von Karman constant ($K \approx 0.41$) and B is an empirical constant related to the thickness of the viscous sublayer ($B \approx 5.0$).

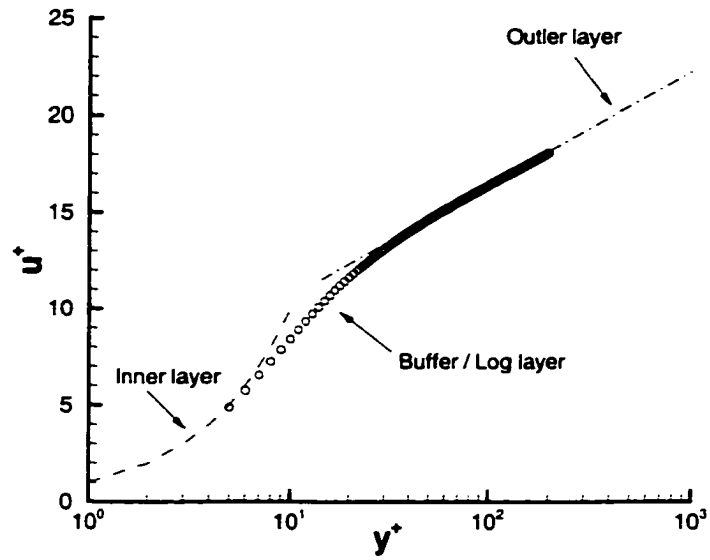

Figure 2.1: Velocity profile over three layers of the near-wall region

2.5 Summary of Governing Equations

To summarize, the three fundamental governing equations expressing mass, momentum and energy conservation and the various subgrid scale models are presented. These equations will be discretized in the next chapter.

2.5.1 Filtered (Large Scale) Governing Equations

Continuity equations:

$$\frac{\partial \overline{U}_i}{\partial x_i} = 0 \tag{2.32}$$

Momentum equations:

$$\frac{\partial \overline{U}_i}{\partial t} + \frac{\partial (\overline{U}_j \overline{U}_i)}{\partial x_j} = -\frac{1}{\rho}\frac{\partial \overline{P}}{\partial x_i} + \frac{\partial}{\partial x_j}\left\{\nu \frac{\partial \overline{U}_i}{\partial x_j} + \nu_t \left(\frac{\partial \overline{U}_i}{\partial x_j} + \frac{\partial \overline{U}_j}{\partial x_i}\right)\right\} \tag{2.33}$$

Energy equations:

$$\frac{\partial \overline{T}}{\partial t} + \overline{U}_j \frac{\partial \overline{T}}{\partial x_j} = \frac{\partial}{\partial x_j}\left\{(\alpha + \alpha_t)\frac{\partial \overline{T}}{\partial x_j}\right\} \tag{2.34}$$

$$\alpha_t = \frac{\nu_t}{Pr_t} \tag{2.35}$$

2.5.2 Subgrid Scale Models

Smagorinsky Model (SM):

$$\nu_t = (C_s D\Delta)^2 (2\overline{S}_{ij}\overline{S}_{ij})^{1/2} \tag{2.36}$$

Structure Function Model (SFM):

$$\nu_t = 0.105\, C_k^{-3/2} \Delta [\overline{F}_2(x_i, \Delta, t)]^{1/2} \tag{2.37}$$

$$\overline{F}_2(x_i, \Delta, t) = \left\langle \| \overline{U}(x_i + r, t) - \overline{U}(x_i, t) \|^2 \right\rangle_{\|r\|=\Delta} \tag{2.38}$$

Selective Structure Function Model (SSFM):

$$\nu_t = 0.1638\, C_k^{-3/2} \zeta \Delta [\bar{F}_2(x_i, \Delta, t)]^{1/2} \tag{2.39}$$

Chapter 3

COMPUTATIONAL PROCEDURE

3.1 Introduction

The governing equations presented in the previous chapter are discretized using a finite volume method and the resulting set of algebraic equations are solved using a modified version of the Unsteady Turbulent Flow (UTF) code [78]. The code was originally developed for multi-dimensional turbulent flows in complex geometries using RANS and LES and incorporated the structure function (SFM) and selective structure function (SSFM) subgrid scale models. Modifications included the addition of the Smagorinsky (SM) model and the energy equation for modeling convective heat transfer.

In this chapter, an overview of the computational procedure is presented. First, the finite volume discretization of all governing equations is discussed. This is fol-

Equations	Φ	Γ_Φ	S_Φ
Continuity	1	0	0
Momentum	U_i	$\nu + \nu_t$	$-\frac{1}{\rho}\frac{\partial P}{\partial x_i} + \frac{\partial}{\partial x_j}\left(\nu_t \frac{\partial U_j}{\partial x_i}\right)$
Energy	T	$\alpha + \alpha_t$	0

Table 3.1: Summary of the diffusion coefficients and the source terms for the governing equations

lowed by the spatial discretization for the convective and the diffusive term, and the temporal discretization for the unsteady term. Finally, the fractional step method for the solution of the Navier-Stokes equation and the direct and conjugate gradient method used for solving the linear system arising from the discretization of pressure (Poisson) equation are discussed.

3.2 Finite Volume Discretization

The governing equations for momentum and energy transport were summarized in section 2.5.1 and can be represented by a general transport equation,

$$\frac{\partial \Phi}{\partial t} + \frac{\partial (\Phi U_j)}{\partial x_j} = \frac{\partial}{\partial x_j}\left(\Gamma_\Phi \frac{\partial \Phi}{\partial x_j}\right) + S_\Phi \tag{3.1}$$

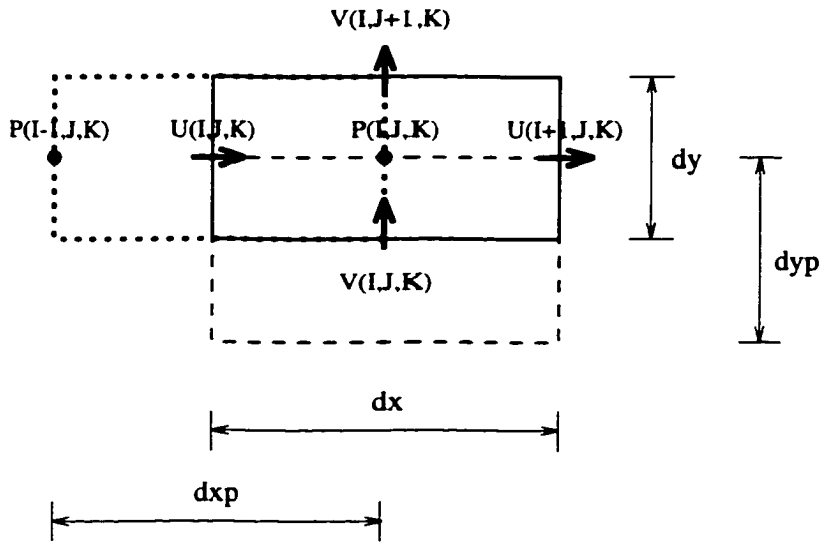

Figure 3.1: Finite volumes on a staggered grid arrangement for a Cartesian two-dimensional grid: solid line for P control volume; dotted line for U control volume; and dashed line for V control volume

where $\Phi = (U, V, W \text{ and } T)$, Γ_Φ is a diffusion coefficient and S_Φ is a general source term. The diffusion coefficient and source term, corresponding to each equation are given in Table 3.1. For simplicity, the bar ($\overline{\Phi}$) denoting the filtered component in Section 2.5.1 is dropped hereafter.

These equations are discretized using a finite volume formulation in which the computational domain is divided into a number of overlapping control volumes. The input grid defines the control volumes for scalar fields (pressure, temperature, etc.). The velocities' control volumes are offset such that their centers are located at the face of the scalar control volumes. This staggered grid/volume arrangement is employed in order to avoid the decoupling of velocity and pressure fields or "checkerboard problem" [79].

A typical arrangement of a staggered grid is illustrated in Figure 3.1 for a two-

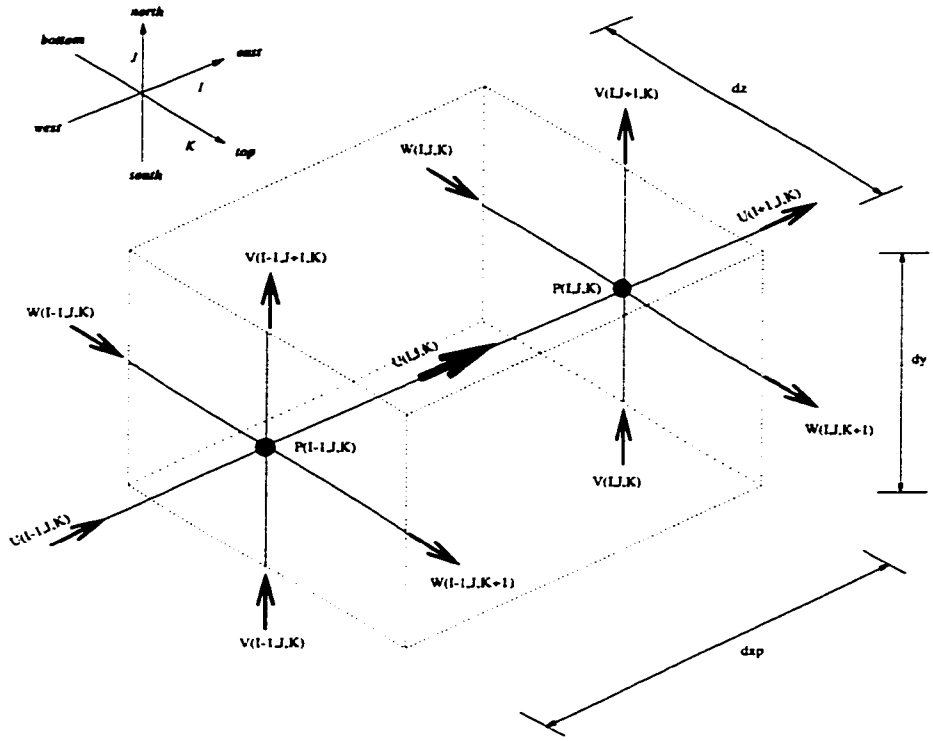

Figure 3.2: Three-dimensional control volume for $U(I, J, K)$

dimensional case. In this arrangement, the node for $P(I, J, K)$ is midway between the nodes for $U(I, J, K)$, and $U(I+1, J, K)$, and $V(I, J, K)$, and $V(I, J+1, K)$. Figure 3.2 illustrates a three-dimensional U velocity control volume centered at location (I, J, K), (indicated by a bold $\rightarrow$). The faces of a control volume are identified by the terms **west, east, south, north, bottom** and **top**, as indicated in the figure.

The discretized equations are derived by integrating the appropriate transport equation (3.1) over each control volume.

$$\int\int\int \left[\frac{\partial \Phi}{\partial t} + \underbrace{\frac{\partial (\Phi U_j)}{\partial x_j} - \frac{\partial}{\partial x_j}\left(\Gamma_\Phi \frac{\partial \Phi}{\partial x_j}\right)}_{\mathbf{F}} - S_\Phi \right] dv = 0 \qquad (3.2)$$

Using Gauss's divergence theorem,

$$\int\int\int \frac{\partial a_i}{\partial x_i}\, dv = \int\int a_i n_i\, ds \tag{3.3}$$

the volume integral of term **F** in equation (3.2) is transformed into a surface integral,

$$\begin{aligned}
\frac{\partial}{\partial t}\int\int\int \Phi\, dv - \int\int\int S_\Phi\, dv = \\
+\int\int_{east}\left(\Gamma_\Phi\frac{\partial\Phi}{\partial x_j} - \Phi U_j\right) ds_x - \int\int_{west}\left(\Gamma_\Phi\frac{\partial\Phi}{\partial x_j} - \Phi U_j\right) ds_x \\
+\int\int_{north}\left(\Gamma_\Phi\frac{\partial\Phi}{\partial x_j} - \Phi U_j\right) ds_y - \int\int_{south}\left(\Gamma_\Phi\frac{\partial\Phi}{\partial x_j} - \Phi U_j\right) ds_y \\
+\int\int_{top}\left(\Gamma_\Phi\frac{\partial\Phi}{\partial x_j} - \Phi U_j\right) ds_z - \int\int_{bottom}\left(\Gamma_\Phi\frac{\partial\Phi}{\partial x_j} - \Phi U_j\right) ds_z
\end{aligned} \tag{3.4}$$

The integral equation (3.4) is exact, however some approximation (discretization) must be used to reduce the equation to algrebraic form. The simplest second order accurate approximation is to represent the volume integral by the product of the volume-averaged ($\hat{\Phi}$) and its volume (Δv) [80],

$$\int\int\int \Phi\, dv = \hat{\Phi}\Delta v \approx \Phi\Delta v \tag{3.5}$$

The volume-averaged ($\hat{\Phi}$) value needs to be determined in order to represent the volume integral in (3.5). This is done by introducing an approximation for $\hat{\Phi}$. Several approximations can be obtained by interpolating nodal values or by using shape functions; for example, a forth order approximation can be obtained by using the bi-quadratic shape function [80]. Higher order approximations of the volume-averaged value are very complex. For simplicity, the present work approximates the volume-

average with the value at the center of the control volume, $\hat{\Phi} \approx \Phi$, since all variables are available at the nodal value and interpolation is unnecessary. This approximation becomes exact when Φ is constant or Φ varies linearly within the control volume.

The right hand side terms in (3.4) represent the diffusive and the convective fluxes. The approximation of these fluxes through a given face of the control volume is represented by,

$$\int\int (Flux)_i \, ds_i = [Flux]_i \, \Delta s_i \approx Flux|_i \, \Delta s_i \tag{3.6}$$

To compute the surface-averaged flux in (3.6), $[Flux]$ term, the averaged value of Φ, U_j and $\frac{\partial \Phi}{\partial x_j}$ on the surface Δs_i need to be determined. Again, some approximations must be introduced in order to obtain the averaged value. The simplest approximation is to approximate at the cell face center which is equivalent to the mean value over the surface. Further details will be discussed in the next section.

To complete the discretization procedure, the source term S_Φ needs to be approximated. From Table 3.1, a non-zero source term appears only in the momentum equations and contains a pressure gradient $(\frac{1}{\rho}\frac{\partial P}{\partial x_i})$ and an additional diffusion $\left(\frac{\partial}{\partial x_j}(\nu_t \frac{\partial U_j}{\partial x_i})\right)$ term. Using the procedure outlined above, these two terms are discretized and summarized in Table 3.2.

3.3 Spatial Discretization Scheme

The determination of the surface-averaged fluxes in (3.6) involves the product of several variables and their gradients at those locations: ΦU_i for the convective flux

Equations	Φ	$\int\int\int S_\Phi dv$
x-momentum	U	$\int\int_{east}(\frac{1}{\rho}P - \nu_t\frac{\partial U}{\partial x})ds_x - \int\int_{west}(\frac{1}{\rho}P - \nu_t\frac{\partial U}{\partial x})ds_x$ $+\int\int_{north}(-\nu_t\frac{\partial V}{\partial x})ds_y - \int\int_{south}(-\nu_t\frac{\partial V}{\partial x})ds_y$ $+\int\int_{top}(-\nu_t\frac{\partial W}{\partial x})ds_z - \int\int_{bottom}(-\nu_t\frac{\partial W}{\partial x})ds_z$
y-momentum	V	$\int\int_{east}(-\nu_t\frac{\partial U}{\partial y})ds_x - \int\int_{west}(-\nu_t\frac{\partial U}{\partial y})ds_x$ $+\int\int_{north}(\frac{1}{\rho}P - \nu_t\frac{\partial V}{\partial y})ds_y - \int\int_{south}(\frac{1}{\rho}P - \nu_t\frac{\partial V}{\partial y})ds_y$ $+\int\int_{top}(-\nu_t\frac{\partial W}{\partial y})ds_z - \int\int_{bottom}(-\nu_t\frac{\partial W}{\partial y})ds_z$
z-momentum	W	$\int\int_{east}(-\nu_t\frac{\partial U}{\partial z})ds_x - \int\int_{west}(-\nu_t\frac{\partial U}{\partial z})ds_x$ $+\int\int_{north}(-\nu_t\frac{\partial V}{\partial z})ds_y - \int\int_{south}(-\nu_t\frac{\partial V}{\partial z})ds_y$ $+\int\int_{east}(\frac{1}{\rho}P - \nu_t\frac{\partial W}{\partial z})ds_z - \int\int_{west}(\frac{1}{\rho}P - \nu_t\frac{\partial W}{\partial z})ds_z$

Table 3.2: Summary of the source terms for the momentum equations

and $\Gamma(\frac{\partial U_i}{x_j})$ or $\Gamma(\frac{\partial T}{x_i})$ for the diffusive flux, as shown in (A.1)-(A.4). These terms are computed by interpolating from the available nodal values of velocity, temperature etc.

3.3.1 Evaluation of the Convective Flux

The discretization scheme for the convective fluxes is critical to both accuracy and numerical stability. The values of both Φ and U_i at each face, are estimated by interpolating one or more of the neighboring nodal values. The convective flux through the face is then approximated using these interpolated values. A conventional way of dealing with the convective flux is to separate it into the product of a convected value (Φ) and the transport velocity(U_i). For example, the flux through the **east** face of Φ_P's control volume in Figure 3.3 is approximated as,

$$[\Phi U_i] \approx [\Phi]_{conv}\,[U_i]_{tran} \quad i.e. \quad [\Phi U]^{east} \approx [\Phi]^{east}_{conv}\,[U]^{east}_{tran} \tag{3.7}$$

where the superscript *east* refers to the interpolated value on the **east** face. The transport velocity, $[U]^{east}_{tran}$, is evaluated using a second order linear interpolation, which accounts for grid non-uniformity. The determination of the convected value, $[\Phi]^{east}_{conv}$ or Φ_e, depends on the discretization scheme.

Upwind Discretization Scheme (UDS)

This scheme approximates the value of Φ_e by its value at the node upstream or downstream of the control volume face, depending on the flow direction. This method is equivalent to the forward or backward difference approximation for the first derivative.

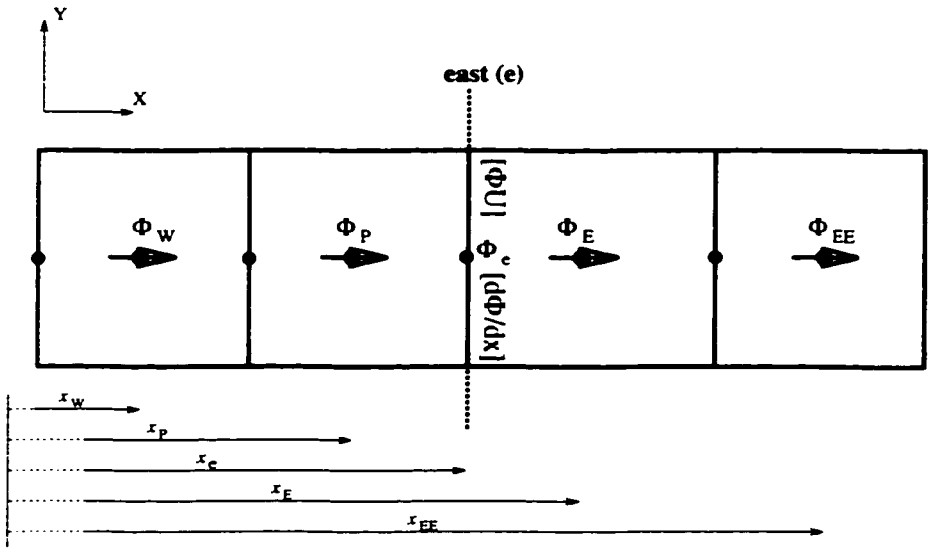

Figure 3.3: Convective and diffusive fluxes on the **east** face of control volume **P** in two-dimensional configuration

Using a Taylor series expansion between Φ_e and Φ_E, and Φ_e and Φ_P, we obtains,

$$\Phi_e = \Phi_P + \underbrace{(x_e - x_P)(\frac{\partial \Phi_P}{\partial x})}_{T.E.} + h.o.t. \tag{3.8}$$

and

$$\Phi_e = \Phi_E + \underbrace{(x_E - x_e)(\frac{\partial \Phi_E}{\partial x})}_{T.E.} + h.o.t. \tag{3.9}$$

where $h.o.t.$ is the higher order trunscation term. UDS is a first order accurate since the leading truncation error term ($T.E.$) is proportional to the grid spacing. In UDS, Φ_e is approximated as,

$$[\Phi]^{east}_{conv} = \Phi_e = \begin{cases} \Phi_E & \text{if } [U]^{east}_{tran} > 0 \\ \Phi_P & \text{if } [U]^{east}_{tran} < 0 \end{cases} \tag{3.10}$$

The UDS approximation is unconditionally stable. However, since the leading truncation error term is large, the approximation can be highly diffusive. This is sometimes known as false diffusion [79, 80].

Linear Interpolation

This approximation is equivalent to the central difference scheme (CDS) used in the finite difference method. It involves a linear interpolation between the two nearest nodes. At the **east** face , we have,

$$[\Phi]_{conv}^{east} = \Phi_e \cong \lambda_{e,P}\Phi_E + (1 - \lambda_{e,P})\Phi_P \tag{3.11}$$

where the interpolation factor $\lambda_{e,P}$ which accounts for non-uniform grids is defined as $\lambda_{e,P} = \frac{x_e - x_P}{x_E - x_P}$. This approximation is second order accurate with a leading truncation error of $T.E. = \frac{(x_e - x_P)(x_E - x_e)}{2}\left(\frac{\partial^2 \Phi_P}{\partial x^2}\right)$.

The CDS is dispersive, and may lead to numerical instability and oscillatory solutions if the grid spacing is not fine enough. Such oscillations may occur when the value of the local Peclet number, $Pe = U\Delta x/\nu$, exceeds 2 [79].

Quadratic Upwind Interpolation (QUICK)

QUICK (Quadratic Upwind Interpolation for Convective Kinematics) [81], approximates the value of a variable using a quadratic interpolation. It uses 3 nodal points, with 2 points upstream and 1 point downstream of the control volume face. A general

formulation for the QUICK scheme written for the east face is given by,

$$[\Phi]^{east}_{conv} = \Phi_e = \begin{cases} g_1\Phi_E - g_2\Phi_W + (1 - g_1 + g_2)\Phi_P & \text{if } [U]^{east}_{tran} > 0 \\ g_3\Phi_P - g_4\Phi_{EE} + (1 - g_3 + g_4)\Phi_E & \text{if } [U]^{east}_{tran} < 0 \end{cases} \tag{3.12}$$

where the coefficients g_i can be expressed in term of the interpolation factors defined earlier:

$$g_1 = \frac{(2 - \lambda_{e,W})\lambda^2_{e,P}}{1 + \lambda^2_{e,P} - \lambda_{e,W}} \qquad g_2 = \frac{(1 - \lambda_{e,P})(1 - \lambda_{e,W})^2}{1 + \lambda^2_{e,P} - \lambda_{e,W}}$$
$$g_3 = \frac{(1 + \lambda_{e,W})(1 - \lambda_{e,P})^2}{1 + \lambda^2_{e,E} - \lambda_{e,P}} \qquad g_4 = \frac{\lambda_{e,P}\lambda^2_{e,E}}{1 + \lambda^2_{e,E} - \lambda_{e,P}} \tag{3.13}$$

The expression above is valid on both uniform and non-uniform grids. A Taylor series expansion for Φ_e on a uniform grid with $[U]^{east}_{tran} > 0$ yields,

$$\Phi_e = \frac{\Phi_P + \Phi_E}{2} - \frac{1}{8}(\Phi_E - 2\Phi_P + \Phi_W) - \underbrace{\frac{3(\Delta x)^3}{48}\left(\frac{\partial^3\Phi}{\partial x^3}\right)_P}_{T.E.} + h.o.t. \tag{3.14}$$

which corresponds to (3.12) with $g_1 = 3/8$ and $g_2 = -1/8$ and shows that QUICK is a third order accurate. In practice QUICK is slightly more accurate than a linear interpolation, however both schemes converge asymptotically in a second order manner [80, 82]. The leading truncation error term ($T.E.$) is diffusive. It is therefore much more stable than the linear interpolation, but the numerical dissipation it introduces damps the smaller scales of motion in LES and DNS and removes substantial turbulent kinetic energy [83].

3.3.2 Evaluation of the Diffusive Flux

The discretization of the diffusive flux is based on the second order linear interpolation scheme. The approximation of the face averaged velocity or temperature gradients uses 2 points, with each point on either side of the interface. The approximation of the gradient is given by,

$$\left[\frac{\partial \Phi}{\partial x}\right]^{east} = \left(\frac{\partial \Phi}{\partial x}\right)_e = \frac{\Phi_E - \Phi_P}{x_E - x_P} + T.E. \tag{3.15}$$

The truncation error term (T.E.) for the above approximation is,

$$T.E. = \frac{(x_e - x_P)^2 - (x_E - x_e)^2}{2(x_E - x_P)} \left(\frac{\partial^2 \Phi}{\partial x^2}\right)_e + \frac{(x_e - x_P)^3 - (x_E - x_e)^3}{6(x_E - x_P)} \left(\frac{\partial^3 \Phi}{\partial x^3}\right)_e + h.o.t. \tag{3.16}$$

This approximation is truly second order on a uniform grid only; the leading truncation error term is proportional to the product of grid spacing and the grid expansion rate on non-uniform grids [80].

3.4 Temporal Discretization Scheme

The left hand side of the governing equations (A.1)-(A.4) contains the unsteady term ($\frac{\partial \Phi}{\partial t}$). The discretization of the temporal term is similar to the spatial discretization, except that a forward time stepping or "marching" procedure is used. This unsteady term is characterized by a "parabolic" behaviour, whereas the spatial terms exhibit an "elliptic" behaviour.

Two classes of methods, explicit and implicit, can be distinguished when the

unsteady term is discretized in conjunction with spatial fluxes. Explicit methods require nodal values at the previous (known) time step only and allow the direct calculation of each nodal value at the new time step. The implicit method requires values of surrounding nodes at the new time step and the solution requires an iterative method. For simplicity, the explicit method is used for calculating the velocity field at the new time step (further details will be given in the next section), since it requires less storage and generally less computational time. However, explicit methods impose constraints on the largest allowable time step in order to ensure stability. Several explicit schemes have been developed. In the present work, the Runge-Kutta method is used.

The Runge-Kutta scheme is a multi-point method. It uses points between t^n and t^{n+1} and is a self-starting scheme, since it does not require any data other than the initial condition. To define an $\mathbf{N}^{th}$ order Runge-Kutta scheme, we consider an equation of the form,

$$\frac{\partial \hat{\Phi}}{\partial t} = F(\hat{\Phi}) \tag{3.17}$$

Given the initial conditions $\hat{\Phi}^n$ and $F(\hat{\Phi}^n)$, the $\mathbf{N}^{th}$ order Runge-Kutta scheme with a step of Δt from $\hat{\Phi}^n$ is given by,

$$\begin{aligned} \hat{\Phi}^{n+1} &= \hat{\Phi}^n + \sum_{j=1}^{N} w_j k_j \\ k_j &= \Delta t \; F\left(\hat{\Phi}^n + \sum_{i=1}^{j-1} \beta_{ji} k_i\right) \end{aligned} \tag{3.18}$$

In order for the Runge-Kutta scheme to be accurate to the appropriate order, the

parameters w_j are constrained by,

$$\sum_{j=1}^{N} w_j = 1 \tag{3.19}$$

and a constraint parameter is defined by,

$$\sigma_j = \sum_{i=1}^{j-1} \beta_{ji} \tag{3.20}$$

with β_{ji} selected according to the order of the scheme.

3.4.1 First Order Runge-Kutta Scheme (RK1)

For $N = 1$, the Runge-Kutta scheme reduces to the explicit forward Euler scheme, which is first order accurate:

$$\hat{\Phi}^{n+1} - \hat{\Phi}^n = \Delta t \; F(\hat{\Phi}^n) \tag{3.21}$$

3.4.2 Second Order Runge-Kutta Scheme (RK2)

The second order scheme must satisfy the conditions $w_1 = 1 - 0.5\sigma_2^{-1}$ and $w_2 = 0.5\sigma_2^{-1}$. Since there are three unknowns and only two equations, there is more than one solution. For example,

Improved Euler method $\rightarrow w_1 = 1/2, w_2 = 1/2$ and $\sigma_2 = 1$

$$\hat{\Phi}^{n+1} - \hat{\Phi}^n = \frac{\Delta t}{2}\left(F(\hat{\Phi}^n) + F(\hat{\Phi}^n + \Delta t \; F(\hat{\Phi}^n)\right) \tag{3.22}$$

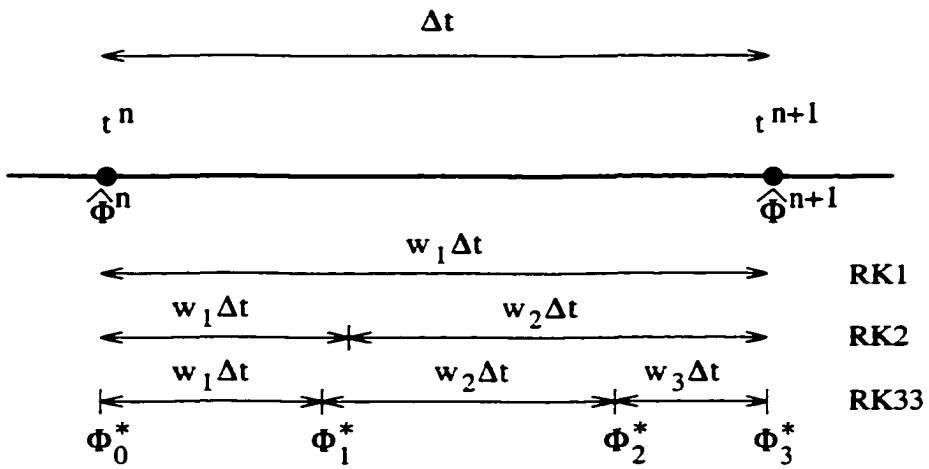

Figure 3.4: Location of the sub-step for the low-storage Runge-Kutta multi-order scheme

Modified Euler method $\rightarrow w_1 = 0, w_2 = 1$ and $\sigma_2 = 1/2$

$$\hat{\Phi}^{n+1} - \hat{\Phi}^n = \Delta t \left(F(\hat{\Phi}^n) + \frac{\Delta t}{2} F(\hat{\Phi}^n) \right) \tag{3.23}$$

3.4.3 Low-storage Third Order Runge-Kutta Scheme (RK33)

The Runge-Kutta method is considered to be more accurate and stable than other methods of the same order. The disadvantages of this scheme are that storage is required for each points between t_n and t_{n+1} (N times per one time step). A "low-storage" Runge-Kutta scheme [84], which requires the same storage as the first order Euler scheme and that can be applied to any order Runge-Kutta scheme (see Figure 3.4) is given as follows, with the appropriate choice of w_j, σ_j and β_{ji}:

$$q_j = a_j q_{j-1} + \Delta t \; F(\Phi^*_{j-1})$$

$$\Phi_j^* = \Phi_{j-1}^* + b_j q_j \tag{3.24}$$

where $j = 1$, N and $a_1 = 0$. For the case of RK33, $\Phi_0^* = \hat{\Phi}^n$ and $\Phi_3^* = \hat{\Phi}^{n+1}$ as shown in Figure 3.4 . Successive values of q_j and Φ_j^* overwrite the previous sub-step. So at any stage, only $2N$ storage locations of q and Φ^* are required. The parameters a_j and b_j can be determined by appropriately setting the coefficients w_j, σ_j and β_{ji}, as follows,

$$b_j = \beta_{j+1\ i} \qquad j \neq N$$

$$b_N = w_N$$

$$a_j = \frac{w_{j-1} - b_{j-1}}{w_j} \qquad (j \neq 1, w_j \neq 0)$$

$$a_j = \frac{\beta_{j+1\ j-1} - \sigma_j}{b_j} \qquad (j \neq 1, w_j = 0)$$

For a low-storage scheme, the necessary conditions for the third order Runge-Kutta are $w_1 = b_1 + a_2 b_2 + a_2 a_3 b_3$, $w_2 = b_2 + a_3 b_3$ and $w_3 = b_3$. One set of coefficients satisfying these conditions corresponds to [84]: $a_2 = 5/9$, $a_3 = -153/128$, $b_1 = 1/3$, $b_2 = 15/16$ and $b_3 = 8/15$. This low-storage scheme uses 10 less storage locations than the Leapfrog method and reduces the computational effort by a factor of 4 [84].

3.5 Solution Methods

A *semi-implicit fractional step* is used for solving the Navier-Stokes equations. The continuity equation and the pressure terms of the momentum equations are cast in implicit form (at new time t^{n+1}). Both convective and diffusive fluxes in the momentum and energy equations are treated explicitly.

3.5.1 Semi-Implicit Fractional Step Methods

The current method is modified from the original fractional step method of Kim and Moin [85]. These methods provide an approach that does not use pressure in the predictor step as in the pressure corrector methods (such as the well-known SIMPLE-family of algorithms). The pressure is treated explicitly in the first step of computing the velocity field. In the second step, the pressure is used to enforce the continuity equation. To demonstrate the method clearly, consider the simplest case of first order Euler time stepping of the Navier-Stokes equations written symbolically as:

$$\hat{u}_i^{n+1} = \hat{u}_i^n + (SU_i^n + P_i^{n+1})\Delta t \tag{3.25}$$

where $\hat{u}_i$ represents the velocity fields, SU_i represents the balance of convective and diffusive fluxes at every control volume face and P_i represents the pressure term, which is expressed implicitly.

Step 1: Calculate the *intermediate velocity field*, i.e. $\hat{u}_i^* = \hat{u}_i^n + SU_i^n \Delta t$, of (3.25). Where the first and second terms on RHS of (3.25) are explicit. The pressure term is negleted in this step.

Step 2: This step yields an appropriate pressure field implicitly using the continuity equation. The continuity equation is cast in implicit form and written as,

$$\frac{\partial \hat{u}_i^{n+1}}{\partial x_i} = 0 \tag{3.26}$$

Substituting $\hat{u}_i^{n+1}$ from (3.25) into the continuity equation results in a Poisson equation for pressure. The pressure field (P_i^{n+1}) is obtained by solving this Poisson equation using one of the methods described in the next section.

Step 3: Calculate the *divergence free velocity field*, i.e. $\hat{u}_i^{n+1}$ using equation (3.25) and the pressure obtained in step 2. Once the divergence free velocity field has been calculated, scalar fields (temperature etc.) can be computed as required.

3.5.2 Solution of Linear Equation System

The discretization of the pressure term in step 2, described above, leads to a very large system of linear equations (Poisson equation) having the general form,

$$Ax = b \tag{3.27}$$

The matrix A is a sparse matrix, containing 7 diagonal terms, or more if the periodicity condition is used. The structure of the matrix A is shown in Figure 3.5. If the boundary conditions are treated appropriately, then A is symmetric and positive definite. Two distinct methods, depending on the size of A have been used to solve (3.27).

Direct Method: LU Factorization

For relatively small size problems (usually two-dimensional simulations), storage is not a problem and a direct method is preferable. In the present calculation, LU factorization is used [86]. The sparse matrix A can be factored into the product of a lower triangular matrix L and upper triangular matrix U, i.e. $A = LU$. The solution to the original problem is then found by a two stage process;

First stage: $Ly = b$

Second stage: $Ux = y$

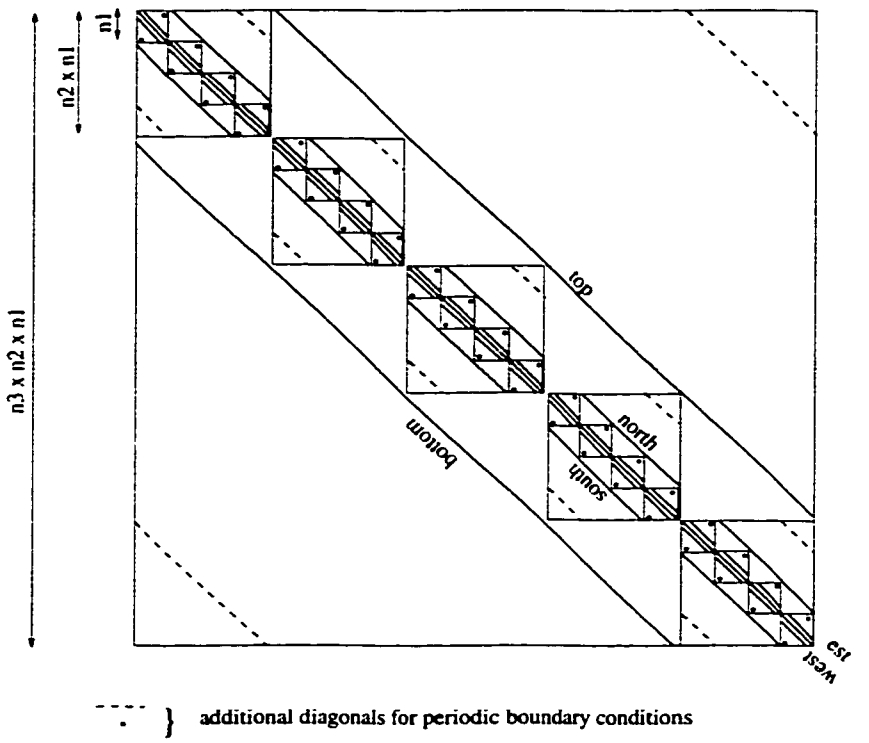

Figure 3.5: Structure of the matrix for natural ordering

LU factorization differs from Gaussian elimination since the factorization can be performed independently of b. The direct method, however, requires storage of all elements of the matrix. For computational problems with a large number of nodes, this method is prohibitive in term of memory, therefore iterative methods have to be considered.

Iterative Method: Conjugate Gradient Method

With the iterative approach, the original matrix A is decomposed into $A = M - N$. Equation (3.27) can be written as,

$$Mx = Nx + b \tag{3.28}$$

At iteration level $k+1$,

$$Mx_{k+1} = Nx_k + b \tag{3.29}$$

The residual of each iteration is defined as,

$$r_k = b - Ax_k \tag{3.30}$$

After a given number of iterations, an approximate solution (x_{k+1}) is obtained as the residual (r_k) becomes smaller than the required tolerance. This residual can be conveniently written as (by subtracting Mx_k from each side of (3.30)).

$$r_k = M\delta_k \tag{3.31}$$

where $\delta_k = x_{k+1} - x_k$ is the correction after each iteration.

For an iterative method to be effective, the method must converge rapidly, which means that the iteration matrix M must be well conditioned. From the view point of matrix properties, the conjugate gradient (CG) method is one of the best choices. Preconditioning is also available to speed up the convergence.

The conjugate gradient method is restricted in that A must be symmetric and its eigenvalues must be positive (positive definite). The idea behind this method is to convert the original equation (3.27) into a minimization problem. The residual (r), where $r = b - Ax$, is minimized and expressed in term of the gradient of the minimization function. With the search direction function (p), the minimizing process

is guided in the right direction. Further details are provided in Ref. [86].

The conjugate gradient algorithm requires only the computation of scalar products and of matrix-vector products. A convergence criterion is based on the residual norm or on an iteration maximum (k_{max}). The convergence is, however, generally very slow, since the matrix A is not well conditioned. The number of iterations required is of order $O(n)$, where n is the number of nodes, $n = n_1 \times n_2 \times n_3$. This represents an unacceptable amount of work. The convergence rate of the conjugate gradient is determined by the spectrum of the eigenvalue of the matrix A [87]. It is then necessary to introduce a preconditioning of the system in order to achieve a more desirable distribution and improve convergence.

This is done by initially multiplying (3.27) by a *preconditoner* C. The preconditioned equation becomes $C^{-1}Ax = C^{-1}b$. The matrix C must be symmetric positive definite, and must be carefully chosen so that $C^{-1}A$ is well conditioned or has a more favorable spectrum of eigenvalues than A. Since C is symmetric positive definite, there is a nonsingular matrix $K \in \Re$, such that $C = KK^t$. The preconditioned conjugate gradient method is equivalent to the ordinary conjugate gradient method and is defined as,

$$\underbrace{K^{-1}AK^{-t}}_{\tilde{A}}\underbrace{K^t x}_{\tilde{x}} = \underbrace{K^{-1}b}_{\tilde{b}} \tag{3.32}$$

The derivation and implementation procedure of the preconditioned conjugate gradient method are documented in [86, 87, 88].

The selection of a good preconditioner C can have a dramatic effect on the rate of convergence and the CPU time. Details of each preconditioner are summarized in [87, 88]. However, numerical solutions indicate that in many situations the construction of C by a suitable incomplete Cholesky factorization (IC) of A is a good choice [88]. This

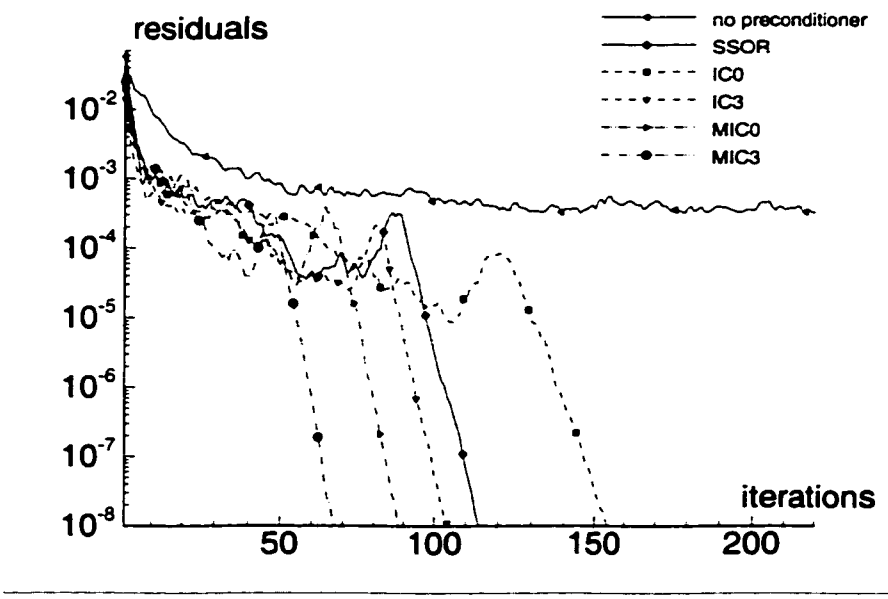

Figure 3.6: Typical convergence of the conjugate gradient method with various preconditioners [48]

factorization method can be modified to suit many different types of preconditioners, such as IC0, IC3, MIC0 and MIC3. Figure 3.6 shows the effect of convergence caused by various types of preconditioners. This result was obtained from the backward facing step flow [48] on a $114 \times 32 \times 24$ mesh with a convergence criterion of 10^{-12}.

Chapter 4

TWO-DIMENSIONAL SIMULATIONS

4.1 Introduction

In this chapter, two-dimensional simulations of both steady and unsteady flows over a bluff rectangular plate are presented at low and moderate Reynolds numbers.

The low Reynolds number simulations, which correspond to the steady laminar flow regime, were performed primarily to validate the computational procedure and determine the suitability of the spatial, temporal discretization and the linear equations solver. This, in turn, facilitated the optimization of the code for the subsequent complex flow simulations. The grid and computational domain specifications were also examined in the preliminary investigation. The second part of this chapter is devoted to two-dimensional unsteady flow at moderate Reynolds numbers. In this regime, the influence of flow dynamics and large scale unsteadiness is of greater in-

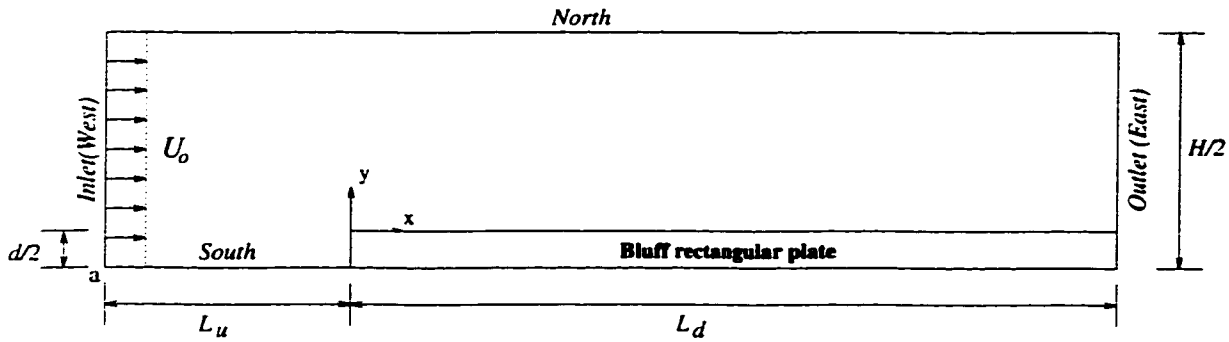

Figure 4.1: Computational domain for the two-dimensional simulations

terest, since they strongly affect momentum and scalar transport [4]. The results are compared with available experimental and numerical data, and the realism and validity of the two-dimensional assumption is assessed.

In the present investigation, the bluff rectangular plate is assumed sufficiently long so that there is no interaction between the upper and lower parts of the flow. Therefore it is only necessary to consider half of the flow field for the numerical simulations as shown in Figure 4.1. For the flow over a bluff rectangular plate, it is convenient to define a Reynolds number, $Re_d = U_o d/\nu$, based on the thickness of the plate (d) and the upstream uniform velocity (U_o). The other important parameter is the blockage ratio, defined as the ratio of the thickness of the plate to the height of the computational domain, $Br = d/H$. The origin of the Cartesian coordinates is on the leading edge of the plate. The distances from the leading edge to the inlet and outlet boundaries are defined as L_u and L_d, respectively.

Grid size	100 × 65	135 × 70	175 × 70	200 × 75
dx_c and dy_c	$\sim 0.025d$	$\sim 0.02d$	$\sim 0.01d$	$\sim 0.01d$

Table 4.1: Summary of the grid size and the grid spacing around the leading edge corner

4.2 Preliminary Computations

The two-dimensional simulations were initially performed at $Br = 10\%$ and Re_d of 250 and 1000. These simulations were performed in order to determine computational parameters, such as grid size and distribution, and the effect of the location of the inlet (L_u) and outlet (L_d) boundaries. A uniform flow velocity field was specified at the inlet(west) boundary. At the outlet(east) boundary, a zero-gradient boundary condition was specified for the $L_d = 20d$ case and an advective condition, $\frac{\partial U}{\partial t} + C_u \frac{\partial U}{\partial x} = 0$, was specified for the $L_d < 20d$. At the south and north boundaries, a symmetry condition was used. A no-slip condition was applied along the surface of the plate. The simulations were performed on a non-uniform grid and central differencing scheme (CDS) was used to discretize both convective and diffusive fluxes.

4.2.1 Computational Grid

A number of different types of grid distributions were investigated. The grid size used ranged from 100 × 65 to 200 × 75 grid points with L_u and L_d being $10.5d$ and $20d$, respectively. The grid expansion factor used for generating the non-uniform grids was

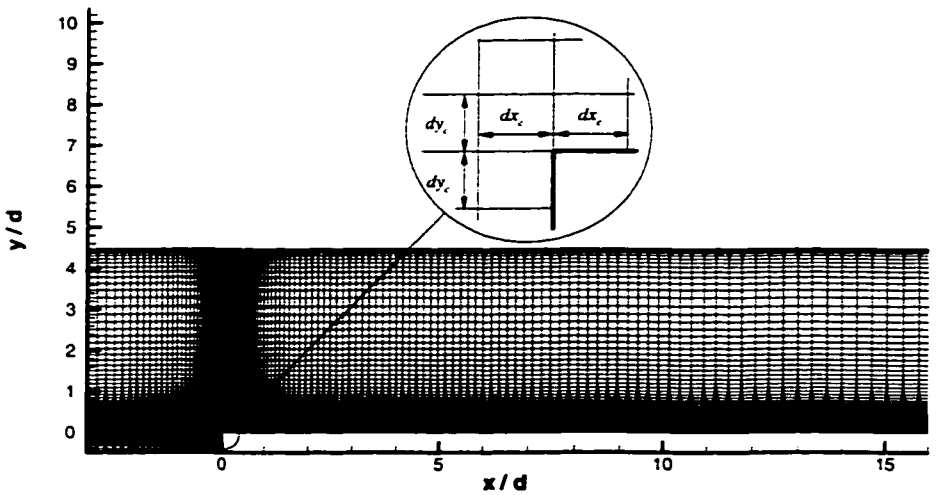

Figure 4.2: Typical grid distribution for the two-dimensional flows over a bluff rectangular plate: $Br = 10\%$

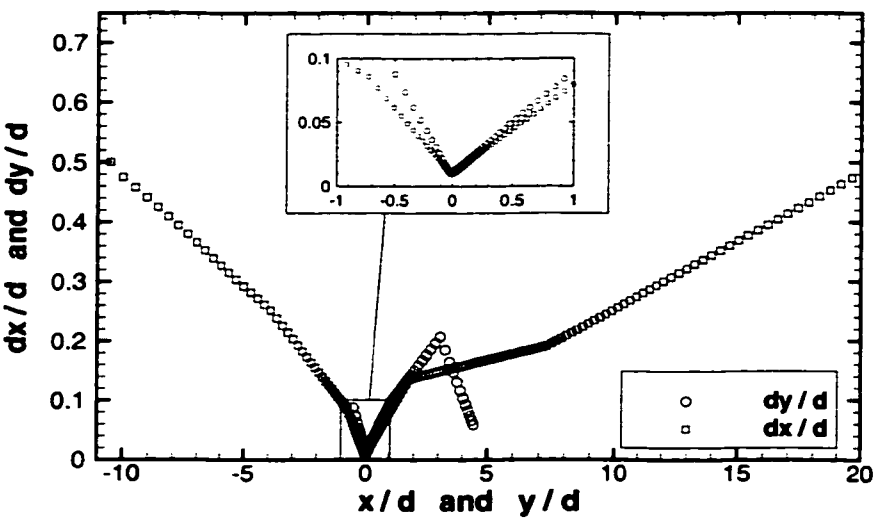

Figure 4.3: Grid distribution for 175 × 70 grid size

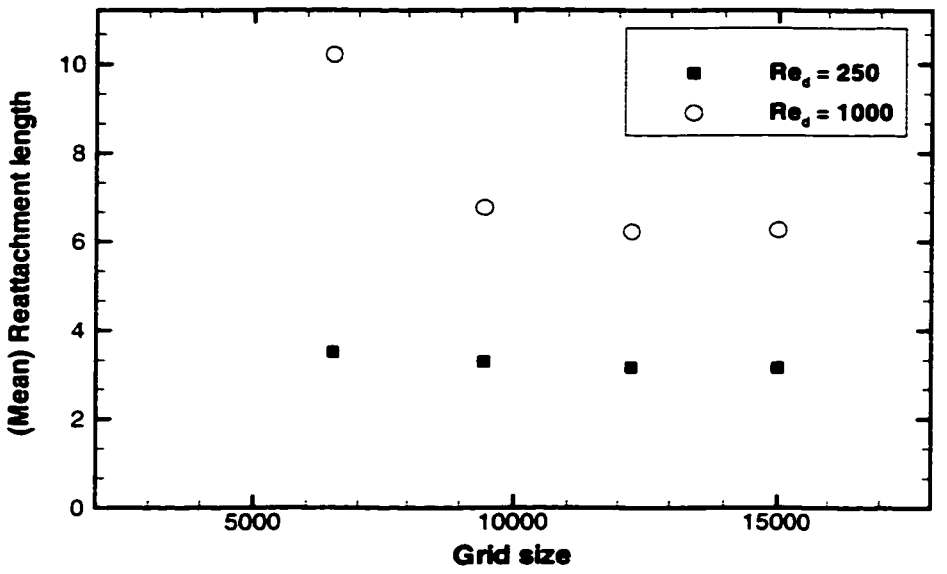

Figure 4.4: Effect of grid refinement on the (mean) reattachment length

kept close to one in both directions in order to avoid deterioration in the discretization scheme accuracy. At the leading edge corner, a cluster of fine, equally spaced grids was generated. A typical grid is shown in Figure 4.2 for part of the domain. The grid size and grid spacing around the leading edge are summarized in Table 4.1, and the grid distributions in the x and y directions are shown for one of the grids in Figure 4.3.

The effect of grid refinement on the predicted (mean) reattachment length (X_r or $\overline{X}_r$) is shown in Figure 4.4 for both steady laminar flow at $Re_d = 250$ and unsteady transitional flow at $Re_d = 1{,}000$. In this calculation the predicted (mean) reattachment length is measured from the leading edge corner to the downstream location where the wall shear stress is zero. For the steady laminar flows, increasing the grid

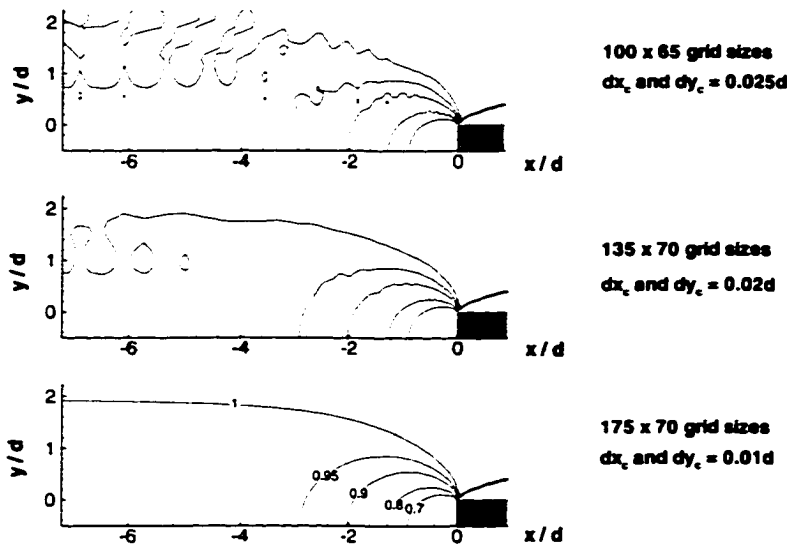

Figure 4.5: Numerical oscillations of streamwise velocity for various grid sizes of Re_d = 1,000

size from 100 × 65 to 175 × 70 results in a 9.5% difference. Further investigation with a 200 × 75 grid point shows a change of approximately less than 1% in the reattachment length. For the unsteady transitional flows, the mean reattachment length ($\overline{X}_r$) is obtained from the time-averaged value after the flow had become statistically stationary. The time-averaging was performed over 250 time units, where a time unit is defined as tU_o/d. A large difference in $\overline{X}_r$ of approximately 39% is obtained between the 100 × 65 and 175 × 70 grid sizes. However, the difference is very small between 175 × 70 and 200 × 75 grid sizes.

Due to the dispersive characteristic of the CDS, numerical oscillations are present in the coarser grid simulations. Such oscillations are predominant in the irrotational part of the flow immediately upstream of the plate where high gradients occur. Such oscillations become more evident with coarser grids at the higher Reynolds number

of 1,000 as shown in Figure 4.5, and a very fine grid, of approximately 1% thickness of the plate, is required to eliminate the numerical oscillations.

4.2.2 The Computational Domain Effect

The location of the inlet and outlet boundaries is an important consideration. A large computational domain results in unnecessarily large arrays, however a small domain can affect the accuracy of the solution in the region of interest. In this preliminary test, the location of the inlet boundary was investigated at $Re_d = 250$, on a non-uniform grid which had a fine grid spacing of $1\%d$ at the leading edge corner and a grid expansion close to one. A small difference of approximately 3% is found for the reattachment length if L_u was decreased from $10.5d$ to $4d$.

The location of the outlet boundary was also subjected to a preliminary test. The advective condition was applied to simulations with $L_d < 20d$. A difference of less than 0.25% is found for the reattachment length when L_d was shortened from $20d$ to $12d$. Several two-dimensional simulations were performed with the advective condition and the location of the outlet boundary was found to have no noticeable effect on the flow (typically less than 1%), provided $L_d > 2.5X_r$ (or $2.5\overline{X}_r$). This advective condition will be extensively used in future unsteady two and three-dimensional flow simulations, since it permits a smaller computational domain downstream of the leading edge.

4.3 Steady Laminar Flows

The steady laminar flow has been previously investigated both experimentally [1, 2] and numerically [3, 4]. The present simulations were performed over a range of Reynolds number, Re_d = 150-500 and blockage ratio, Br = 8.3 to 33%.

The computational domain was extended by $L_u = 5.5d$ upstream of the leading edge and $L_d \approx 2.5X_r$ downstream from the leading edge corner (the value of X_r was based on a previous numerical investigation by Djilali [3]). A non-uniform grid of 175 $\times$ 70 was used and two different discretization schemes were employed for the convective fluxes: QUICK and CDS. The following boundary conditions were used.

- Inlet(West): Uniform flow condition; (U_o).
- Outlet(East): Advective boundary condition; ($\frac{\partial U}{\partial t} + C_u \frac{\partial U}{\partial x} = 0$).
- North and South: Free-slip condition for velocity.
- Bluff plate: No-slip condition for velocity.

4.3.1 Results and Discussions

The expected quasi-linear variation of the reattachment length with the Reynolds number is clearly reproduced in Figure 4.6a, which shows both CDS and QUICK simulation results compared to the flow visualization experiment of Lane and Loehrke [2] and previous numerical results [3]. The variation of reattachment length with the Reynolds number is represented by $X_r \simeq 0.0236 Re_d$ for the CDS, with a slightly accentuated slope for the QUICK simulation ($X_r \simeq 0.0252 Re_d$). These slopes are comparable to the value of $\sim$ 0.024 obtained in [2]. The small difference between

numerical simulations and experiments can be attributed to the effective increase in blockage caused by the boundary layers on the solid walls of the experimental channel.

The effect of blockage ratio on the reattachment length is shown in Figure 4.6b. Increasing the blockage ratio reduces the size of the separation bubble and reattachment length. The reattachment length varies like $X_r/Re_d \simeq 0.0066$, 0.0117 and 0.0246 for blockage ratios of 33%, 20% and 10%, respectively, for the QUICK simulations. Typical streamline patterns are shown in Figure 4.7 for $Br = 10\%$. The simulations show that the maximum backflow streamwise velocities, which correspond to a minimum value of the stream function, are located in the first half and close to the middle of the separation bubble.

The pressure coefficient distribution along the surface of the plate is shown in Figure 4.8a for several Reynolds number at $Br = 10\%$. For a steady flow solution ($Re_d \leq 500$), a sharp drop of C_p at the leading edge corner is followed by an immediate pressure recovery. With increasing Reynolds number, the recovery is spread out over a larger distance as a result of the elongation of the separation bubble. After the maxima have been reached, the flow recovers and behaves like fully developed channel flow with a linear drop in C_p. At higher Reynolds number ($Re_d = 750$ and 800), the distribution is radically altered due to the onset of unsteadiness, as shown by instantaneous pressure distribution along the streamwise direction in Figure 4.8b. The pressure does not recover after separation and interestingly, the pressure distribution is first perturbed near the outlet boundary. As the Reynolds number is increased, this unsteadiness gradually propagates upstream until, eventually, the shear layer becomes unstable soon after separation. Unsteadiness is first observed around Re_d of 750 in the CDS simulations, but is delayed until Re_d around 950 in the QUICK simulations.

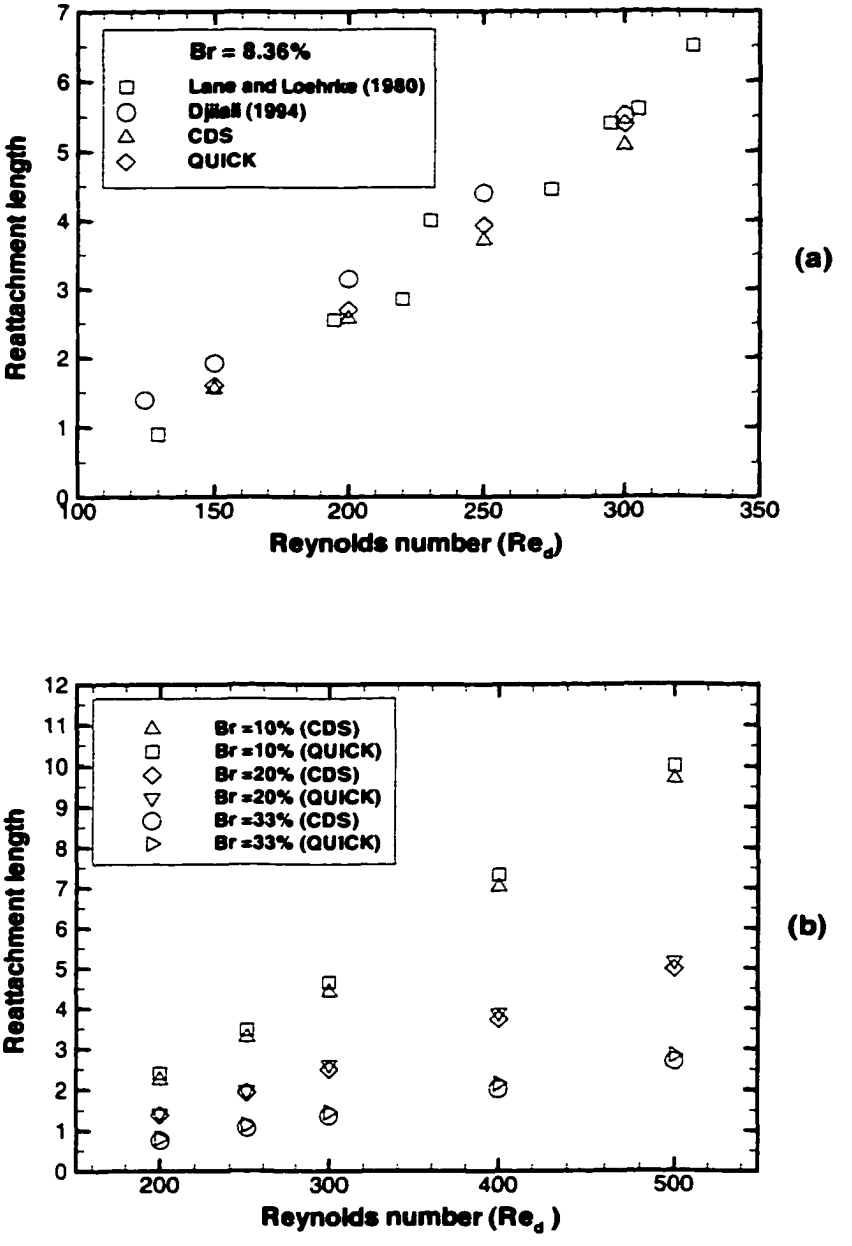

Figure 4.6: The variation of reattachment length for the steady and laminar flow

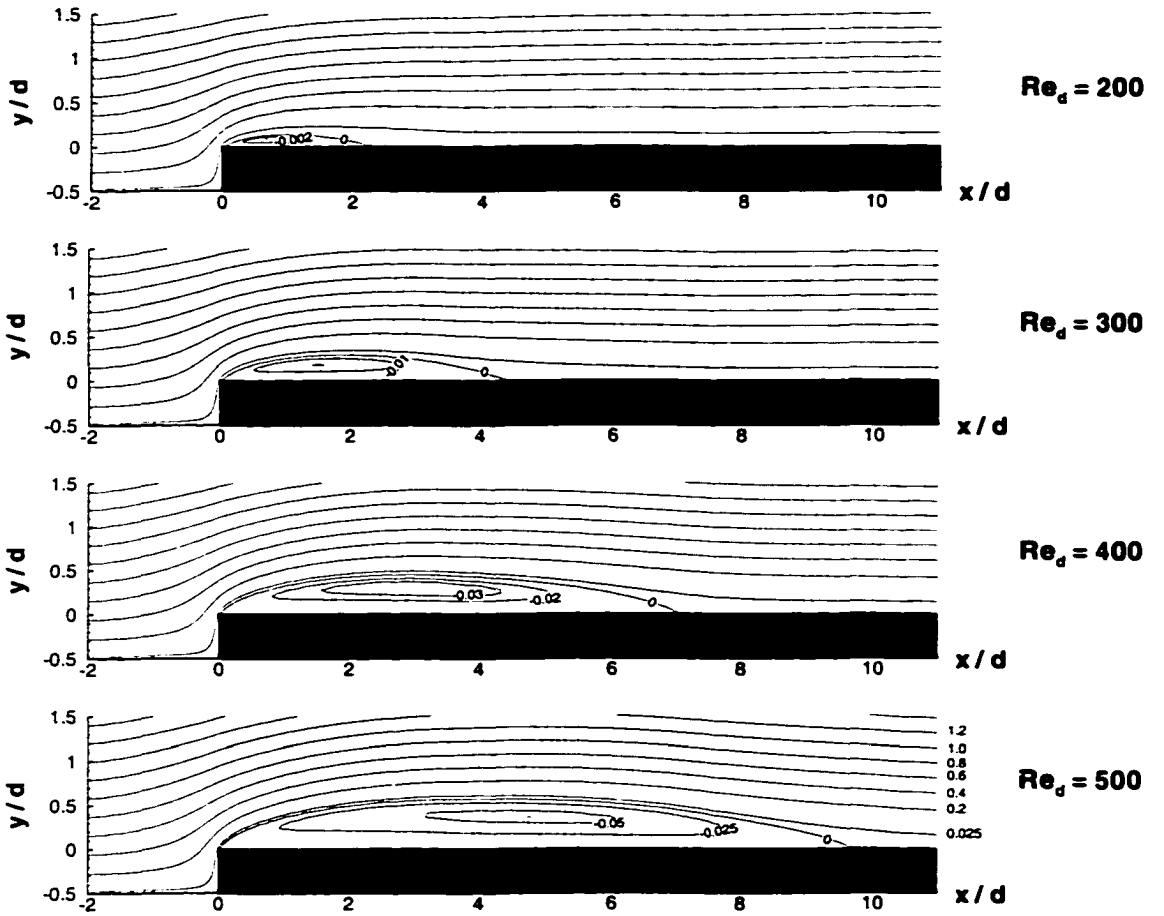

Figure 4.7: The streamline patterns for steady and laminar flow: $Br = 10\%$ (CDS simulations

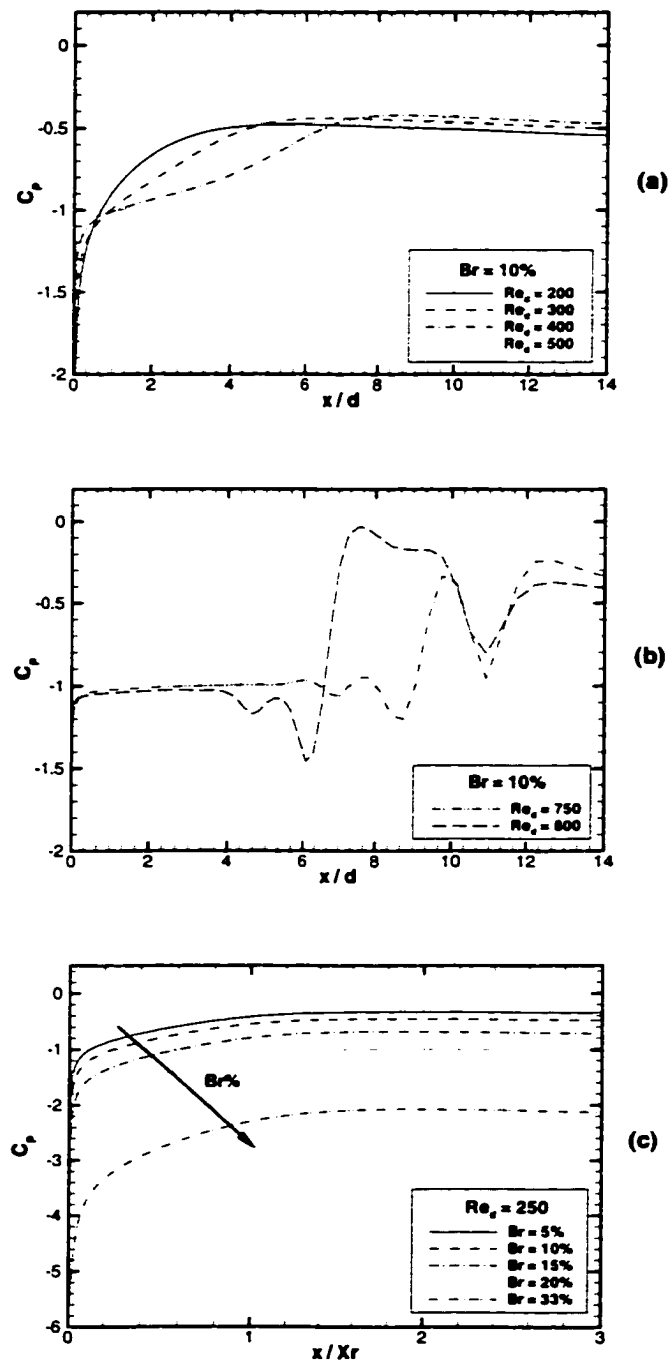

Figure 4.8: Pressure coefficient distribution along the surface of the plate (CDS simulations)

Figure 4.8c shows the effect of blockage on the predicted pressure distribution along the surface. Note that the streamwise distance was normalized by the reattachment length. Increasing the blockage reduces the pressure distribution in the flow field. This is due to the higher acceleration of the fluid in the higher blockage domain. The trends of C_p for different blockage ratios are similar and the maxima are located around $x/X_r = 1.75$ for $Re_d = 250$.

4.4 Unsteady Transitional Flows

The unsteady two-dimensional flow simulations were performed at a Reynolds number of 1,000 for a blockage ratio of 5.6%. This blockage corresponds to the high Reynolds number experiment in [12]. The computational domain was extended $5.5d$ upstream and $15d$ downstream of the leading edge corner. Both distances were found to be sufficient to simulate the unsteady flow with the advective outlet condition. Two non-uniform grids of 111×61 and 141×81 with a refinement of 1% around the leading edge were used. One of the purposes of the coarse grid simulations was to assess the adequacy of this resolution in the $x - y$ plane for the subsequent three-dimensional simulations. The boundary conditions are similar to the steady flow case except for the **north** boundary, which is set here as a no-slip wall to correspond with experimental conditions where a flow channel or wind tunnel wall is presented.

The pressure (Poisson) equation was solved using the direct method. For spatial discretization, the QUICK scheme despite its third order accuracy does not, in the context of unsteady flow simulations, perform as well as the second order CDS. It results in over-damping of the unsteadiness due to numerical dissipation [80]. The unsteady flow simulations presented in this section are therefore all performed using

the CDS.

The unsteady simulations yield instantaneous fields at each time step. In order to interpret and analyze these results and compare them to available experimental data, it is necessary to calculate statistical mean and fluctuating flow components. Let Q be any instantaneous local value,

$$Q = \overline{Q} + Q' \tag{4.1}$$

where $\overline{Q}$ is a local time average over the integration time, defined as,

$$\overline{Q} = \frac{\sum_{i=1}^{N} Q_i \Delta t_i}{\sum_{i=1}^{N} \Delta t_i} \tag{4.2}$$

and Q' is a local fluctuation component. The root mean square (r.m.s.) of the fluctuating component is obtained from,

$$\begin{aligned} Q'_{rms} = < Q' > &= \sqrt{\overline{(Q - \overline{Q})^2}} \\ < Q' > &= \sqrt{\overline{QQ} - \overline{Q}\,\overline{Q}} \end{aligned} \tag{4.3}$$

4.4.1 Results and Discussions

Time-Averaged Fields

The simulations were initialized for a period of $100tU_o/d$ in order to allow initial transients to convect out of the domain. Statistical sampling of the mean flows and r.m.s. values was then performed for $1100tU_o/d$. A time mean reattachment length ($\overline{X}_r$) of $6.29d$ was obtained for a grid size of 141 $\times$ 81 and a difference of

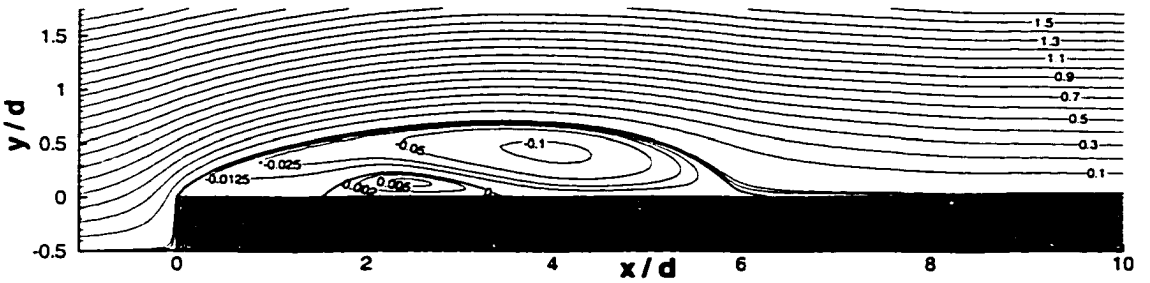

Figure 4.9: Time-averaged streamline pattern for the 141 × 81 mesh sizes

approximately 3% in $\overline{X}_r$ was found for the 111 × 61 mesh size. Both values were found to be consistent with previous numerical values obtained by Tafti and Vanka [4].

The time averaged streamline pattern is shown in Figure 4.9 for the 141 × 81 mesh size. It clearly shows that inside the main primary separation bubble, a small secondary separation bubble exists and is located in the first half of the primary separation bubble (extending from about x/d = 1.52 to 3.4). This unusual feature shows a small layer with positive mean velocity that corresponds to the positive shear stress shown in Figure 4.10.

The time averaged pressure distribution is shown in Figure 4.11 together with available high Reynolds number experimental data at Re_d = 50,000 [12]. This pressure distribution is defined in terms of the mean pressure coefficient (C_p) as,

$$\overline{C_p} = \frac{P - P_o}{1/2\rho U_o^2} \tag{4.4}$$

where P_o is the free stream pressure.

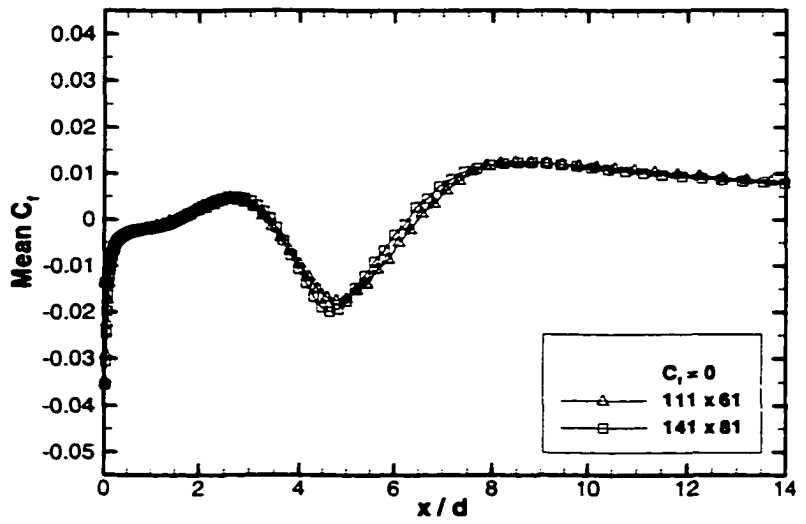

Figure 4.10: Time-averaged wall shear stress coefficient distributions

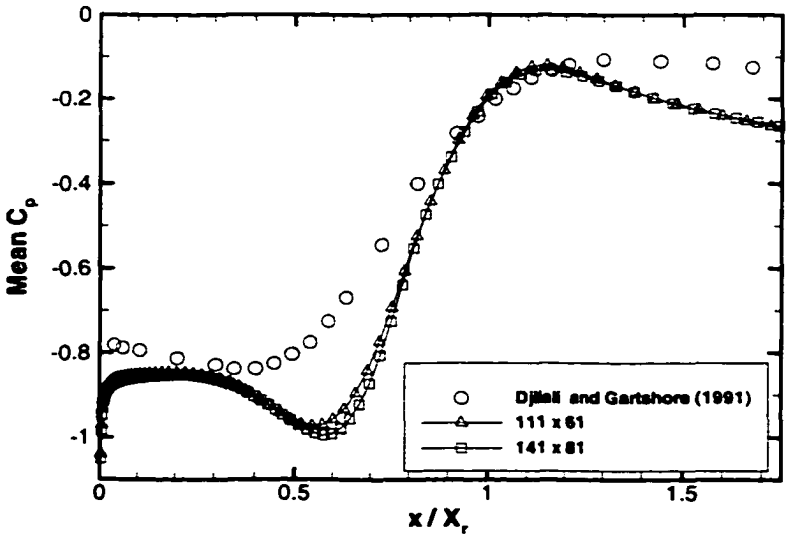

Figure 4.11: Time-averaged surface pressure coefficient distributions

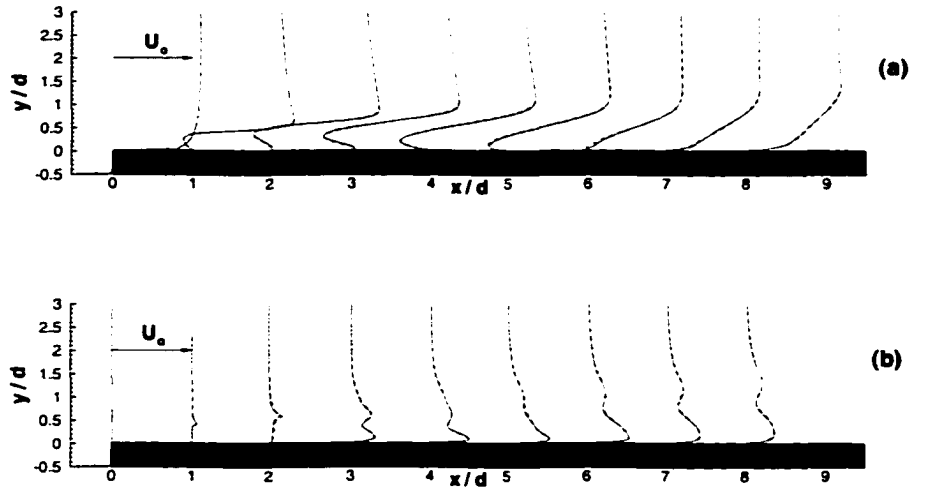

Figure 4.12: Time-averaged: (a) streamwise velocity profiles, (b) streamwise fluctuating velocity profiles; solid line for the 141 × 81 mesh; dashed line for the 111 × 61 mesh

The distributions are remarkably different from the steady case; a much larger low pressure region is maintained downstream of separation, and recovery is not initiated until $x/\overline{X}_r \approx 0.6$. The predicted C_p follows the same trends as the experiments, but with a much more pronounced minimum around the middle of the mean separation bubble. This strong suction peak is located close to the center of the primary recirculating flow region shown in the mean flow pattern.

Figure 4.12a shows the mean streamwise velocity profiles ($\overline{U}/U_o$) at several stations along the plate obtained with the two grids. The distributions are almost identical, indicating that a practically grid independent solution is achieved even with the coarser grid. In the recovery region, the mean velocity profiles show the distinctive boundary layer retardation characteristic of reattaching flows [16]. Both simulations predict a mean negative streamwise (backflow) velocity of $\overline{U}/U_o \approx 0.39$, at $x/d = 4.2$, which is about 18% higher than the value reported from high Reynolds number

measurement [12]. The mean streamwise intensity is shown in Figure 4.12b and the maximum occurs slightly upstream of the mean reattachment point.

Unsteady Flow Dynamics

Downstream of separation, the separated shear layer is subjected to the Kelvin-Helmholtz type of instabilities and eventually rolls up into a spanwise vortex. A typical cycle of vortex formation, merging, pairing and shedding is illustrated in Figure 4.13. At $\Delta t = 0$, the shear layer rolls up at about $x/d = 3$, while the previous vortex shed in the previous cycle is located at $x/d = 4.5$. At $\Delta t = 2$, the spanwise vortex becomes larger and extends close to $x/d = 4$. The pairing and merging is clearly shown at $\Delta t = 4$. The previous vortex begins to detach from the separation bubble and is shed into the faster moving flow. The coalescence process is completed at $\Delta t = 6$, while the previous vortex moves further downstream with a much higher advective velocity. A new cycle is started at $\Delta t = 8$, and is repeated in a pseudo-periodic fashion, with some cycles not exhibiting coalescing vortices.

The vortex fields can be clearly detected from the pressure signals. The strong correlation between the pressure and spanwise vorticity fields, illustrated in Figure 4.14, make it possible to identify the passage of the coherent vortical structures. The passage of a vortex at a given streamwise location can be identified by the suction peak of the pressure occurring at the same streamwise location. These pressure signals are used next for further analysis of the vortex dynamics.

The flow patterns and large scale unsteadiness of the flow are intermittent and it is useful to obtain information about scales and characteristic frequencies of the events while localizing these events in time. This is achieved by using wavelet transform

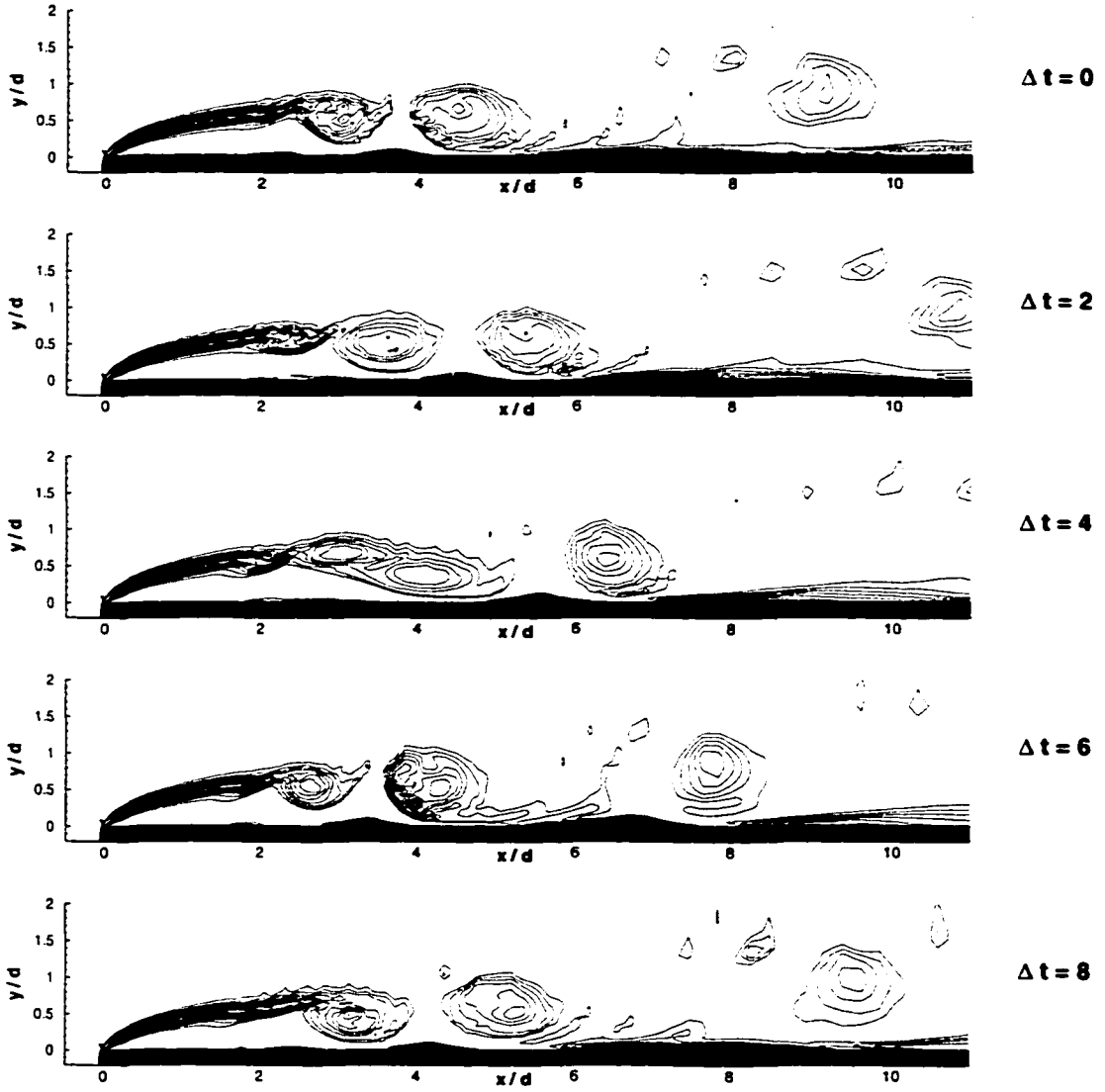

Figure 4.13: Spanwise vorticity contours at different time frames

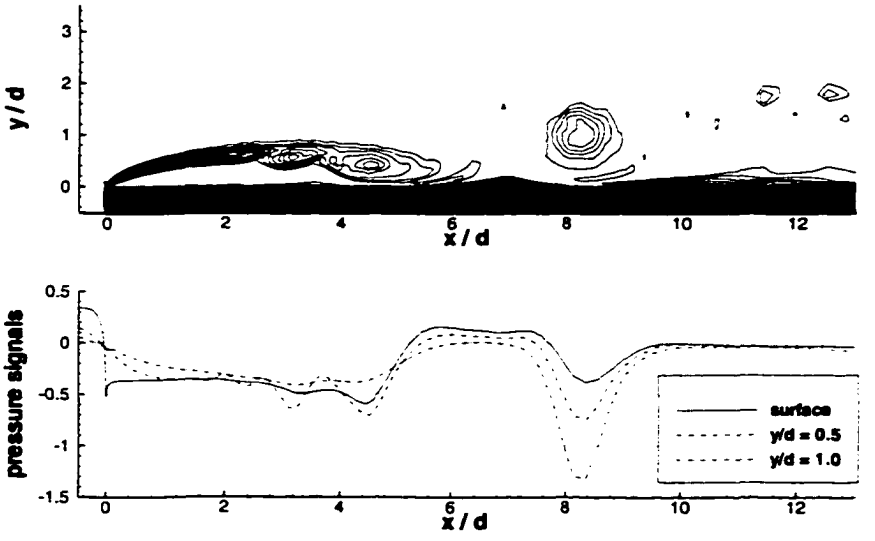

Figure 4.14: Instantaneous spanwise vorticity and pressure signals

analysis. This technique offers the advantage over classical (Fourier) spectral analysis of retaining temporal information and allows localization of intermittent events in time. An overview of the one-dimensional continuous wavelet transform is provided in Appendix B. Further details on the mathematical development of the method and its applications are available in [89]. The wavelet transform was applied to fluctuating pressure signals recorded at several locations downstream of the leading edge.

Figures 4.15a shows a pressure trace at $x/d = 2.0$ between 450-650tU/d. The energy distribution among the various frequencies can be visualized on the wavelet map in Figure 4.15b and 4.15c. The contour lines on both figures represent the high value of the wavelet coefficients. The resolution of the scales/frequencies and of time localization vary depending on the basis or mother function used in the wavelet transform. Here the Mexican wavelet, which provides good time localization and the Morlet wavelet, which provides good spectral resolution are used. With the

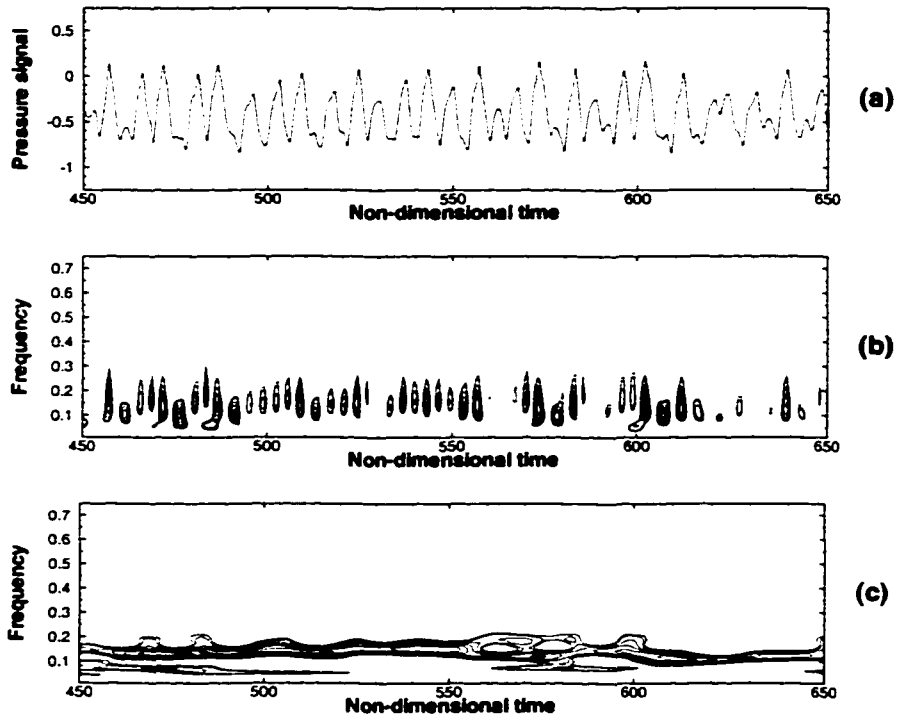

Figure 4.15: (a) Pressure signal at $x/d = 2.0$, $y/d = 0.5$, (b) Mexican wavelet map, (c) Morlet wavelet map

Mexican wavelet, the peak and the valley (the core of vortex) of the pressure signal are identified. The periodic pattern is clearly illustrated by a continuous contour line in Figure 4.15c.

The analysis of pressure signal in the reattachment region ($x/d = 6.0$) is presented in Figure 4.16. The concentration of energy is mainly around the non-dimensional frequency (fd/U_o) of 0.08-0.25 (or $f\overline{X}_r/U_o$ = 0.5-1.57). This frequency range corresponds to the dominant frequency characterising the large scale shedding from the reattachment region illustrated in Figure 4.13. This range of values is in agreement with those obtained from Tafti and Vanka's autocorrelation analysis [4]. The corre-

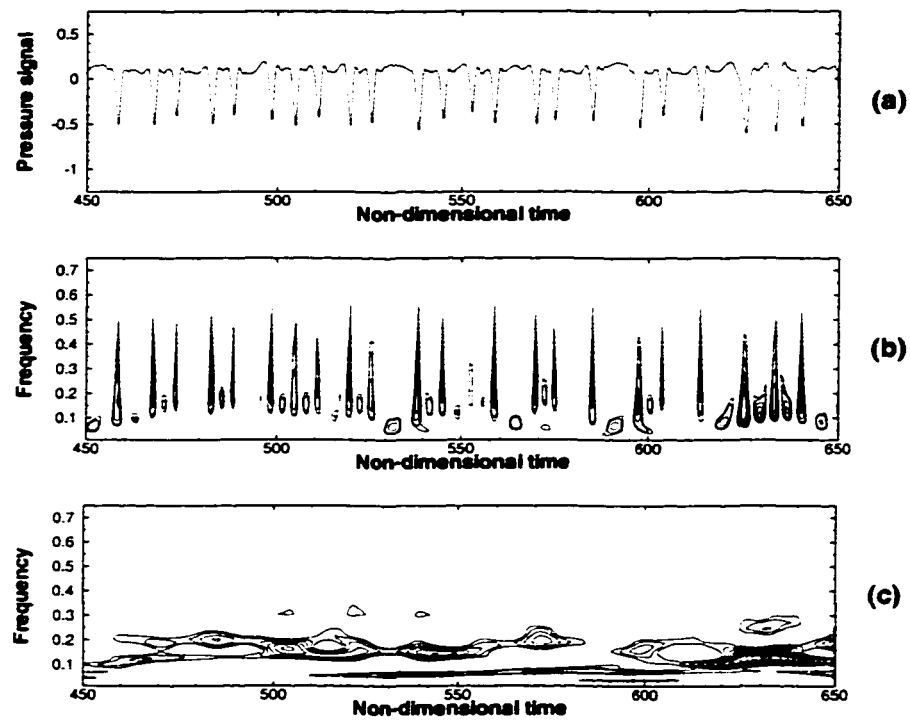

Figure 4.16: (a) Pressure signal at $x/d = 6.0$, $y/d = 0.5$, (b) Mexican wavelet map, (c) Morlet wavelet map

sponding Fourier and wavelet transform spectra are compared in Figure 4.17. The frequency peak obtained from both transforms is identical and is centered around the non-dimensional frequency (fd/U_o) of 0.15 (or $f\overline{X}_r/U_o = 0.94$).

4.5 Closing Remarks

The two-dimensional steady flow simulations reproduce well the reattachment lengths and the pressure distributions compared to previous experimental and numerical studies. The flow is altered by unsteadiness associated with the increasing Reynolds num-

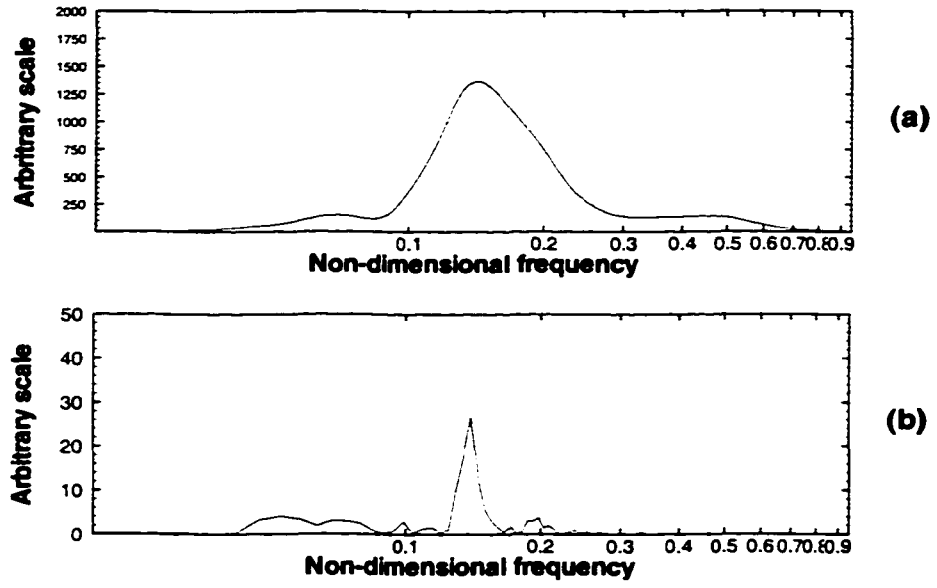

Figure 4.17: Mean power spectrum of pressure signal at $x/d = 2$, $y/d = 0.5$; (a) Wavelet (Morlet) transform, (b) Fourier transform

ber. Despite its third order accuracy, the QUICK scheme does not, in the context of unsteady flow simulations, perform as well as the second order CDS.

In unsteady flow simulations, the coarse grid of 111 $\times$ 61 provides an adequate resolution with small differences in $\overline{X}_r$ and almost identical mean streamwise velocity and fluctuating velocity profiles compared to the finer grid. Accordingly, the coarse grid will be used in future three-dimensional simulations.

The unsteady flow simulations provide an insight into the unsteady flow patterns which are difficult to observe experimentally, particularly in the complex and pseudo-periodic patterns of vortex formation, merging and shedding in the separated and reattaching flow region. The breakdown of the initial two-dimensional spanwise vortices, which is inherent to a turbulent field, is prevented. Hence, higher levels of mean

vorticity are likely to occur. This artificially strong vorticity would result in stronger suction peaks of the pressure distribution upstream of the reattachment region.

The two-dimensional simulations provide valuable insights into the dynamics of the flow. However it is unrealistic to expect more than qualitative agreement since inherently three-dimensional turbulent processes are not simulated. The three-dimensional simulations are promising and can provide valuable data and insights into the dynamics of the flow and the turbulent transport processes. Therefore, the three-dimensional numerical simulations will be investigated in the next chapter.

Chapter 5

THREE-DIMENSIONAL SIMULATIONS

5.1 Introduction

The two-dimensional results presented in the previous chapter provide some valuable insight into the dynamics of the flow, but their scope and realism is clearly limited due to the inherent three-dimensionality of the flow. In this chapter, we present, assess and analyze three-dimensional simulations using the direct as well as large eddy simulation approaches. As discussed in the introduction, DNS requires the resolution of all scales of motion and is therefore confined to moderate Reynolds number (Re_d = 1,000) corresponding to the unsteady transitional regime. LES's are presented first for moderate Reynolds numbers and then for the high Reynolds number flow case (Re_d = 50,000) corresponding to the experiments of Djilali and Gartshore [12]. The performance of three subgrid scale models namely the structure function model

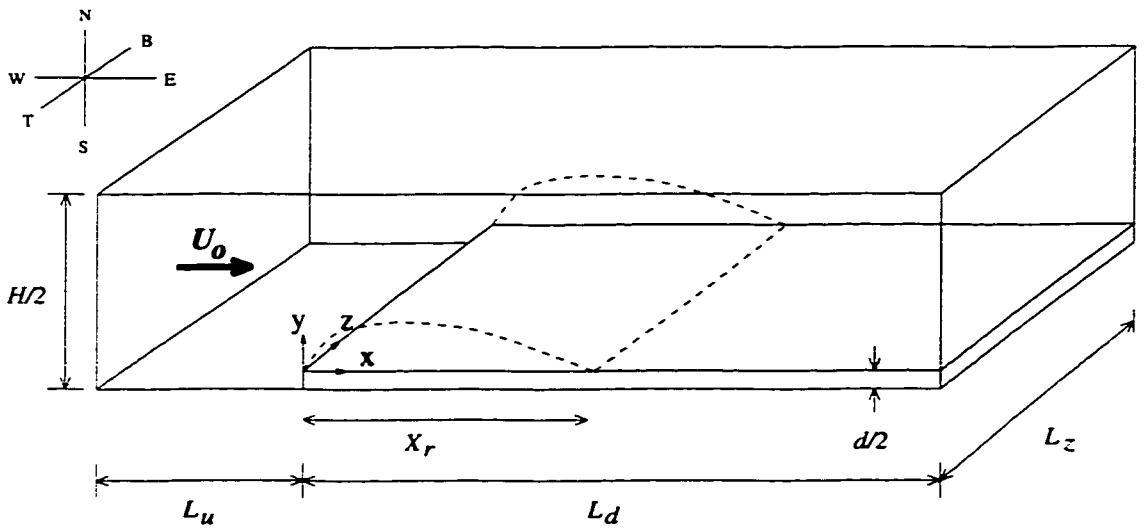

Figure 5.1: Computational domain for the three-dimensional simulations

(SFM), selective structure function model (SSFM) and the Smagorinsky model (SM) is examined in terms of mean flow statistics and dynamic features, and further analysis is performed using coherent structure identification tools and wavelet transforms.

5.2 Computational Domain

A schematic of the three-dimensional flow domain is shown in Figure 5.1. As in the two-dimensional case, the origin of the Cartesian coordinates is defined on the leading edge and the top surface of the plate. The distances from the leading edge of the plate to the inlet and outlet boundaries, L_u and L_d, and the spanwise dimension of the domain, L_z, are given in Table 5.1 together with the grid sizes employed for the two Reynolds numbers.

In both regimes, the extent of the domain downstream of the leading edge (L_d), is

Re_d	L_u	L_d	L_z	Br	grid
1,000	$5.5d$	$14d$	$6d$	5.6%	$111 \times 61 \times 31$
50,000	$4d$	$12d$	$5.2d$	5.6%	$108 \times 61 \times 27$

Table 5.1: Summary of computational domain parameters for the three-dimensional simulations

more than 2.5 times the mean reattachment length, based on previous experiments of Ota *et. al.* [1], for $Re_d = 1{,}000$, and Djilali and Gartshore [12], for $Re_d = 50{,}000$. The spanwise dimension (L_z) is also a very important parameter. With periodic boundary conditions in the spanwise direction, the movement of the large scale structures present in the flow can be artificially limited and eventually lead to a large deviation in the mean reattachment length [90]. Accordingly, the present value for L_z is set to over twice the spanwise correlation length obtained from the measurements of Saathoff and Melbourne [7].

The blockage ratio was selected to be identical with [12]. Due to the limitation of computer resources, the grid sizes were limited, and non-uniform mesh distributions were applied in the x and y directions with grid spacings of the order of $0.01d$ in the vicinity of the leading edge. A uniform mesh was applied in the z direction with a spacing of $\Delta z = 0.2d$. The mesh distributions used in the $x - y$ plane are similar to those for which "grid-independent" simulations were obtained in two-dimensional cases.

5.3 Boundary Conditions

The boundary conditions are summarized below,

- Inlet (West): Uniform flow condition; (U_o).
- Outlet (East): Advective boundary condition; ($\frac{\partial U}{\partial t} + C_u \frac{\partial U}{\partial x} = 0$).
- South: Free-slip condition for velocity (upstream of the plate).
- Top and Bottom (spanwise direction): Periodic conditions.
- North and Bluff plate: No-slip velocity (moderate Reynolds number) and wall function conditions (high Reynolds number).

Approximate wall functions, as described in Section 2.4, are used on all solid boundaries for the LES at high Reynolds number. Though known to be inadequate for separated flows, this kind of treatment is currently unavoidable at high Reynolds numbers.

5.4 Numerical Parameters

The second order central differencing scheme (CDS) has been shown to be more effective than upwind biased schemes for DNS and LES type computations [15] since the use of upwind methods introduces dissipation into the simulations [91]. At high Reynolds numbers, however, CDS can generate spurious oscillations in the high gradient region immediately upstream of the leading corner of the plate if the mesh is not fine enough. Accordingly, a mixed discretization is adopted for the convective fluxes whereby: CDS is used downstream of the leading edge of the plate to ensure that the simulations in the zone of interest are free from numerical dissipation; and

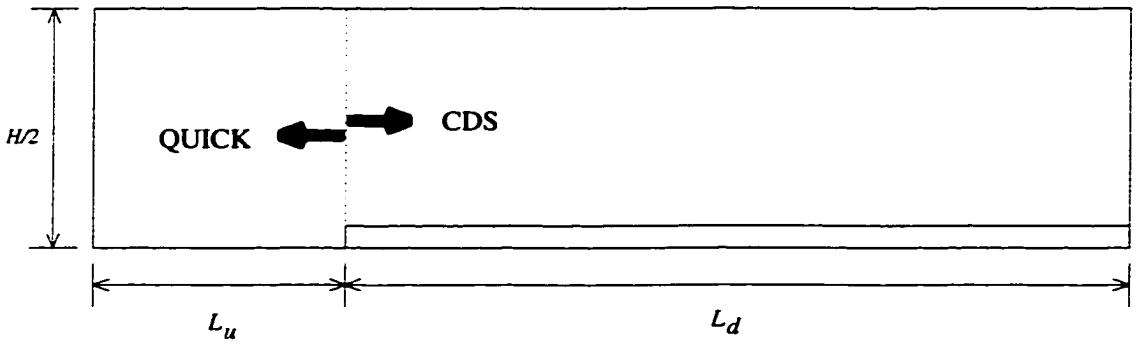

Figure 5.2: Mixed spatial discretization in two-dimensional configurations

a quadratic upwind scheme (QUICK) is used in the region upstream of the plate to avoid the aforementioned numerical oscillations. This discretization procedure is illustrated in Figure 5.2 and used for the high Reynolds number case only (Section 5.6). Testing of this procedure at moderate Reynolds number (Re_d = 1,000) has shown that it does not alter the dynamics and statistics of the simulations.

The efficient preconditioned conjugate gradient method is used in all three-dimensional simulations for the solution of the Poisson equation.

5.5 Unsteady Transitional Flows: Re_d = 1,000

The flow at Re_d = 1,000, corresponds to the unsteady, transitional regime observed experimentally by Ota *et al.* [1]. The simulations were performed using both DNS and LES approaches. In LES, the SSFM subgrid scale model was used. This model has the advantage of being able to localize small scale turbulence and is shown in Section 5.6 to have better performance than the two other models investigated in this study.

Simulations	SGS model	Sampling times (tU_o/d)	$\overline{X}_r/d$
DNS	-	1100	6.85
LES	SSFM	600	6.16

Table 5.2: Mean reattachment length and sampling time for both direct numerical and large eddy simulations

5.5.1 Mean Flow Statistics

The mean quantities are obtained by averaging in both time and spanwise direction. The mean reattachment lengths ($\overline{X}_r/d$) obtained from both simulations are given in Table 5.2, together with the corresponding sampling times. Initial conditions for both simulations were generated from stationary two-dimensional simulations at the same Reynolds number. The instantaneous two-dimensional fields (U and V) were used for each plane in the spanwise direction while the spanwise velocity (W) was set to zero everywhere. Statistical sampling of the mean flow field and mean turbulent quantities was not started until $\tau = 100tU_o/d$ in order to allow the passage of initial transients to be convected out of the domain. The integration times presented here are exceptionally long and correspond to about 78 and 42 "flow-through" times for DNS and LES, respectively. The time step for both simulations is varied and constrained with the CFL condition, resulting in time steps of the order of $0.008tU_o/d$ for DNS and $0.006tU_o/d$ for LES.

In the case of DNS, a value of 6.85 is obtained for $\overline{X}_r/d$ and while this is higher

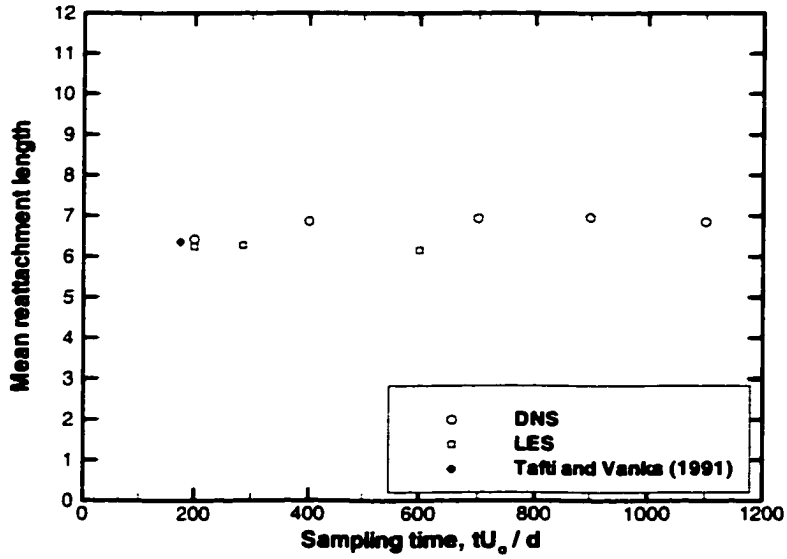

Figure 5.3: The mean reattachment length variations with sampling time

than the value of 6.36 reported by Tafti and Vanka [15] from their DNS, their integration time was much shorter. Figure 5.3 shows that about the same value of $\overline{X}_r$ is obtained at $\tau = 200$, but that $\overline{X}_r$ does not actually stabilize before $\tau = 400$, when it reaches a value of 6.85. This shows the need for long periods of integration, corresponding to about 30 flow-through times, for the simulations to attain stationary flow conditions. The persistence of initial transients is probably due to the long residency time of flow particles in the recirculating flow region. Various measurements compiled by Ota *et al.* [1] show values of $\overline{X}_r/d$ in the range of 4.0-5.0 at $Re_d = 1,000$. A mean reattachment length of 6.16 is obtained from the LES and is in better agreement with [1] than the DNS, although is still high. In addition to large experimental uncertainties, other factors that may have contributed to the difference are blockage ratio and levels of free-stream turbulence.

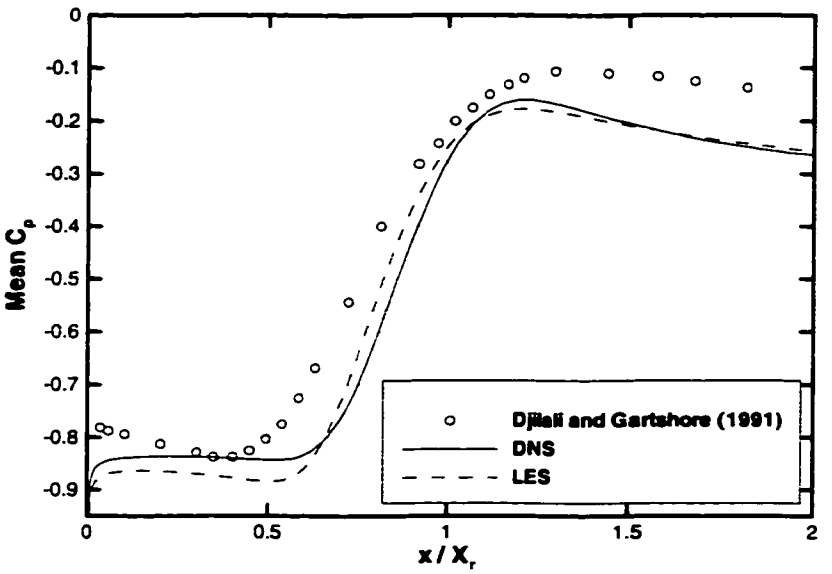

Figure 5.4: Distribution of mean surface pressure coefficient; high Reynolds number measurements are also plotted for reference

The distribution of the mean surface pressure coefficient is shown in Figure 5.4. Both DNS and LES distributions exhibit similar behavior, with an approximately constant pressure throughout the first 60% of the mean separation bubble. No experimental data is available at this Reynolds number. For reference the data for Re_d =50,000 [12] is plotted, but it should be emphasized that the flow regimes corresponding to two Reynolds numbers are different and hence detailed agreement is not expected. The simulations do not exhibit the distinct suction minimum at Re_d = 1,000, and while recovery begins further along the channel, a faster recovery rate is exhibited by both DNS and LES, and maxima are reached at $x/\overline{X}_r \approx 1.2$. The three-dimensional pressure distributions are much more realistic than those obtained from two-dimensional simulations, Figure 4.11, which exhibit a unphysically large

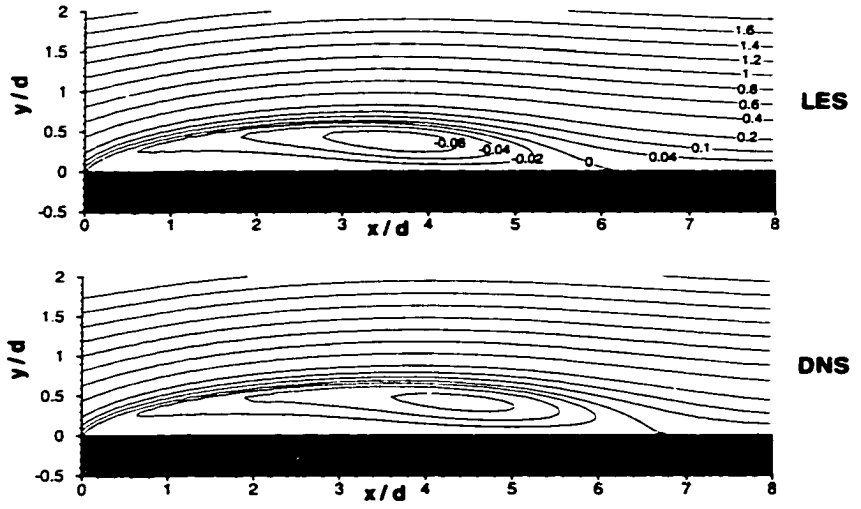

Figure 5.5: The mean streamline patterns for three-dimensional unsteady transitional flows

minimum as a result of the strong coherence enforced by two-dimensionality.

The mean streamlines are shown in Figure 5.5 and clearly show the center of the recirculation zone is further upstream in the case of LES; this is true even when the location is non-dimensionalized with respect to $\overline{X}_r$. This location corresponds to the location where the pressure recovery begins. The streamline pattern does not show any indication of a secondary separation bubble noted in [15] and a detailed examination of the shear stress and mean velocity distributions confirm this. Such a secondary separation might have been an artifact of the coarser resolution of the near-wall flow in [15].

The predicted mean streamwise velocity distributions are presented in Figure 5.6 at six locations covering the separation bubble, the reattachment region and the recovery region. The mean reattachment length is used to normalize both x and y coordinates. Again the experimental profiles obtained from [12] at $Re_d = 50,000$ are

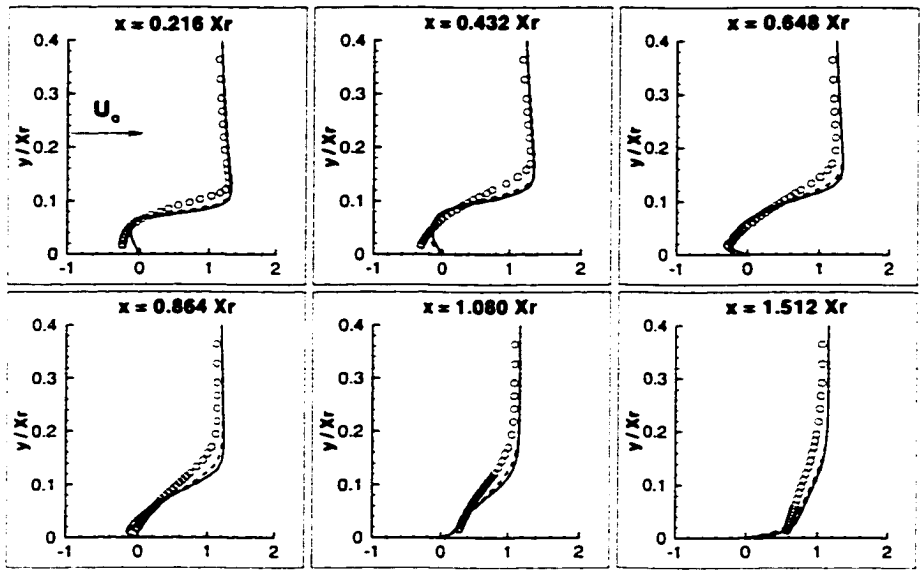

Figure 5.6: Mean streamwise velocity (U/U_o) profiles for various locations along the plate: Experimental ($Re_d = 50,000$) [12], circle; DNS, solid line; LES, dashed line

plotted for indicative purposes. In the first half of the separation bubble, the backflow velocities of the transitional regime (simulated) are noticeably lower than the fully turbulent regime (experimental). It is believed that these differences are physically representative of the dependence of the flow on Reynolds number, since a previous three-dimensional numerical simulation, at the same Reynolds number [15], yielded similar distributions, and the simulations at Re_d = 50,000 presented in the next section yield very good agreement with experimental observations. The simulated backflow velocities also reached approximately the same maximum of -0.3U_o in the region $x/\overline{X}_r$ = 0.6-0.7. Although the simulated and experimental profiles were from different regimes, they are similar downstream of the reattachment region, exhibiting an inflection point characteristic of reattaching boundary layers slowly recovering to equilibrium conditions.

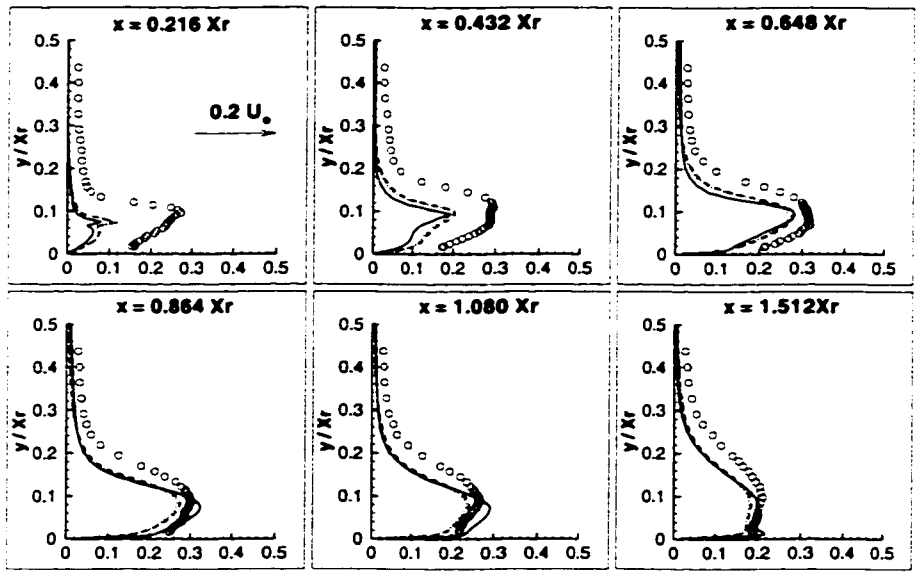

Figure 5.7: Mean streamwise turbulent intensity ($< u' > /U_o$) profiles for various locations along the plate: Experimental ($Re_d = 50,000$) [12], circle; DNS, solid line; LES(Total), dashed line; LES(Resolved), dotted line

While there is little difference between the DNS and LES mean velocity profiles the effect of the SGS model is much more evident in the fluctuating velocity profiles shown in Figure 5.7. Both resolved and total (resolved + SGS) contributions are plotted for the LES case. It is noted that normalizing the mean turbulent intensity with a longer $\overline{X}_r$ for the simulations causes the profiles to shift toward the wall. As expected, the LES and DNS intensities at the first two stations, $x/\overline{X}_r = 0.216$ and 0.432, are much lower than the high Re_d experimental value, since transition takes place immediately after separation at $Re_d = 50,000$, whereas the instabilities in the separated shear layer develop over a longer distance for the case of $Re_d = 1,000$.

Interestingly, the deficit in mean turbulent intensity is regained by $x/\overline{X}_r \simeq 1.5$ indicating that the dynamic processes controlling turbulent energy production in the

reattachment zone is similar at both Reynolds numbers. The profiles also indicate that the simulations are well resolved; the modeled contributions of the SGS are essentially zero at $x/\overline{X}_r = 0.216$ and 0.432, and remain minimal even in the recovery zone where the grid is coarser. Although the SGS contribution to turbulent intensities is small, the overall effect of the SGS model on the resolved scales is noticeable.

In addition to the change in the evolution of the turbulent intensities with streamwise distance, there is also a near-wall peak obtained with the DNS at $x/\overline{X}_r = 1.512$ but not with the LES. This peak is similar to that observed in the highly resolved DNS of the low Reynolds number flow over a backward facing step [92]. The suppression of this feature in the LES indicates inadequate near-wall behaviour of the SGS model. Overall the turbulent intensities are lower than those obtained by Tafti and Vanka [15], but, as noted earlier, their simulation time was probably too short and furthermore the spanwise extent of their domain was smaller than in the present simulations.

Typical instantaneous contours of the eddy viscosity are shown for the LES in Figure 5.8. Consistent with the previous discussion, negligible eddy viscosity is introduced in the flow for $x/d < 2$. However the intensity profiles of Figure 5.7 show substantial differences between DNS and LES, even for locations close to separation. This is probably due to the combined effect of (a) the feedback of upstream influences via the recirculating flow patterns; and (b) the alteration of the dynamics of the flow by the eddy viscosity.

As described earlier, the grid spacing is gradually increased downstream of the leading edge of the plate. Consequently, the grid Peclet number increases, and with it the dispersive effect of the central differencing scheme. This may explain the faster

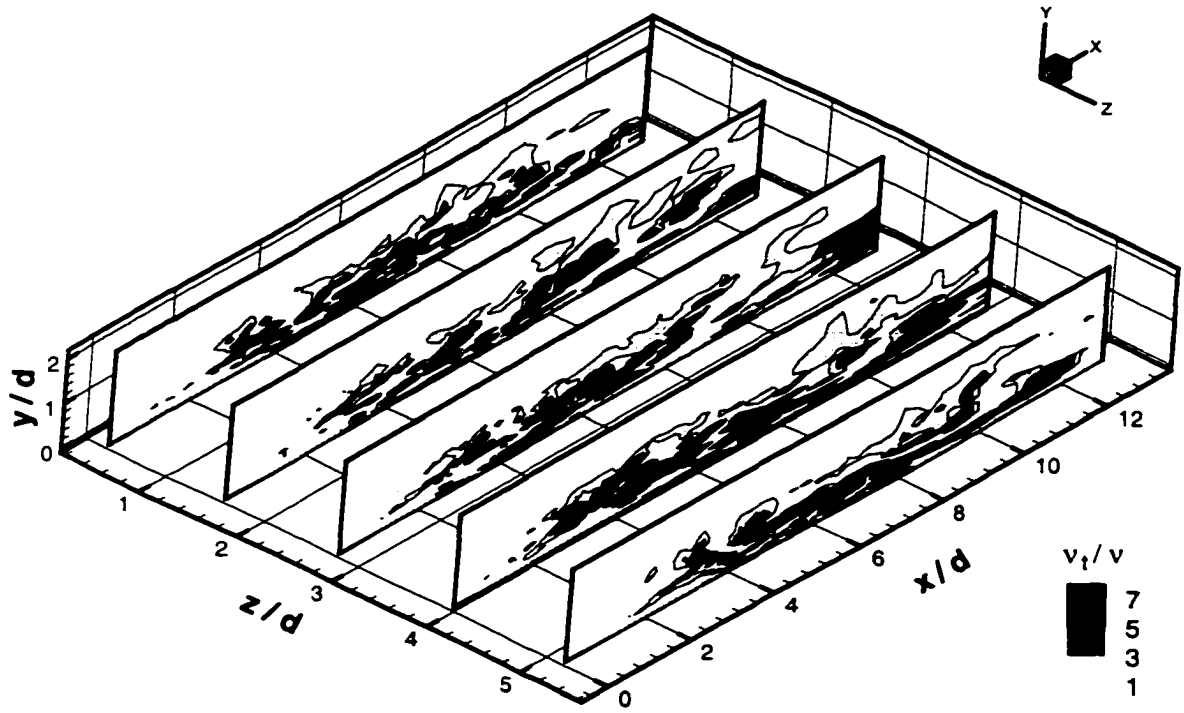

Figure 5.8: Normalized instantaneous eddy viscosity contour (ν_t/ν) in $x-y$ plane: 4 levels of 1, 3, 5 and 7

rate of increase of turbulent intensities with downstream distance in the DNS. One of the roles of the SGS model appears to be a dampening of this effect. The dampening provided by the selective structure function model is of the correct nature since, overall, the turbulent intensity levels and their streamwise evolution computed using LES are in better agreement with experimental observations at $Re_d = 50{,}000$ [12] and since recent low Re_d measurements of Hwang *et al.* [24] show substantially lower turbulent intensities than the high Re_d flow of [12].

5.5.2 Flow Structures and Dynamics

In the initial transient period ($\tau < 100tU_o/d$), the flow structures are clearly identified by the vorticity. The flow dynamics at this stage are similar to that of the free mixing layer [32] and the backward facing step flow [47], and are characterized by a Kelvin-Helmholtz type instability. Figure 5.9 shows quasi two-dimensional spanwise vortices shed downstream of the leading edge and longitudinal vortices of alternating sign stretched by the flow. Figure 5.9a clearly shows that the growth of spanwise instability and the formation of secondary hairpin vortices stretching between primary Kelvin-Helmholtz rolls. It also shows a quasi two-dimensional pairing of two spanwise vortices at the location between x/d = 2-3.

The pairing and the hairpin vortices play an important role in the transition process toward three-dimensionality. The hairpin vortices become stronger as the flow progresses in time and leads to the break-up of the spanwise vortices. The counter rotation of the hairpin vortices tends to generate three-dimensionality, while the pairing of the spanwise rolls tends to counter it. This phenomenon has been observed previously by Bernal and Roshko [93] in plane mixing layers. Figure 5.10 shows the instantaneous spanwise vorticity at about 50 time units from the initial "start-up". The two-dimensional spanwise vorticity begins to break up into smaller three-dimensional structure, but traces of two-dimensional structures can still be identified at about x/d = 2.75 and 4.0.

Rapid amplification of three-dimensional disturbances leads to the stretching and break-up of the quasi two-dimensional structures. Instantaneous spanwise vorticity fields from both DNS and LES are shown in Figure 5.11. The vorticity is initially two-dimensional and concentrated in the separated shear layer, which in the case

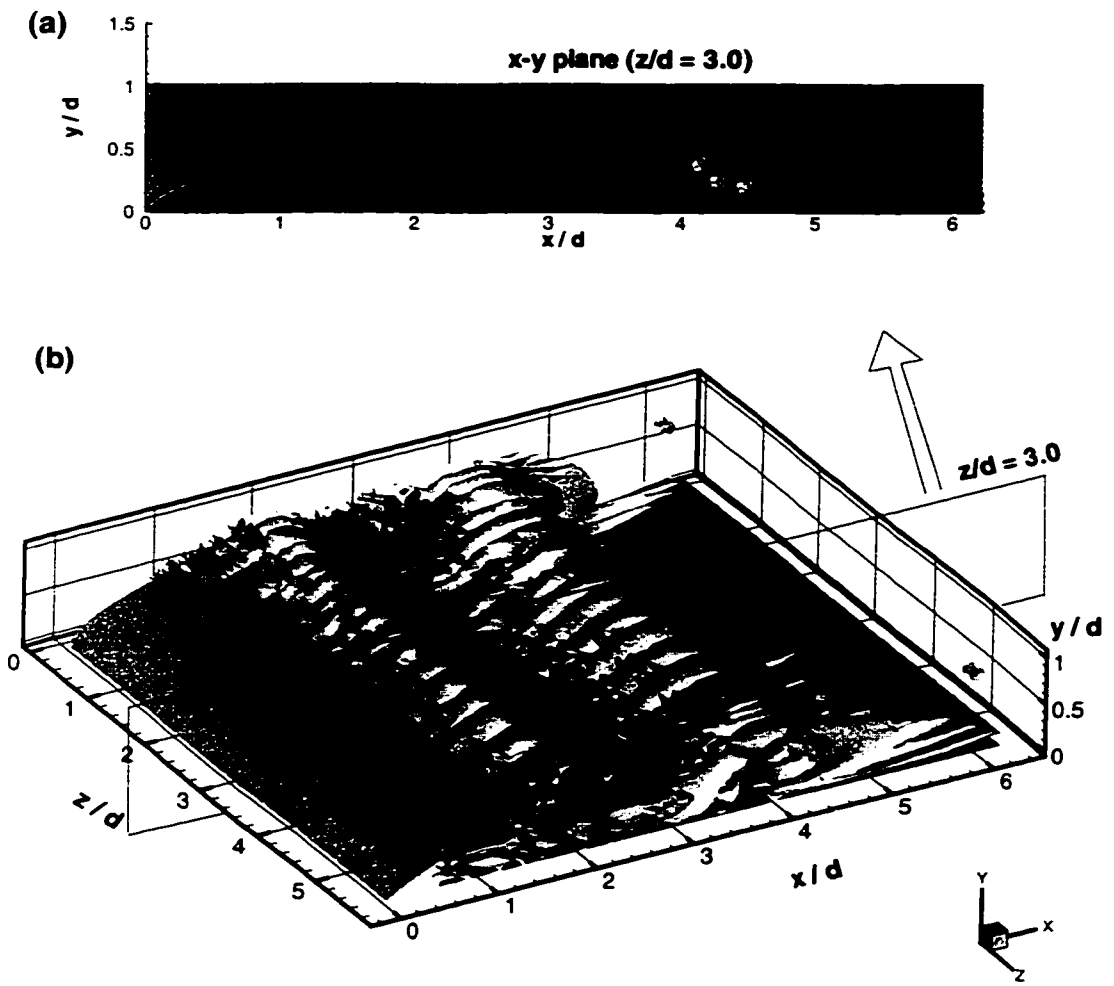

Figure 5.9: Instantaneous spanwise and streamwise vorticity interaction from the DNS at the beginning of the "start-up" period ($\approx$ 15 time units): (a) $x - y$ plane ($z/d = 3.0$). (b) 3-D volume

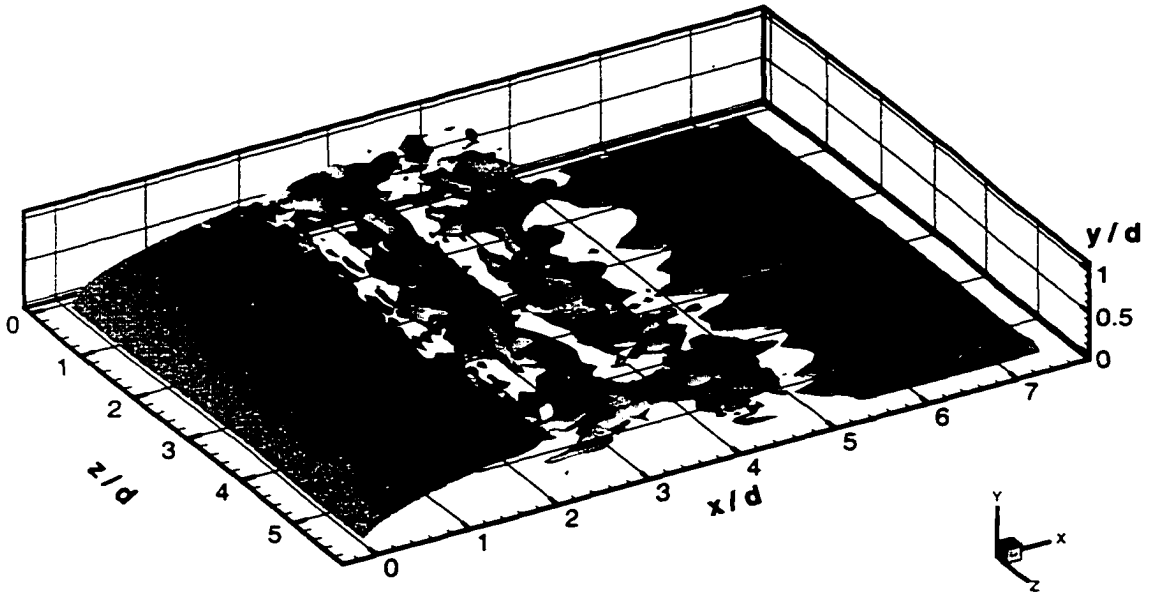

Figure 5.10: Relief plot of instantaneous spanwise vorticity from the DNS which indicates the starting of the break-up process ($\approx$ 50 time units): ω_z = -6U_o/d

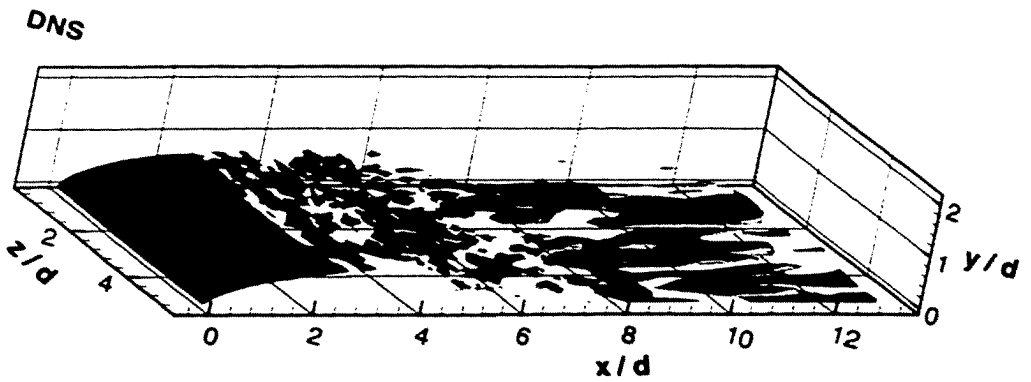

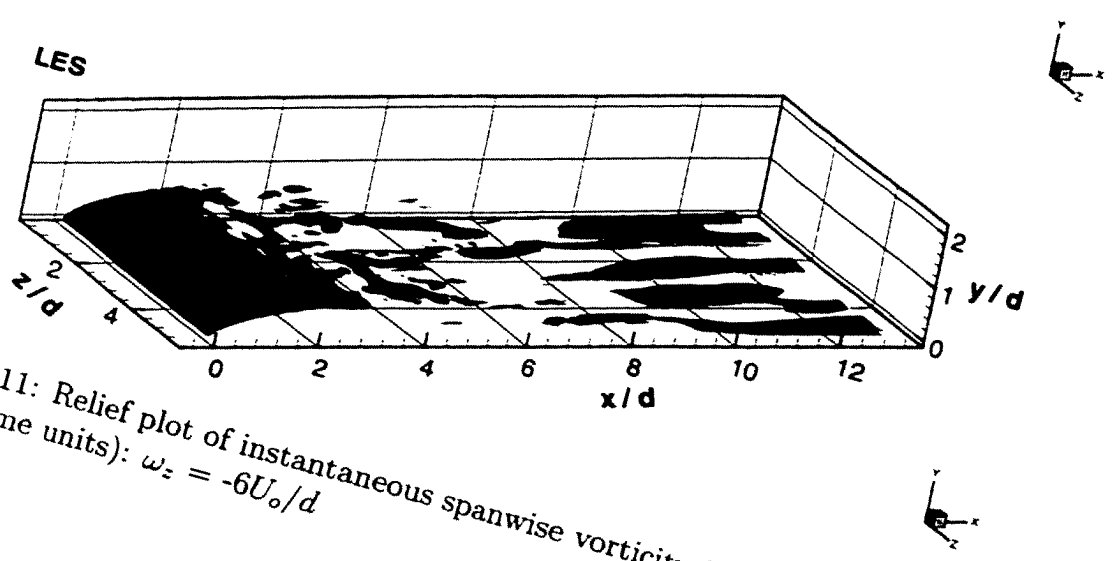

Figure 5.11: Relief plot of instantaneous spanwise vorticity from both DNS and LES ($\approx$ 100 time units): $\omega_z = -6U_o/d$

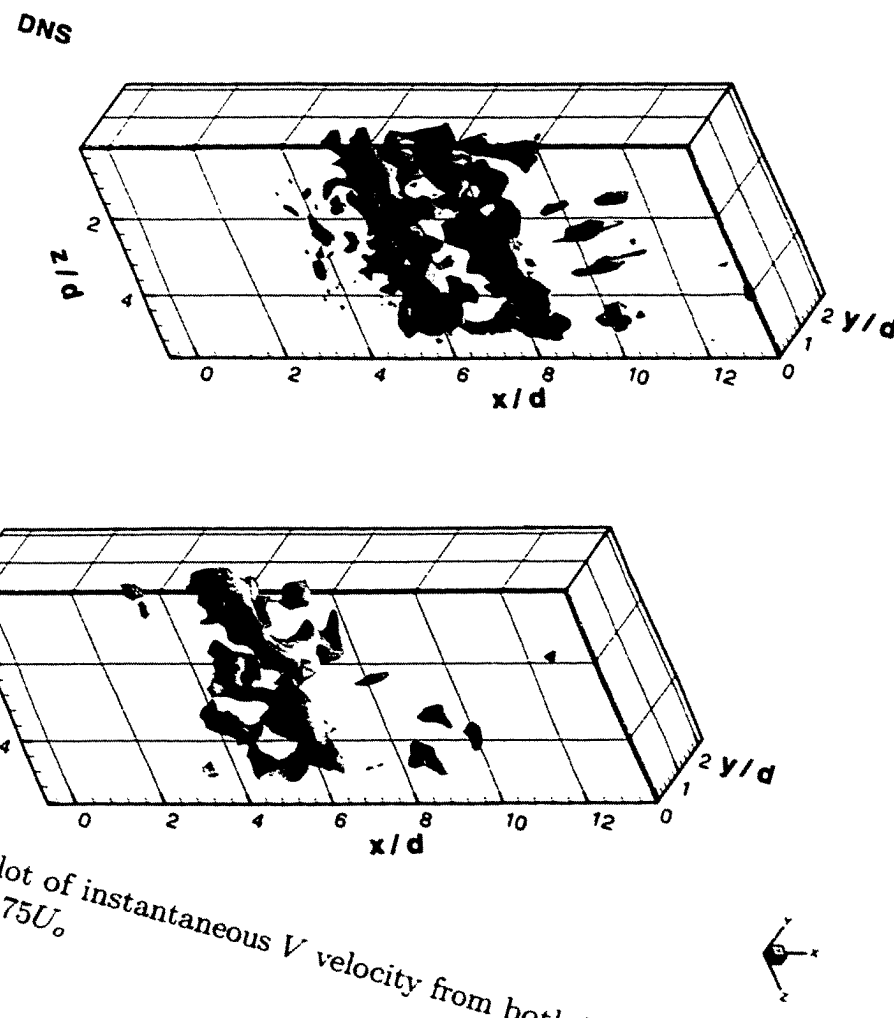

Figure 5.12: Relief plot of instantaneous V velocity from both DNS and LES (≈ 100 time units): $V = -0.175U_o$

of DNS remains stable up to $x/d \approx 2.5$, at which point the shear layer rolls up. In the case of LES, disturbances in the shear layer are evident much earlier, and the break-up process is less sudden. Complete three-dimensionalization occurs at $x/d \approx 2$, at which point the selective structure function model starts to produce appreciable levels of eddy viscosity as shown earlier in Figure 5.8. The earlier onset of instability in the case of LES results, naturally, in higher fluctuating velocities producing the higher turbulent intensities presented in Figure 5.7. In the second half of the separation bubble ($2.5 \leq x/d \leq 5$), the dissipative effect of the SGS model is evident. The small scale structures, clearly visible in DNS, are suppressed in LES, and only larger elongated structures remain. In this region, the DNS produces higher velocity fluctuations as shown in Figure 5.12. Further downstream, in the recovery region $x/d \geq 8$, the vorticity is primarily produced at the surface of the plate in a pattern of alternating, elongated streak-like shapes. The effect of near-wall dissipation is evident in the LES.

In the reattachment zone, the flow is characterized by pseudo-periodic shedding of large scale structures, which are ejected into the free stream and convected downstream. This process is accompanied by cyclic growth and shrinkage of the separation bubble and meandering of the instantaneous reattachment point. This is illustrated by the time history of the flow direction index presented in Figure 5.13. The data is sampled at a location close to the mean reattachment point. Note that, at this location, on average, the negative flow phases (long reattachment) have a longer duration than the positive flow phases (short reattachment). This may be interpreted as follows: with the gradual growth of large scale vortices in the separated shear layer, the reattachment point moves gradually downstream; when a large scale structure is shed, the bubble "collapses" and the reattachment length moves rapidly upstream.

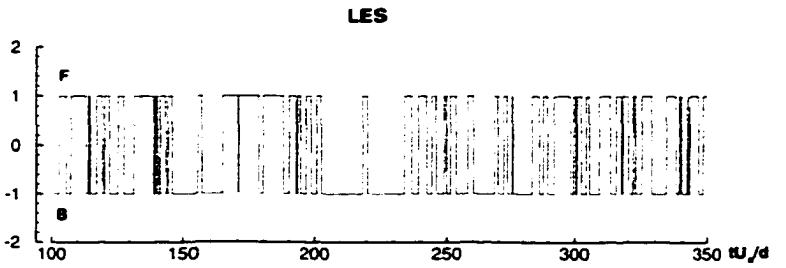

Figure 5.13: Trace of the streamwise velocity component at the surface indicating the flow direction index (F = Forward. B = Backward): $x/d = 6.18$ and $z/d = 3$

The pseudo-periodic cycle is then repeated.

The corresponding Fourier transform spectra of surface pressure and spanwise velocity signals are presented in Figure 5.14. The frequency ranges, labeled by **A, B, C** in both spectra, indicate three distinct phenomena occurring downstream of the leading edge. The most distinct range, **A**, is centered around $fd/U_o = 0.015\text{-}0.0175$ (or $f\overline{X}_r/U_o = 0.092\text{-}0.107$) and appears in both the surface pressure and the spanwise velocity signals. This frequency range is associated with the "low-frequency flapping" of the shear layer, resulting from the cyclic growth and shrinkage of the separation bubble, and is in good agreement with the range of frequencies deduced from high Reynolds number experimental observations [12, 14].

The second frequency range is much broader and accounts for a large portion of the turbulent kinetic energy. This frequency range, labeled **B**, corresponds to the main vortex shedding from the reattachment region. The highest frequency range, **C**, ($fd/U_o \approx 0.25\text{-}1.0$) is more prevalent along the separated shear layer (Figure 5.14b) than in the reattachment region, and is related to the shedding frequency of the separated shear layer.

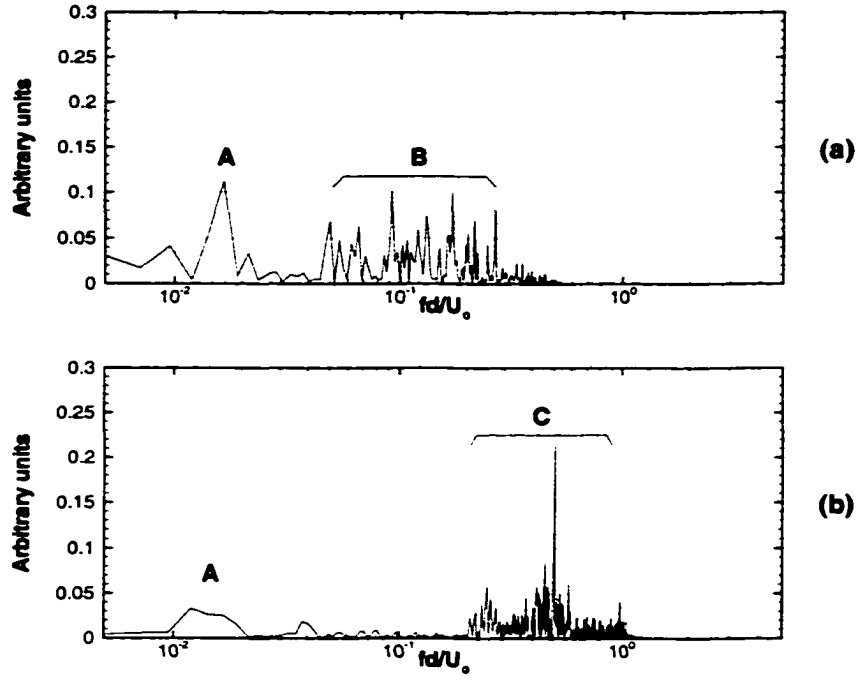

Figure 5.14: Fourier spectrum of: (a) surface pressure at $x/d = 4.0$, mid-span; (b) spanwise velocity at $x/d = 2.057$, $y/d = 0.672$, mid-span (LES)

A useful tool for further elucidating the dynamics of the flow is the wavelet transform analysis. This allows the characterization of unsteady signals in the frequency/scale and time domains simultaneously, and provides not only spectral information, as in Fourier analysis, but also localization of events in time (see Appendix B for details). A map of the wavelet coefficient showing the energy associated with various scales at various times is presented in Figure 5.15 for both simulations. We note the suppression of the small scales in the LES, whereas energy containing time-scales (period) of order of $0.5tU_o/d$ are present in the DNS wavelet map.

The reoccurrence of peaks with scales (periods) of about $10tU_o/d$ (i.e., $log\{\text{scale}\}$ ≈ 1) and $5tU_o/d$ ($log\{\text{scale}\} \approx 0.7$) correspond to the experimentally observed period

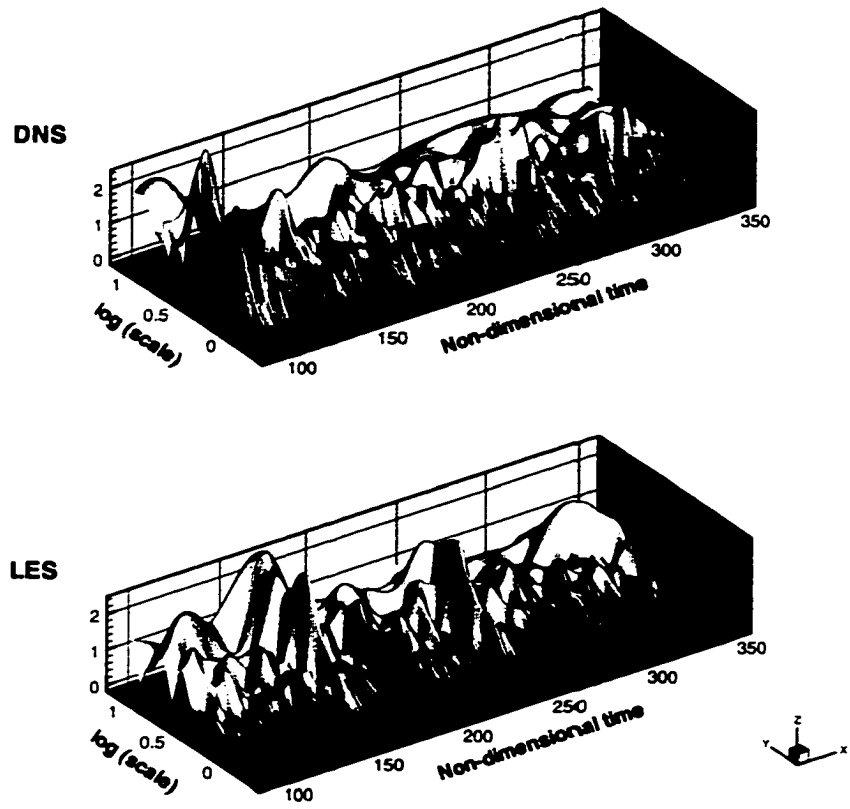

Figure 5.15: Morlet wavelet map of streamwise velocity at $x/d = 6.18$ and $y/d = 1.03$; $z/d = 3$ (mid-span). $log(tU_o/d)$ is plotted on the scale (y) axis to increase resolution of small scales

of vortex shedding from the bubble and its first harmonic. These periods correlate well with the instantaneous flow direction shown in Figure 5.13 and the Fourier transform spectra shown in Figure 5.14a (**B** range). The evolution along the time axis illustrates the pseudo periodic nature of this process. A high energy peak in the large scales is identifiable in the LES at about 170 time units and corresponds to the clear pattern of reattachment length oscillations of duration approximately $10tU_o/d$ shown in Figure 5.13 between 150 and 190 time units.

Simulations	SGS models	Sampling times (tU_o/d)	$\overline{X}_r/d$
3DSF	SFM	400	5.14
3DSSF	SSFM	400	4.30
3DSM	SM	400	4.57
Expt. [12]	—	—	4.7± 0.1

Table 5.3: Mean reattachment length and sampling time for the high Reynolds number large eddy simulation

5.6 Unsteady Turbulent Flows: $Re_d = 50{,}000$

All simulations of this Reynolds number were performed using LES. The Reynolds number of 50,000 corresponds to the turbulent separation and turbulent reattachment regime. For flow over a bluff rectangular plate, this regime is Reynolds number independent [1] ($Re_d \geq 22{,}000$) and it has been the subjected of a number of experimental studies [5, 6, 7, 9, 10, 11, 12, 14]. Three SGS models are used (SFM, SFFM and SM) and the performance of these models is evaluated and a detailed analysis of the mean and dynamic characteristics of the flow is presented.

5.6.1 Mean Flow Statistics

The mean reattachment lengths obtained with the three SGS models are given in Table 5.3, together with the sampling time for each model. The time step is varied and constrained with the CFL condition, but is of the order of $0.006tU_o/d$ for 3DSF and 3DSM and $0.003tU_o/d$ for 3DSSF. Simulations over an initial "start-up" period

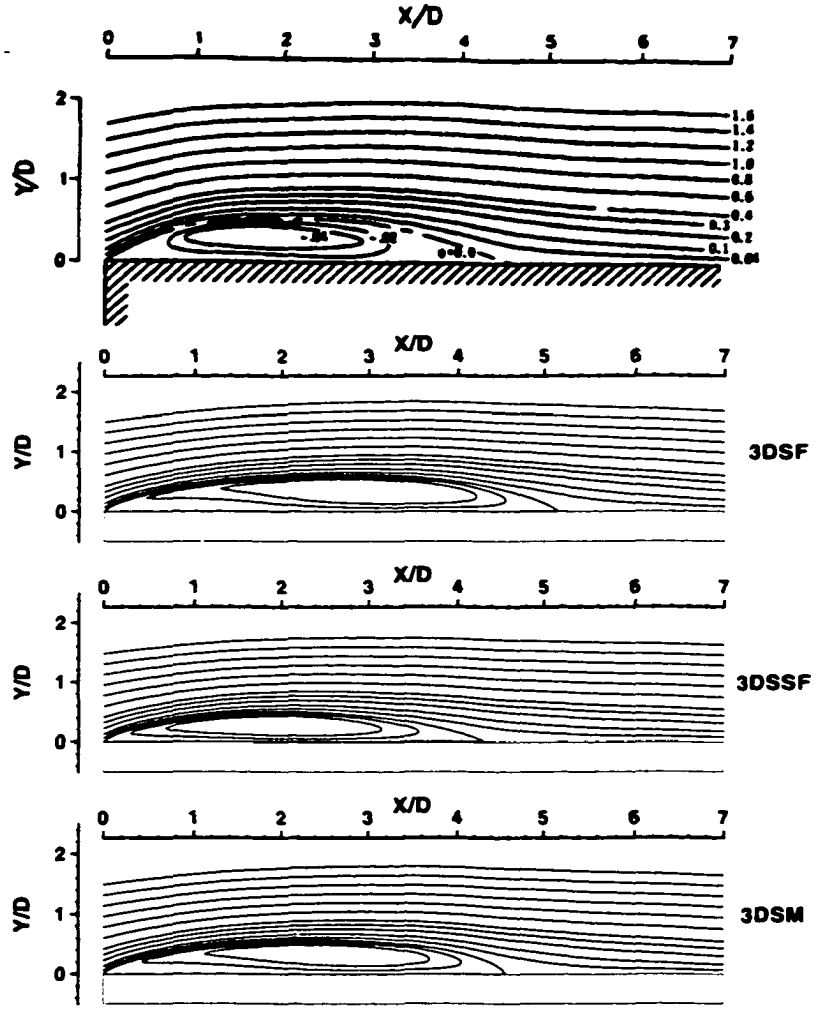

Figure 5.16: The spanwise and time-averaged streamline patterns for the unsteady-high Reynolds number flows: (the top streamline pattern is from experimental studies of [12])

of about $50tU_o/d$ were discarded to allow the passage of initial transients. Initial conditions were taken from the three-dimensional instantaneous flow fields of the DNS at $Re_d = 1{,}000$. Subsequently, all simulations were integrated over $400tU_o/d$ (about 35 "residence" times). These exceptionally long integration times are required for this flow to attain stationary conditions, as discussed in the previous section. The spanwise and time-averaged streamline patterns from all three simulations are compared with experiment in Figure 5.16. Although 3DSM provides the best prediction of $\overline{X}_r$, the streamline pattern compared to experiments is skewed, with the location of the center of the mean recirculating vortex located too far downstream. The mean flow pattern of 3DSSF provides better overall agreement with experiment with both the shape and the location of the centre of recirculation well predicted.

Figure 5.17a compares predicted mean surface pressure distributions along the surface of the plate. The experimental trend is reproduced reasonably well by all three simulations. The minimum mean surface pressure coefficients are underpredicted by about 10 to 18 percent, depending on the SGS models, however the 3DSSF provides better agreement with the location of the minimum at $x/\overline{X}_r \approx 0.4$ and the recovery rate afterwards. The strength and location of the surface pressure minima is coupled with the vorticity in the mean separation bubble. Figure 5.17b shows that the pressure minima are located approximately at the centre of the recirculation vortex in the streamwise direction and about $y/\overline{X}_r = 0.08$ in the normal (y) direction. The recovery process for all three SGS simulations is completed by $x/\overline{X}_r \approx 1.35$, which is identical to experimental observations [12]. Downstream of the recovery region ($x/\overline{X}_r \gtrsim 1.35$), the flow is dominated by the redeveloping boundary layer which takes place under a slightly negative streamwise pressure gradient. We note a slight underprediction of the surface pressure coefficient of 3DSSF in this region. Figure 5.18 compares simulated

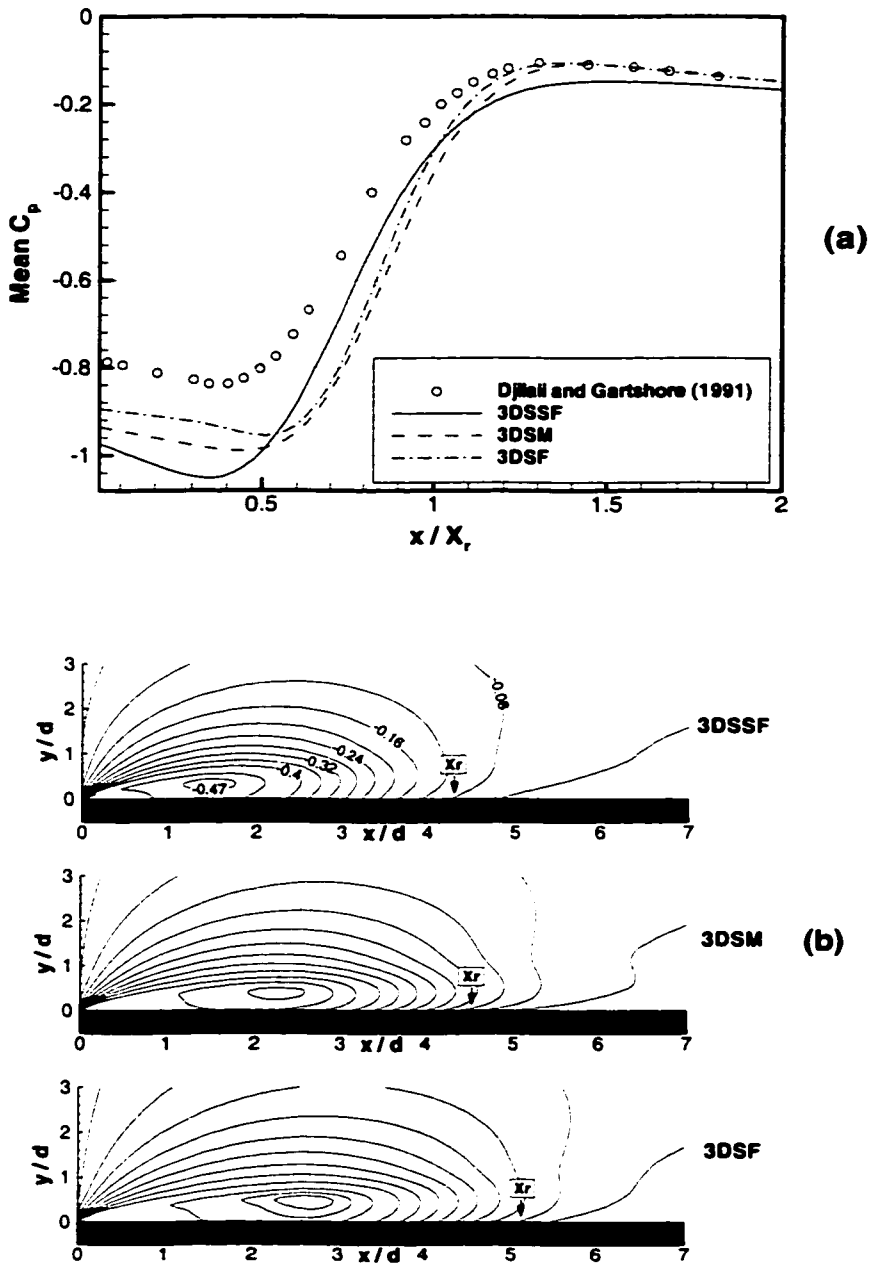

Figure 5.17: (a) Mean surface pressure coefficient distributions; (b) Mean pressure contour for three simulations

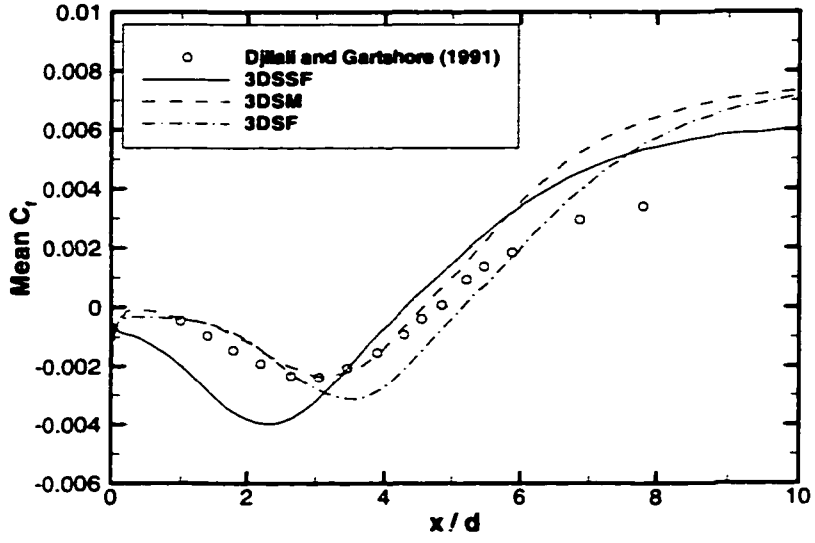

Figure 5.18: Mean wall shear stress coefficient distributions

and measured wall shear stress distributions. Again the experimental trends are well reproduced and the maxima and minima compare well within the large uncertainty of the measured values (±25%).

Figure 5.19 compares the mean streamwise velocity profiles at several stations along the plate with pulsed-wire measurements [12]. The 3DSSF profiles are in very good agreement with measurements at all stations, but both 3DSF and 3DSM predict a broader backflow profile and underestimate the peak backflow velocity over the first half of the separation bubble. Further downstream, all three simulations result in similar profiles. In the recovery region, the present LES simulations do not suffer from the commonly observed velocity defect obtained with RANS computations [16]. The dynamics of the flow in this region is largely governed by the large scale unsteadiness, a process that is well captured by LES but poorly modelled in RANS-based calculations.

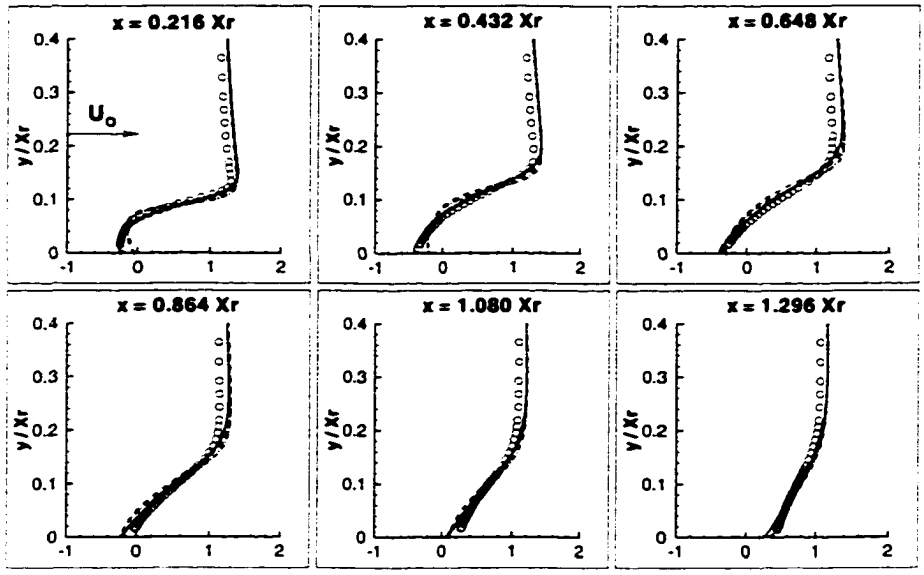

Figure 5.19: Mean streamwise velocity (U/U_o) profiles at selected locations: Experimental [12], circle; 3DSSF, solid line; 3DSM, dashed line; 3DSF, dot-dashed line

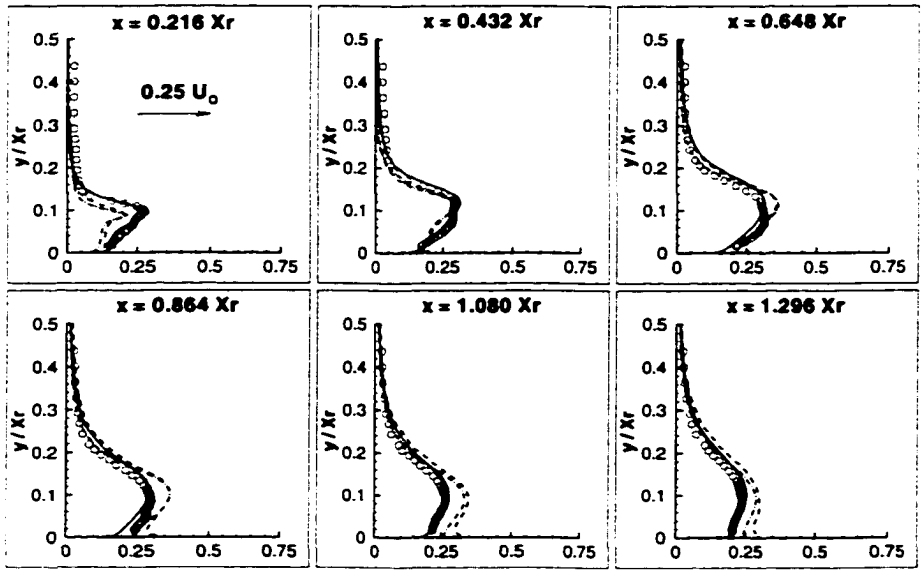

Figure 5.20: Mean streamwise turbulent intensity ($< u' > /U_o$) profiles: Experimental [12], circle; 3DSSF, solid line; 3DSM, dashed line; 3DSF, dot-dashed line

The mean turbulent intensity profiles, including both resolved and SGS contributions, are presented in Figure 5.20. The 3DSSF simulation yields remarkably good agreement with experimental data throughout. The cusp near the leading edge is well reproduced, the correct evolution of the maximum intensities with streamwise direction is obtained and a maximum value of $< u' > /U_o \approx 0.3$ is attained in the last third of the mean separation bubble. The 3DSF and 3DSM profiles, on the other hand, have noticeable deficiencies. The intensities are underestimated for $x/\overline{X}_r < 0.4$, and are overestimated for $x/\overline{X}_r > 0.5$. In 3DSM, where wall damping is used, a near-wall peak is present after $x/\overline{X}_r > 0.6$. Available measurements do not resolve the near-wall region, but the appearance of a near-wall peak in the recovery region, $x/\overline{X}_r > 1.2$, is not unrealistic; such a feature was reported in the highly resolved DNS of the low Reynolds number flow over a backward facing step of [92]. The Reynolds shear stress profiles, $-< u'v' >$, in Figure 5.21 show that the 3DSSF simulation produces higher Reynolds shear stress close to the leading edge. 3DSF and 3DSM achieve the same level around $x/\overline{X}_r = 0.5$, but as in the case of the turbulent intensity, attain higher values afterward.

The contribution of the SGS to the mean turbulent intensity ($< u' > /U_o$) and the mean turbulent shear stress ($-< u'v' > /U_o^2$) is shown in Figure 5.22 at selected locations for the 3DSSF case. The contribution is generally largest close to the separation point where the rapid break-up of the two-dimensional structures occurs right after the leading edge. While $< u' > /U_o$ in Figure 5.22a is quite well resolved, the SGS contribution to $-< u'v' > /U_o^2$ component in Figure 5.22b is significantly larger, especially close to the separation. In 3DSF, the contribution of the model to both components is similar to the 3DSSF, whereas in the Smagorinsky model (3DSM), the SGS contribution is minimal. The dissipation provided by this model is, in the mean,

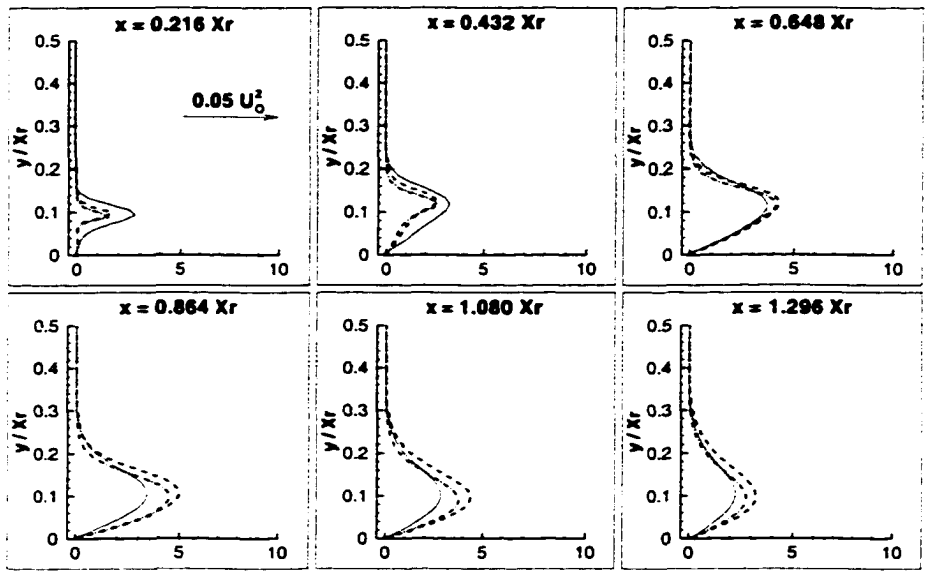

Figure 5.21: Mean turbulent shear stress ($-< u'v' > /U_o^2$) profiles: 3DSSF, solid line; 3DSM, dashed line; 3DSF, dot-dashed line

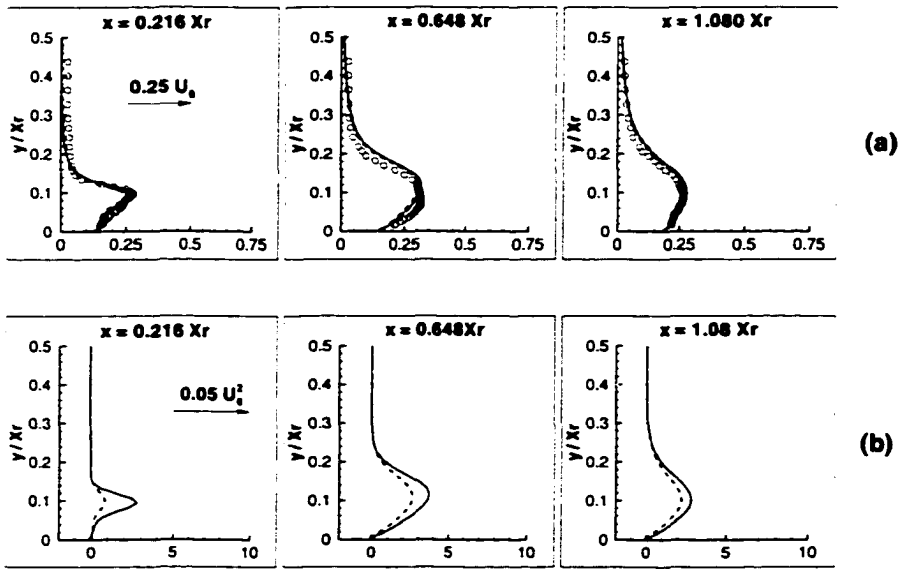

Figure 5.22: Contribution of the SGS to (a) the mean turbulent intensity profiles, (b) the mean turbulent shear stress profiles in 3DSSF: Experimental [12], circle; Total, solid line; Resolved, dashed line

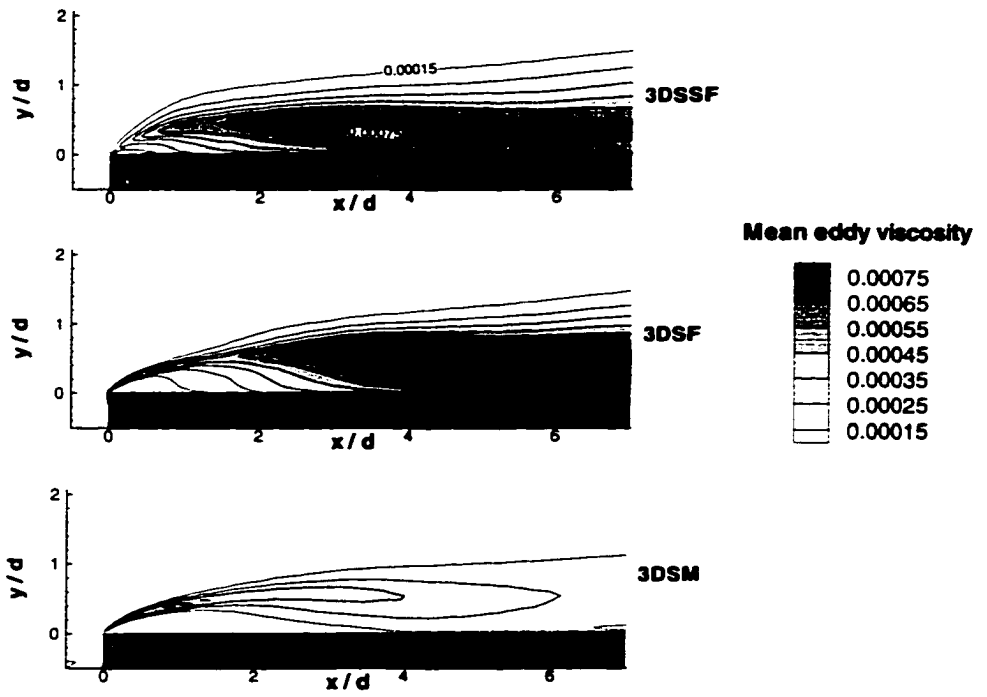

Figure 5.23: Mean eddy viscosity for three SGS simulations

very small and confined to the early part of the separated shear layer. It should be noted that the constant (C_s) used here is that recommended by Kogaki [51] for separated rectangular cylinder flows and is lower than the "standard" value used in boundary layer simulations. Figure 5.23 presents the mean eddy viscosity for each simulation. Both structure function models (3DSSF and 3DSF) produce larger SGS dissipation in the reattachment zone, but much higher levels are obtained with 3DSF which is therefore expected to have a much stronger influence on the dynamics of the flow in the reattachment zone.

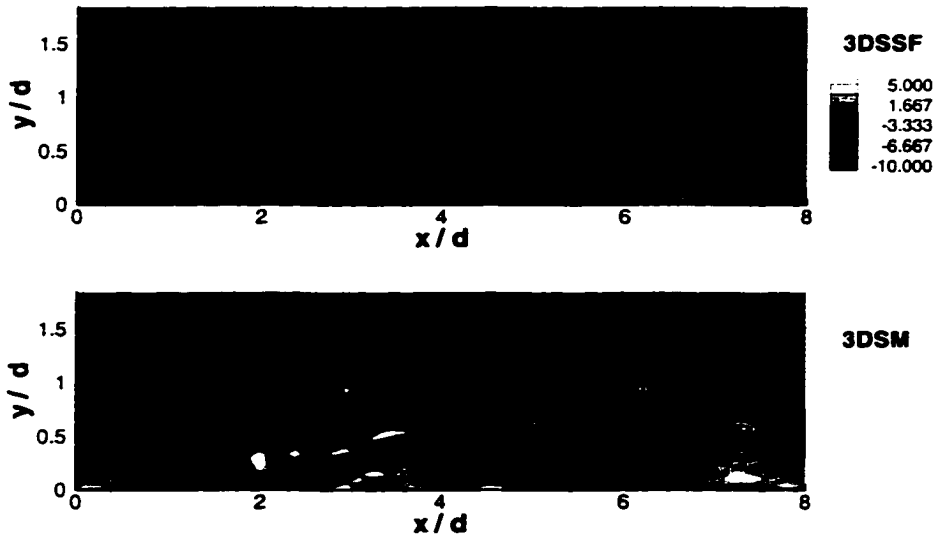

Figure 5.24: Instantaneous spanwise vorticity contours in $x-y$ plane at $z/d = 2.6$: 10 contours from -10U_o/d to 5U_o/d

5.6.2 Flow Structures and Dynamics

Instantaneous spanwise vorticity fields from the selective structure function (3DSSF) and the Smagorinsky model (3DSM) simulations are shown in Figure 5.24. In the case of 3DSM, no significant fluctuations are detected in the separated shear layer before $x/d \approx 1.8$, whereas instabilities appear much sooner in 3DSSF. The streamwise evolution of the instabilities is illustrated at various $y-z$ planes in Figure 5.25 showing the earlier appearance of transverse perturbations and three-dimensionalization in 3DSSF. The small scale structures are much more prominent in the reattachment region for 3DSM. This is consistent with the higher turbulent intensities obtained with this model in the reattachment and recovery regions, in Figure 5.20, and the much lower SGS dissipation of the model.

Figure 5.26 shows the instantaneous streamwise vorticity field in a plane close to

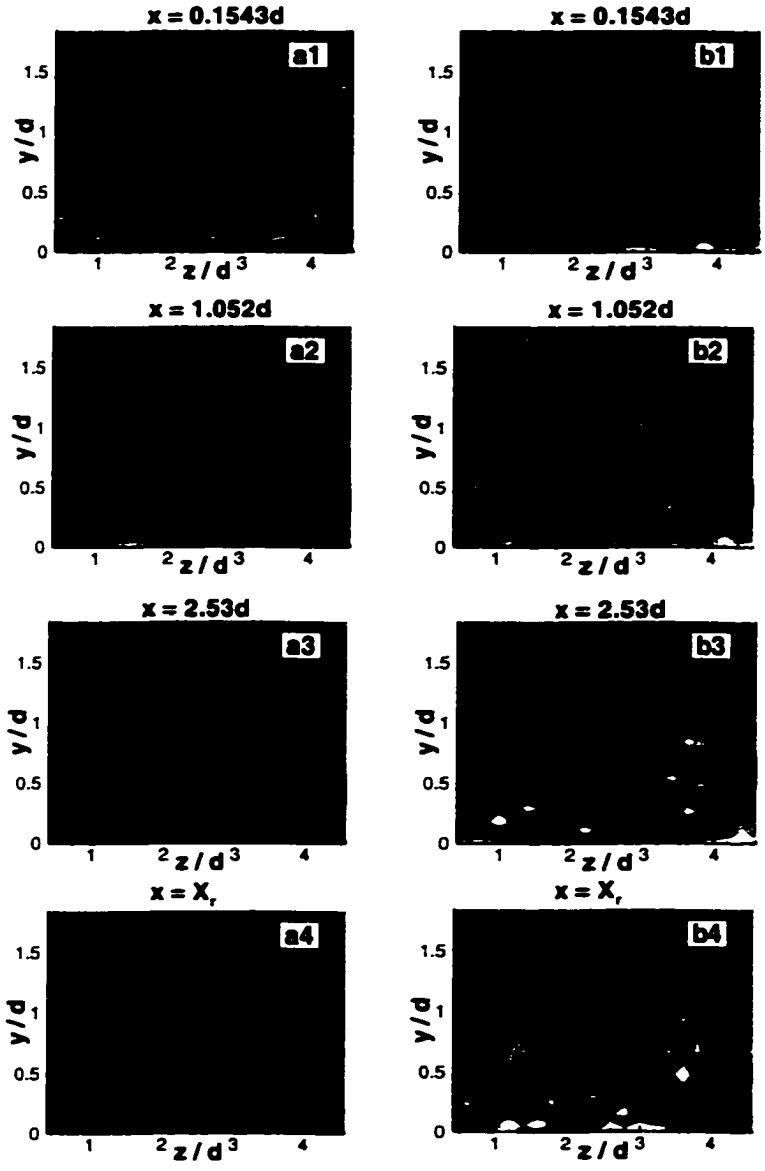

Figure 5.25: Instantaneous spanwise vorticity contours in $y - z$ plane, 10 contours from -10U_o/d to 5U_o/d: **a1, a2, a3 and a4** for 3DSSF; **b1, b2, b3 and b4** for 3DSM

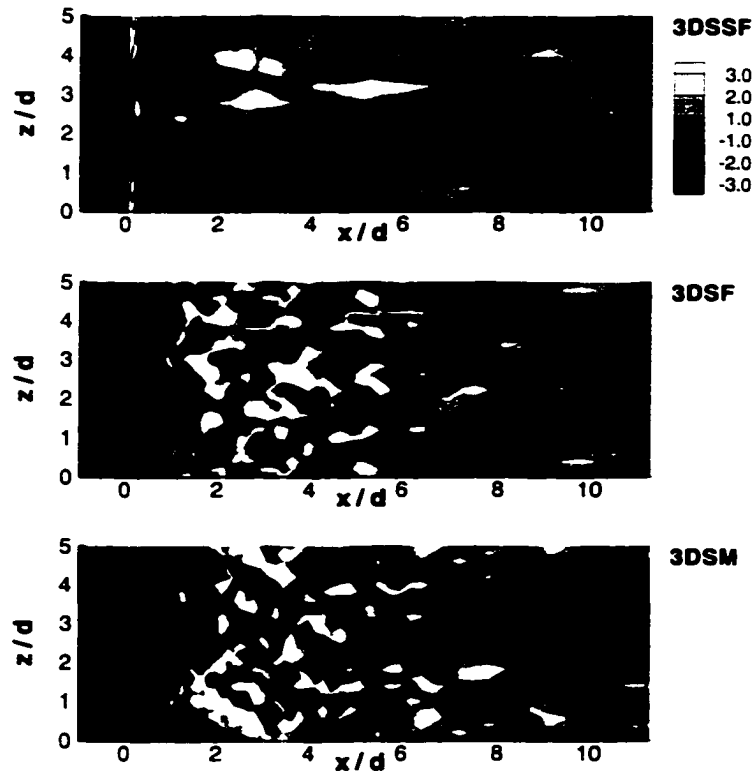

Figure 5.26: Instantaneous streamwise vorticity contours in $x-z$ plane at $y/d = 0.12$: 7 contours from -$3U_o/d$ to $3U_o/d$

the surface of the plate. 3DSM and 3DSF exhibit less "coherence" and contain smaller structures with roughly equal characteristic sizes in the spanwise and streamwise directions. The structures become gradually more elongated only after reattachment. 3DSSF presents a much higher degree of coherence and the structures with streamwise lengths in the range of 1-3d are apparent. Significant streamwise vorticity levels are not observed until well downstream of separation with the appearance of counter-rotating pairs of vortices.

Overall, the selective structure function simulation (3DSSF) produces separated shear layer instabilities, dynamical patterns, and structures which are physically con-

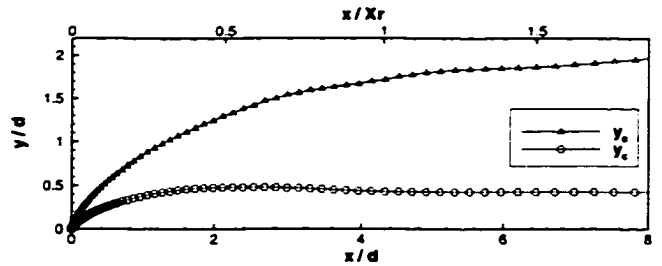

Figure 5.27: The center (y_c) and the edge (y_e) of the mean separated shear layer: 3DSSF

sistent with the flow visualization of Saathoff and Melbourne [7]. It was also shown that the mean flow characteristics are overall better with this model. Further analysis is therefore confined to the 3DSSF simulation.

The loci of the shear center (y_c), where the r.m.s. velocity attains a maximum, and the edge of the shear layer (y_e), where the r.m.s. velocity attains 2.5% of $< u' > /U_o$, are shown in Figure 5.27 for the 3DSSF. The position of y_c attains a maximum around $x/d = 2$ and then slightly declines and becomes constant around the mean reattachment point. The result compares very well with [12]. The prediction of y_e is slightly higher than the experimental value due to the higher uncertainty in locating y_e.

The instantaneous velocity fields along the surface defined by the mean shear center (y_c) are shown in Figure 5.28. The structures that are identifiable in the velocity fields close to the separation point, are stretched in the spanwise direction as clearly shown in the vertical velocity (V) field. In the reattachment region, larger structures are identified. The small scale structures are suppressed by the dissipative effect of the SGS models. The instantaneous vorticity field corresponding to Figure 5.28 is plotted in Figure 5.29. In this figure, the structures close to separation are

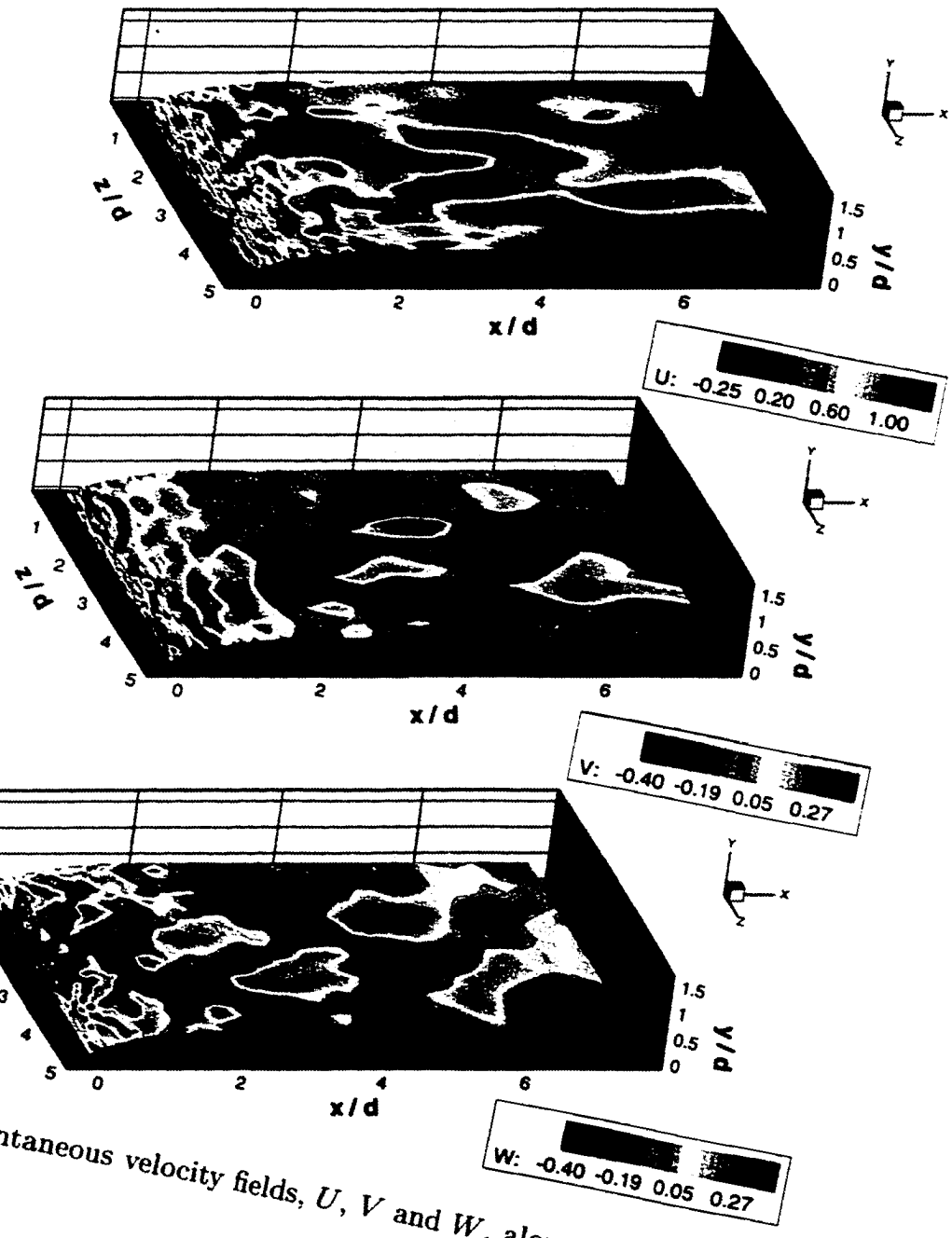

Figure 5.28: Instantaneous velocity fields, U, V and W, along the shear center location: 3DSSF

hardly discernible, however, three horseshoe vortices are visible in the reattachment region.

In order to identify the flow structures more clearly, the technique of Jeong and Hussain [94] was used. In this method, the vortex cores are extracted directly from the instantaneous velocity fields. The vortex cores are identified with a region of negative λ_2, the second largest eigenvalue of the tensor $S_{ik}S_{kj} + \Omega_{ik}\Omega_{kj}$, where $S_{ij} = (U_{i,j} + U_{j,i})/2$ and $\Omega_{ij} = (U_{i,j} - U_{j,i})/2$ are the symmetric and antisymmetric parts of the velocity gradient tensor, $U_{i,j} = \partial U_i/\partial x_j$. This method has been successful in capturing vortical structures, even in the presence of strong shear occurring in near wall boundary layers [95].

The contour plot of the second largest eigenvalue (λ_2) is plotted in Figure 5.30 for the same instantaneous fields as Figure 5.29. The structures are much more clearly exhibited than in Figure 5.29. In the first half of the mean separation bubble, $x/d \leq 2$, the strong background shear along the separated shear layer is eliminated and only vortex cores remain. These structures develop at the leading edge of the plate and are largely two-dimensional in nature. Further downstream, in the reattachment region, three-dimensionalization has occurred and the predominant structures are clearly identified as hairpin (horseshoe) vortices. These structures are identical to the sketch suggested by Kiya and Sasaki [14] based on the interpretation of conditionally sampled data.

The spanwise length scale of the horseshoe vortices in the reattachment region range from $1.5d$ to $2.75d$ (0.35-0.58$\overline{X}_r$), which is in the range suggested in [7, 14]. The legs of the horseshoe vortices are inclined with respect to the streamwise direction. These vortices can be also identified by region of positive and negative spanwise

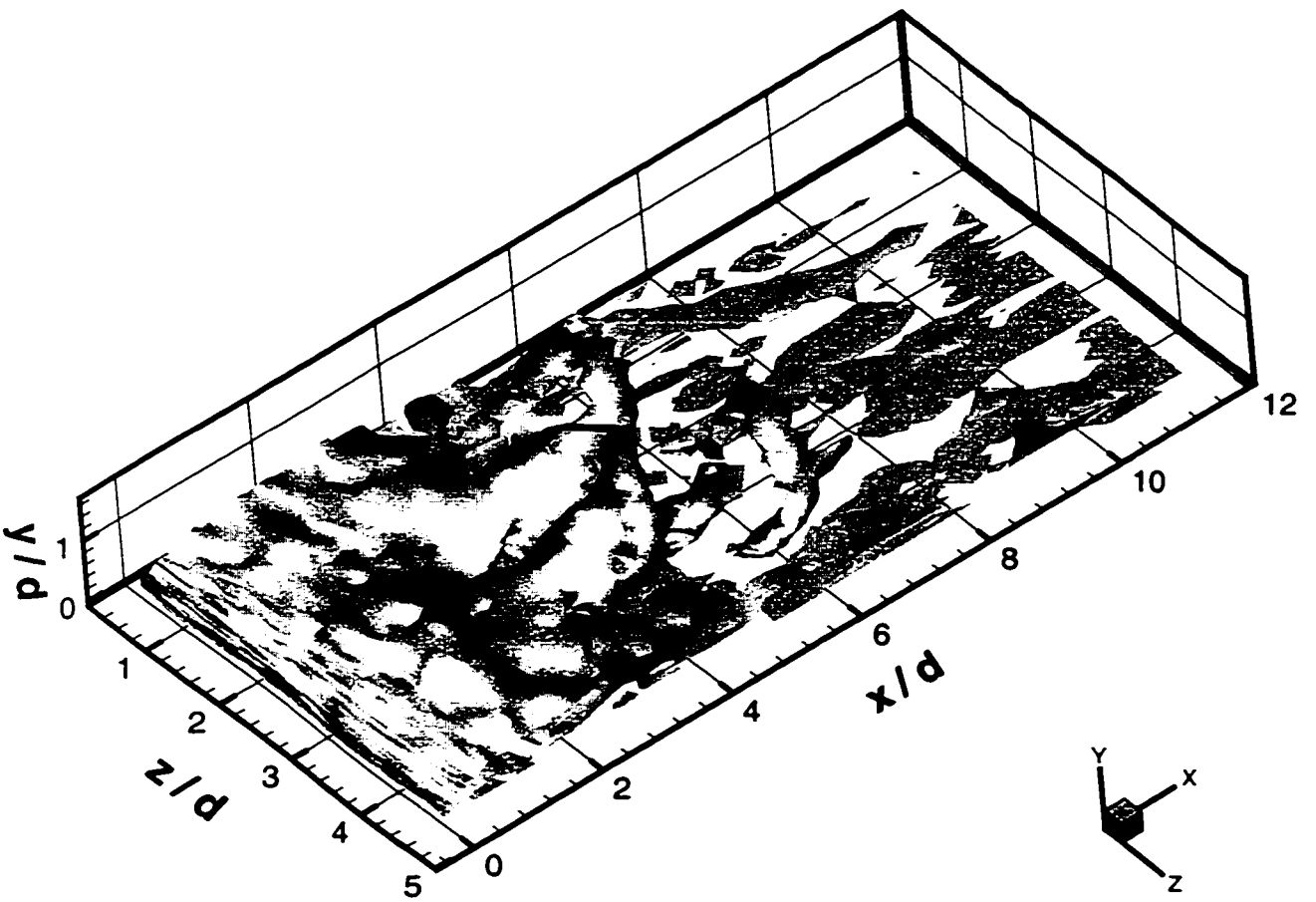

Figure 5.29: Instantaneous vorticity contour: 3DSSF, $|\omega| = 2.5U_o/d$

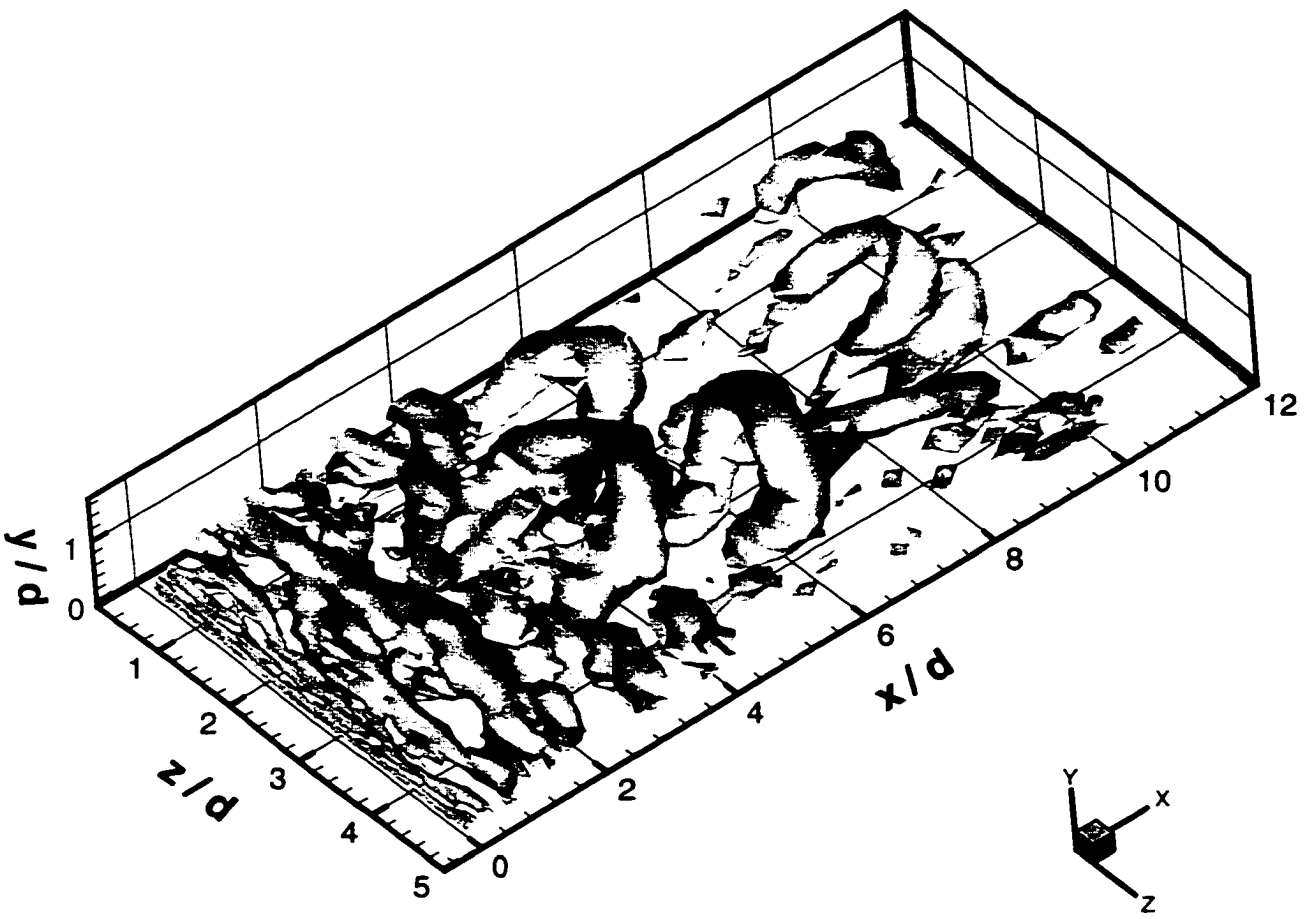

Figure 5.30: Instantaneous contour plot of the second largest eigenvalues: 3DSSF, λ_2 = -0.1

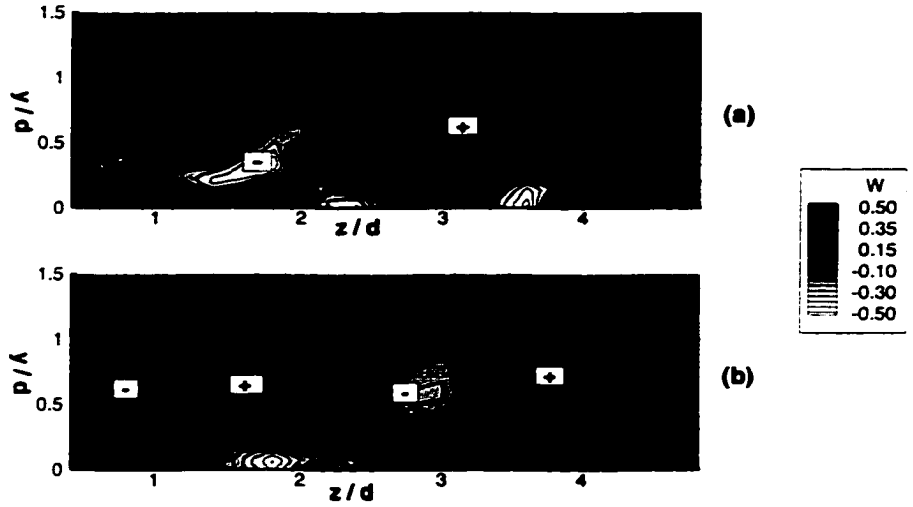

Figure 5.31: Spanwise velocity contour from 3DSSF in the $y-z$ plane: (a) $x/d = 3.44$; (b) $x/d = 5.75$

velocity (W) as shown in the $y-z$ plane in Figure 5.31.

A typical vortex grows in every direction as it travels downstream of the reattachment region. Due to the interaction between the vortical motion of the large scale structure and the wall, it also tends to lift away from the wall. This in turn, brings the top end of the horseshoe vortex into contact with the outer (higher velocity) region, resulting in further stretching and inclination of the vortex along the flow direction. Eventually, the central portion breaks down, and only the two inclined legs remain. This phenomenon happens in the recovery region. The unsteady motion from the shedding of these large scale vortices creates the oscillation of the instantaneous reattachment point. Three time frames of instantaneous reattachment points are shown in Figure 5.32. The dark colour indicates a negative wall shear stress, while the light colour indicates a positive wall shear stress. The oscillation of the instantaneous reattachment point is controlled indirectly by the flapping motion

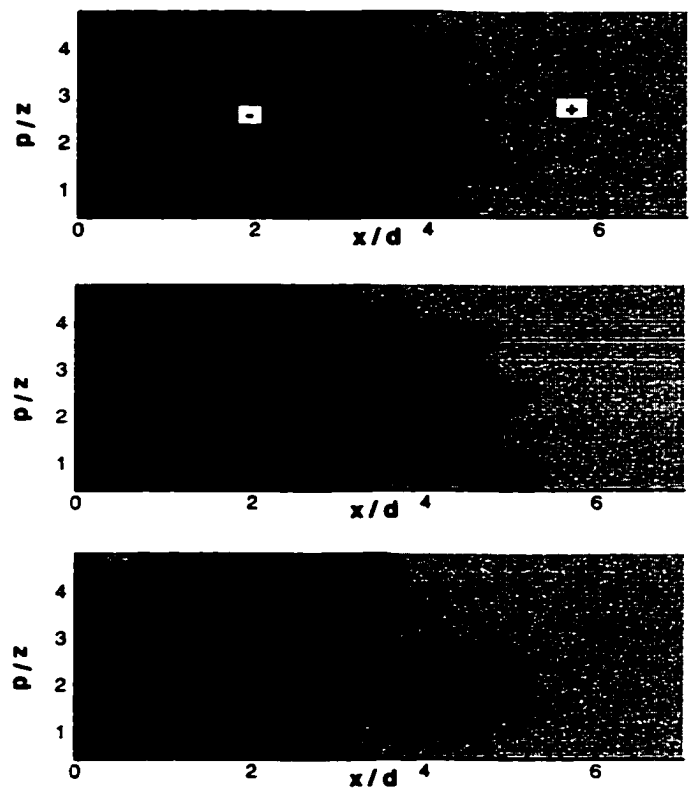

Figure 5.32: Time frames indicating the motion of line of zero wall shear stress in the $x - z$ plane: 3DSSF

of the shear layer, or low-frequency unsteadiness [14] which is not clearly understood and difficult to identify.

Figure 5.33a shows the trace of the instantaneous vertical velocity recorded just downstream of separation within the shear layer. The power density spectrum of this signal is shown in Figure 5.33b. Consistent with experimental spectra [12], high frequency motion is dominant in the vicinity of separation, and the spectrum indicates small eddies with time scales of order of $0.3tU_o/d$. In addition to the high frequency activity centered around $fd/U_o = 0.8$, the signal also exhibits peaks in the low fre-

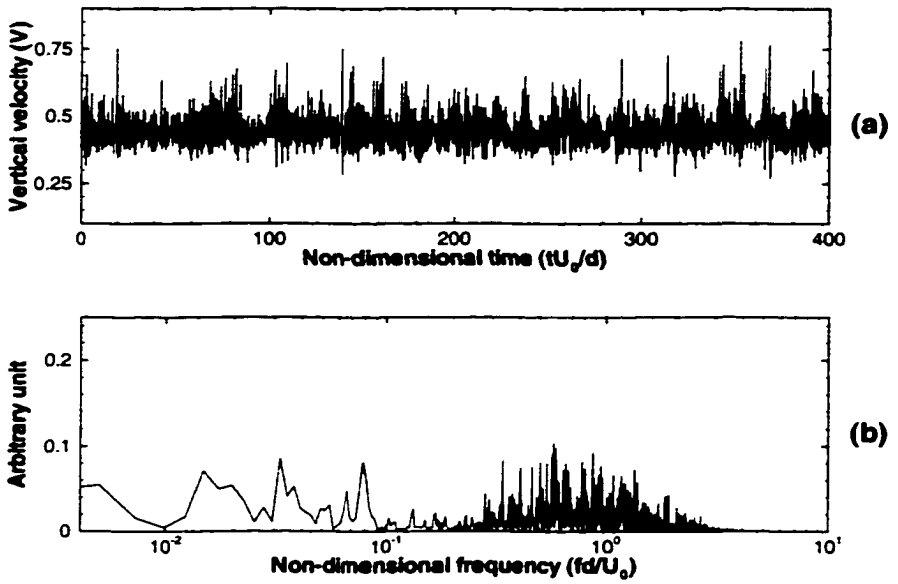

Figure 5.33: 3DSSF simulation (a) vertical velocity (V) signal at $x/d = 0.493$, $y/d = 0.47$, mid-span; (b) power spectrum density

quency range ($fd/U_o \approx$ 0.02-0.08). As mentioned earlier, this low frequency motion is attributed with the flapping of the shear layer.

To provide further insight into the flow dynamics around the reattachment region, Figure 5.34 shows the streamwise velocity signal at a location close to the mean reattachment and the corresponding (Fourier) power spectrum density. Compared to the signal sampled near separation (Figure 5.33), there is little energy in the high frequencies. Most of the energy is in the larger scales corresponding to non-dimensional frequencies (fd/U_o) well below 0.2.

A time domain analysis using the wavelet transform of the near-wall streamwise velocity signal was conducted in this region. Figure 5.35 shows the wavelet map of this signal, in terms of the relief plot of the absolute value of the wavelet coefficient.

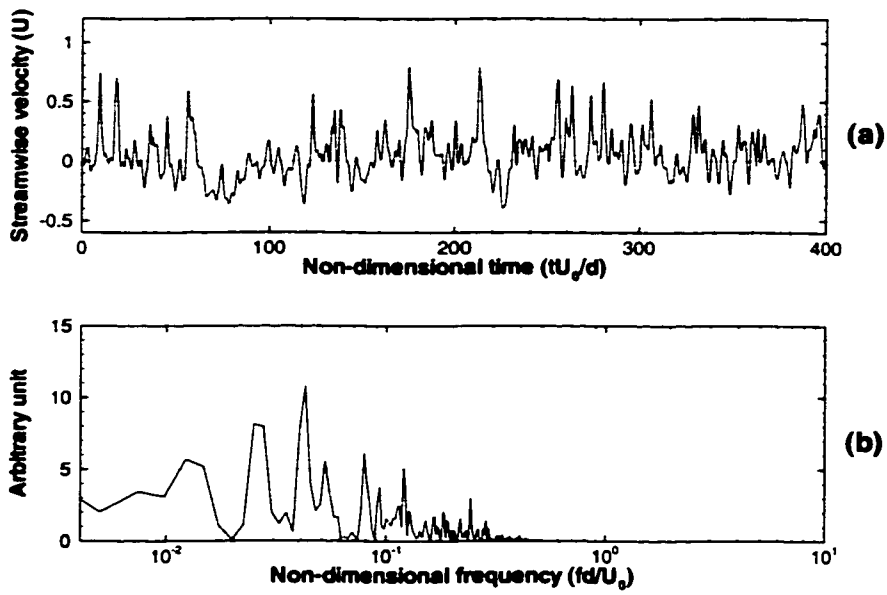

Figure 5.34: 3DSSF simulation (a) near-wall streamwise velocity (U) signal at $x/d =$ 4.51, mid-span; (b) power spectrum density

The intermittent nature of the large scale unsteadiness is illustrated along the most distinct range of scales: $tU_o/d \approx$ 20-50. This range corresponds to non-dimensional frequencies of 0.02-0.05 and is associated with the low frequency flapping of the shear layer discussed earlier. The intermittence of this phenomenon is clearly shown by the alternating peaks and troughs between 45 and 395 time units. The scales containing the most energy are in the range of 5-15tU_o/d, or non-dimensional frequencies of 0.066-0.2. This coincides with the range of frequencies reported experimentally for the pseudo-periodic vortex shedding around reattachment [9, 12]. The time localization of these events shows activity of relatively short duration, followed by longer quiescent periods. Furthermore, the signal in Figure 5.34a shows positive fluctuations about the mean which are of a much higher amplitude than the negative fluctuations.

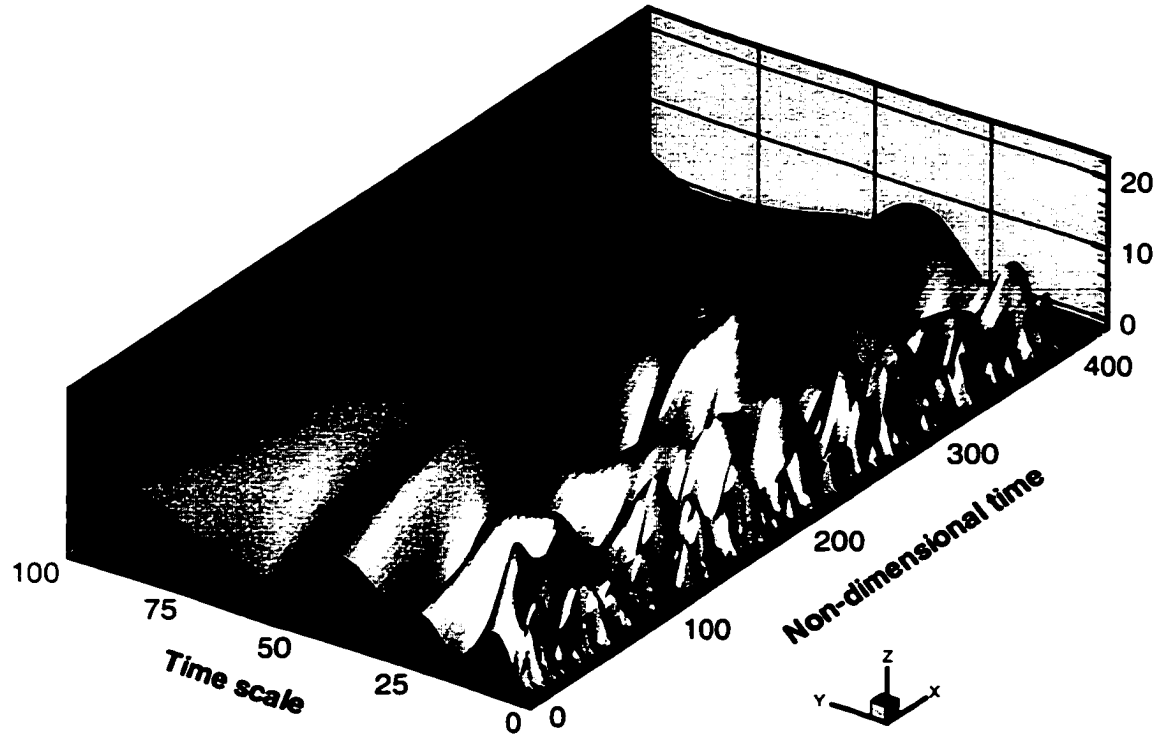

Figure 5.35: Morlet wavelet map of near-wall streamwise velocity (U) signal at x/d = 4.51, mid-span: 3DSSF

This feature and the patterns shown in the wavelet map suggest that a typical cycle consists of two distinct phases: (i) gradual growth of large scale structures in the separated shear layer, accompanied by a progressive growth of the separation bubble; (ii) shedding of a large scale structure followed by a "collapse" of the bubble and abrupt shortening of the reattachment length.

5.7 Closing Remarks

The results in this chapter indicate that three-dimensional simulations provide more realistic simulations of the unsteady separated flow than two-dimensional cases. Three-dimensionality induces the break-up of the two-dimensional structure into smaller three-dimensional structures and results in more complex transition, turbulent and mixing processes.

At moderate Reynolds number (Re_d = 1,000), an exceptionally long integration time is required to establish a statistically stationary flow. Overall, the mean flow statistics follows the same trend as high Reynolds number experimental results. The selective structure function subgrid scale model slightly alters the dynamics of the flow and results in mean flow statistics which are in better agreement with experimental observations. The flow structures are clearly identified at the initial transient period and characterized by a Kelvin-Hemholtz type instability. Rapid amplification of three-dimensional disturbances leads to the break-up of two-dimensional structures which begins around the middle of the mean separation bubble. The three-dimensional transitional simulations provide insights into the dynamics of the flow and the turbulent transport processes, however, to be more directly relevant to a number of engineering applications, simulations must be extended to higher Reynolds number.

At Re_d = 50,000, the flow structures break up and become turbulent right after the separation. The selective structure function simulation predicts the mean flow and turbulence characteristics which are in excellent agreement with the pulsed-wire experimental data [12] and produces the separated shear layer instabilities, dynamical patterns which are physically consistent with the flow visualization of Saathoff and Melbourne [7]. The horseshoe vortices are identified in the reattachment region.

This structure is more clearly identifled with the λ_2 technique than with the typical $|\omega|$ technique, and identical to the sketch suggested by Kiya and Sasaki [14]. With Fourier and wavelet transforms analysis, the characteristic frequencies and intermittent nature of the pseudo-periodic vortex shedding from the separated shear layer and the reattachment region as well as the shear layer flapping were captured in three-dimensional simulations.

Chapter 6

CONVECTIVE HEAT TRANSFER IN BLUFF PLATE GEOMETRY

6.1 Introduction

The bluff plate is a basic module encountered in a number of heat transfer applications, particularly heat exchangers. In this chapter, two and three-dimensional simulations of convective heat transfer over a bluff rectangular plate are presented at low and moderate Reynolds number, ($150 \leq Re_d \leq 1{,}000$). The fluid dynamical features were investigated and discussed in Chapters 4 and 5. In this chapter, the influence on the temperature field of flow features such as large scale structures and three-dimensionality is investigated. The focus is primarily on the behavior of the wall heat transfer coefficient, expressed in term of the Nusselt number (Nu_x). This

chapter is organized as follows, first, a brief outline of the computational methods and boundary conditions is provided. This is followed by a discussion of the results from the two-dimensional steady and unsteady simulations, and finally of the three-dimensional unsteady simulations.

6.1.1 Computational Methods and Boundary Conditions

In the present heat transfer calculations, it is assumed that transport is by forced convection only and that temperature variations are small enough for the fluid properties to be considered constant. The temperature is hence a passive scalar and the momentum equation is decoupled from the energy equation. Accordingly, the convective heat transfer simulations are performed by explicitly solving the time-dependent energy equation for an incompressible fluid, after the solution of the flow field has been obtained at a given time step.

The boundary conditions for the energy equation are:

- Inlet(West): Uniform temperature distribution; ($T = T_o$).
- Outlet(East): Advective boundary condition; ($\frac{\partial T}{\partial t} + C_u \frac{\partial T}{\partial x} = 0$).
- North and South: Symmetry condition ($\frac{\partial T}{\partial y} = 0$).
- Top and Bottom (3-D simulations): Periodic condition.
- Surface of bluff plate: Constant heat flux ($\dot{q}$).

The convective heat transfer calculations are performed at Reynolds number ranging from 150 to 1,000 for four Prandtl numbers (Pr) and for blockage ratios (Br) varying between 5.6% to 33%. A summary of the computations is provided in Table

Simulations	$Br(\%)$	Re_d	Pr
2-D steady	10, 15, 20, 33	150, 250, 300, 400	0.7, 1, 2, 5
2-D unsteady	10, 15, 20	1,000	0.7, 1, 2, 5
2-D and 3-D unsteady	5.6	1,000	0.7

Table 6.1: Summary of the parameters in convective heat transfer calculations

6.1. The influence of the large scale dynamics and of three-dimensionality on the temperature field are documented and discussed for the blockage ratio case $Br = 5.6\%$. The three-dimensional simulations are performed both in DNS and LES modes. The selective structure function subgrid scale model was used in the 3-D(LES), since the localization obtained with this model was shown in Chapter 5 to yield simulations that are consistent with experimental observations. The turbulent Prandtl number (Pr_t) was assumed to be constant and taken to be equal to 1 [68]. Other computational parameters such as computational domain, time step etc., are the same as those presented in previous chapters.

6.2 Two-Dimensional Simulations

6.2.1 Steady Laminar Flows

This case has been investigated in detail in Ref. [3] and is briefly considered here as a basic validation. The predicted heat transfer rate along the plate surface, expressed

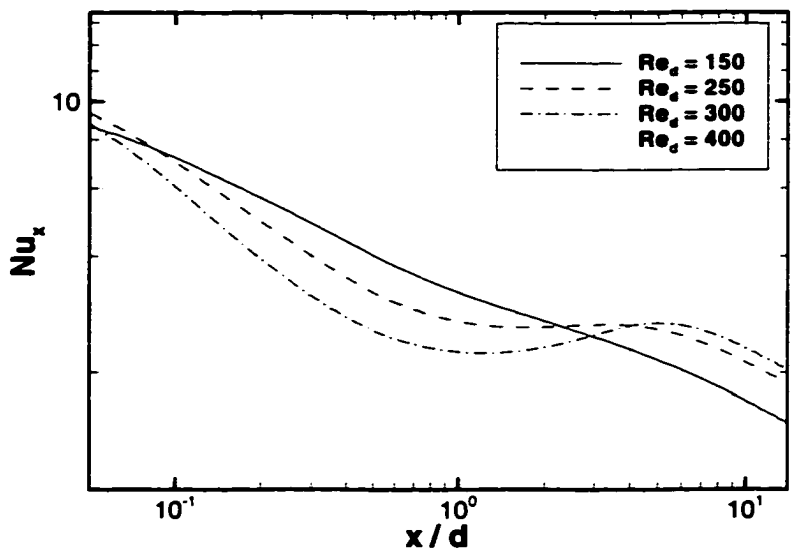

Figure 6.1: Effect of Reynolds number on the Nusselt number distribution: Br = 10% and $Pr = 0.7$

in terms of the Nusselt number, $Nu_x = h_x d/k$, where $h_x = \dot{q}/(T_o - T_w)$, is plotted in Figure 6.1 and 6.2. In the present investigation, the specified heat flux ($\dot{q}$) along the plate is kept constant, therefore, the higher the wall temperature (T_w), the lower the heat transfer rate. For a low Reynolds number there is no flow separation, and a linear (log-log) distribution is obtained consistent with developing laminar flow in a channel [96]. As the Reynolds number increases, a separation bubble forms, and the Nusselt number distribution becomes non-linear. A local maximum occurs slightly downstream of the reattachment point and become more pronounced as Reynolds number increases.

The effect of blockage ratio on the heat transfer rate is shown in Figure 6.2a. As expected, the blockage ratio has a strong influence on both the separation bubble size and the heat transfer rate: a high blockage ratio decreases the separation bubble

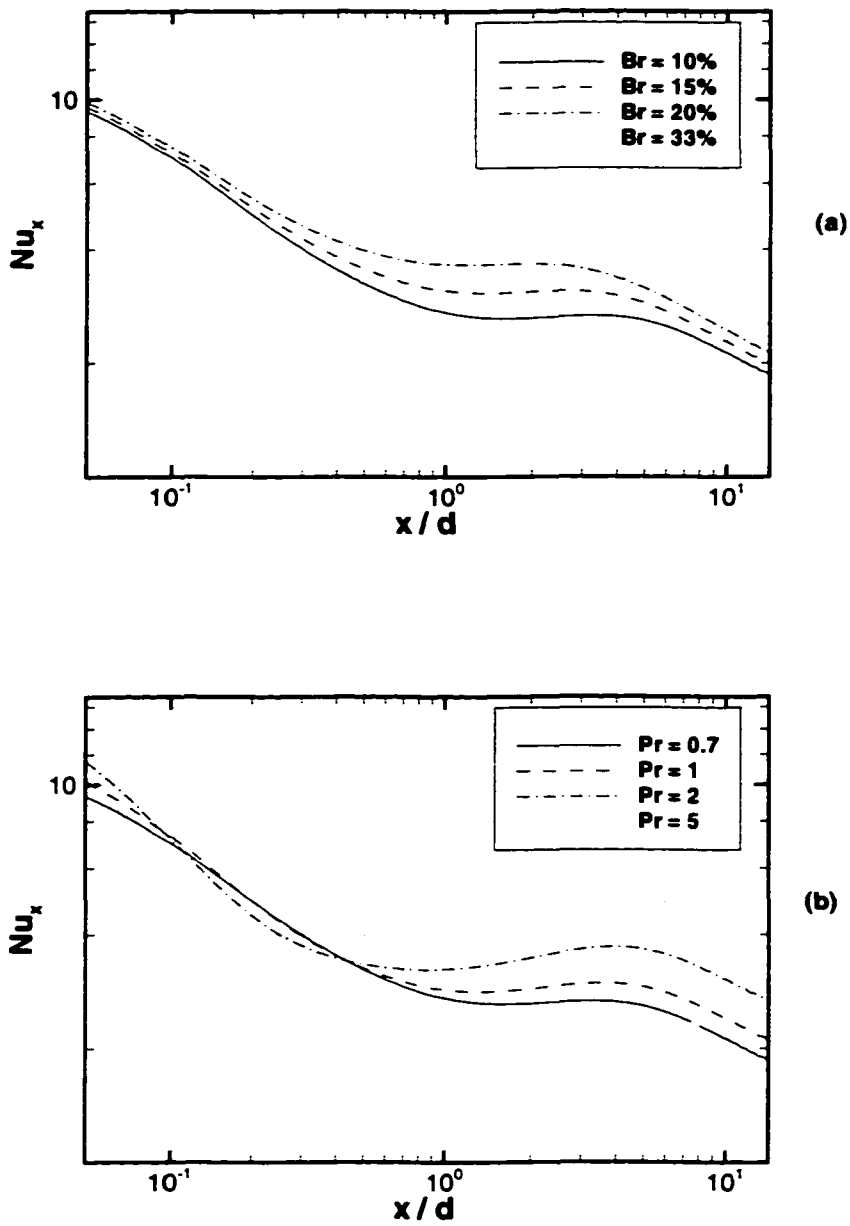

Figure 6.2: (a) Effect of blockage ratio on the Nusselt number distribution, Re_d= 250 and $Pr = 0.7$; (b) Effect of Prandtl number on the Nusselt number distribution, Re_d = 250 and $Br = 10\%$

size and increases the heat transfer rate. Figure 6.2b shows the effect of the Prandtl number on the heat transfer rate. The location of the Nusselt number maximum along the streamwise direction does not vary with the Prandtl number, but it increases with increasing Prandtl number. The overall pattern of the present steady laminar flow results are in excellent agreement with [3].

6.2.2 Unsteady Transitional Flows: $Re_d = 1{,}000$

In Section 4.4, it was shown that the flow at this Reynolds number becomes unsteady and is characterized by the appearance of shear layer instabilities near separation, transition to turbulence prior to reattachment, and the pairing and shedding of large scale vortices. The temperature field was reported to strongly correlate with such large scale vortices [22]. Figure 6.3 presents the spanwise vorticity, temperature field and the streamwise variation of Nusselt number at one instant. The instantaneous Nusselt number distribution attains a local peak slightly upstream of the vortex located at $x/d \simeq 4$. The induced rotational motion transports heated fluid away from the surface and entrains ambient fluid towards the surface. The temperature field in Figure 6.3 is an excellent tracer of large scale vortices in the transport of energy.

Figure 6.4a shows the effect of Prandtl number on the mean Nusselt number distribution. As in the case of steady flow, the maximum value attained by the mean Nusselt number increases with the Prandtl number, but as will be shown later, this maximum occurs slightly upstream of the time mean reattachment point. Figure 6.4b shows the decreasing and shifting of the local maxima downstream of the leading edge for the case of $Br = 10$, 15 and 20%. In contrast to steady flow results, increasing the blockage ratio increases the separation bubble size and lowers the maximum heat

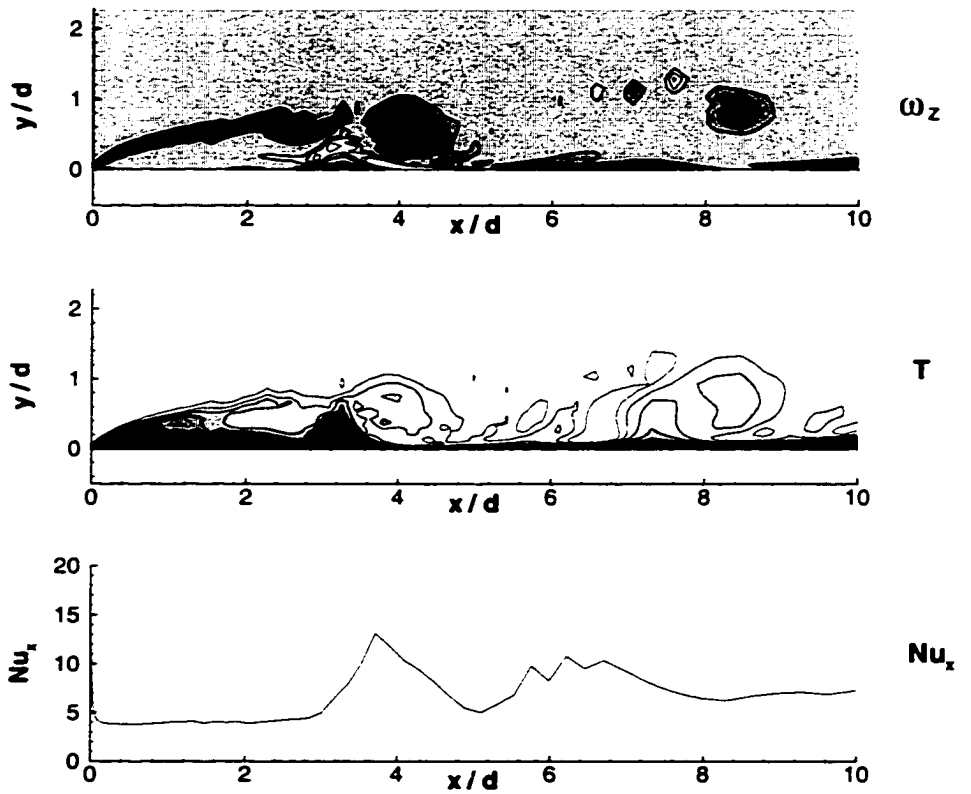

Figure 6.3: Instantaneous predicted spanwise vorticity, temperature and Nusselt number distribution: 2-D(DNS); dark regions indicate high vorticity and high temperature

transfer rate. This is due to the high blockage effect which stabilizes the flow and delays the onset of instability. The stabilizing effect of increased blockage ratio is clearly illustrated in Figure 6.5 by the instantaneous spanwise vorticity plots for Br = 33% and 15%. At Br = 33%, the flow becomes steady with a shorter separation bubble and a significantly lower maximum heat transfer rate.

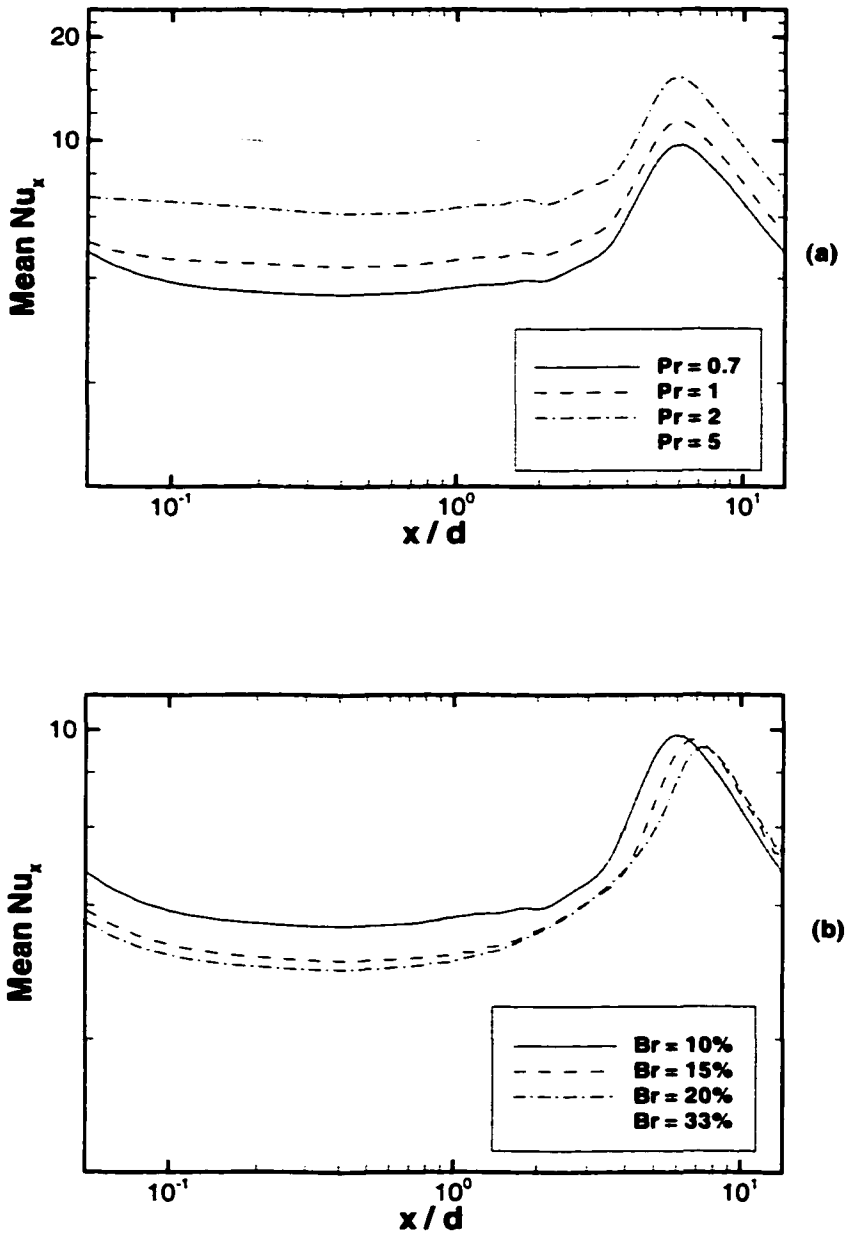

Figure 6.4: (a) Effect of Prandtl number on the mean Nusselt number distribution, $Br = 10\%$; (b) Effect of blockage ratio on the mean Nusselt number distribution, $Pr = 0.7$

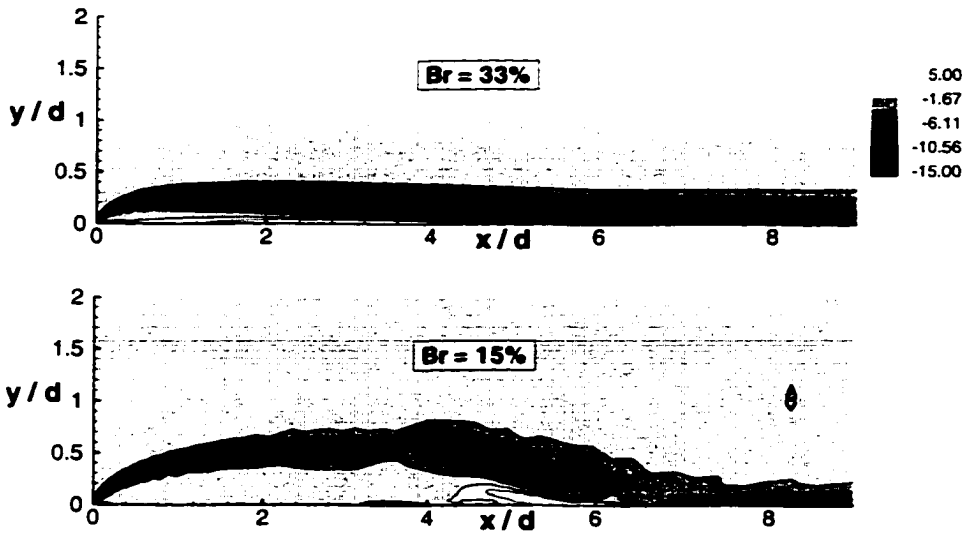

Figure 6.5: Instantaneous spanwise vorticity contour for two blockage ratios at $Pr = 0.7$

6.3 Three-Dimensional Simulations: $Re_d = 1{,}000$

Accounting for three-dimensionality allows for the break-up of the two-dimensional spanwise vorticity which results in more complex transition and mixing processes. The time and spanwise averaged temperature distributions in terms of the dimensionless temperature, θ, where $\theta = (T - T_o)/(T_w - T_o)$ is shown in Figure 6.6 for 3-D(DNS). The profiles exhibit an unusual kink in the separated region, where a large reverse velocity exists, and the sharp deviation seems to correlate well with the center of the separated shear layer (y_c). The shapes of the predicted temperature profiles compare well with experimental results at $Re_d = 5{,}850$, obtained by Ota and Kon [20].

The mean Nusselt number distributions predicted by each simulation are shown in Figure 6.7. In the first half of the mean separation bubble, which is a region of low heat transfer rate, the two-dimensional simulation predicts a higher Nu_x than the

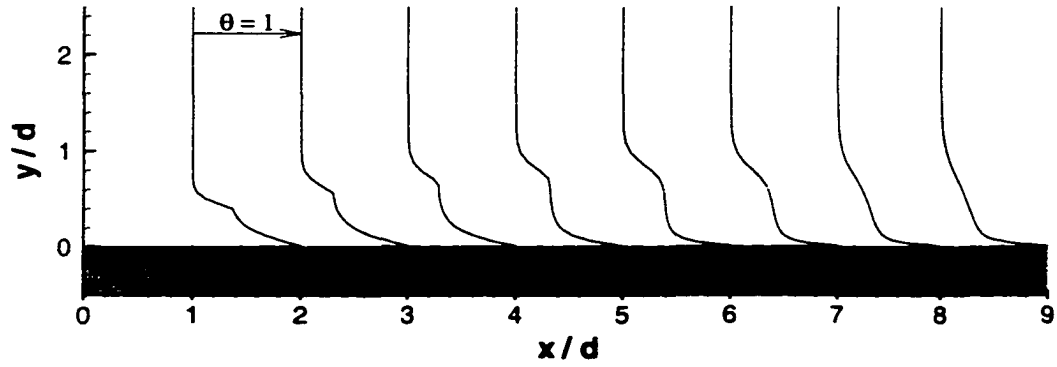

Figure 6.6: The mean temperature profile in term of the dimensionless temperature, $\theta = (T - T_o)/(T_w - T_o)$, 3-D(DNS)

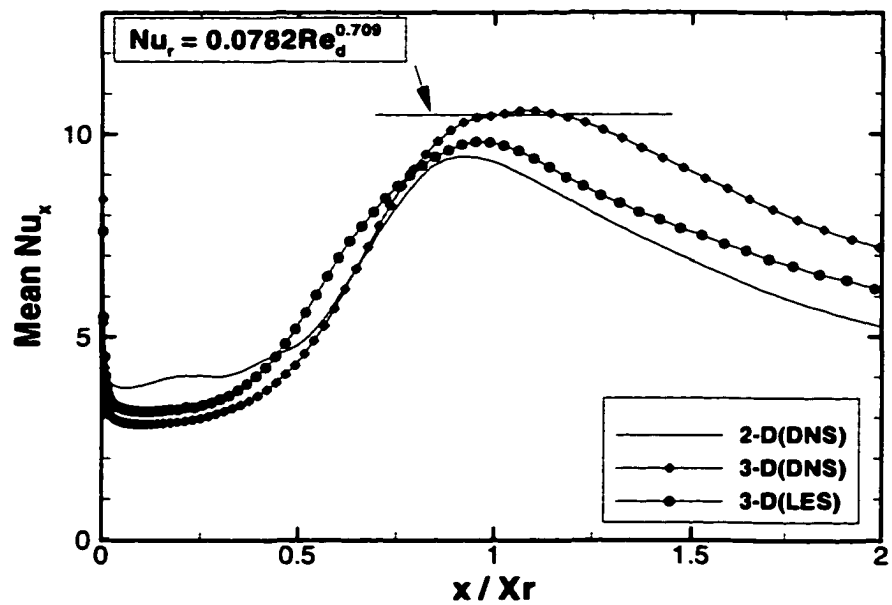

Figure 6.7: The mean Nusselt number distributions along the streamwise direction at $Re_d = 1{,}000$

three-dimensional simulations. This is due to a higher backflow velocity in the three-dimensional case resulting in higher transport of warmer bulk of fluid from the reattachment region. However, in the two-dimensional case, the positive velocity resulted from the unusual secondary separation bubble presented in Figure 4.9 counters it.

After a sharp drop following separation, the mean Nusselt number remains relatively flat for the first half of the bubble and then rises rapidly to a maximum near the mean reattachment point, in general agreement with [20, 22]. The enhancement of the mean heat transfer in this region is a consequence of the shedding and break-up of large scale structures from the separated shear layer (as described in the previous chapter), which begins near the middle of the separation bubble. The break-up process reduces large two-dimensional structures in the separated shear layer to smaller three-dimensional structures and results in more turbulent mixing. The highly three-dimensional and intermittent nature of these small structures increases the transport and exchange of energy between the outer flow and the inner flow. The predicted Nusselt number maxima from the three simulations are within 10% of the empirical correlation deduced by Ota and Kon [20], $Nu_r = 0.0782 Re_d^{0.709}$, where Nu_r is the maximum Nusselt number at the mean reattachment point.

Contrary to the mean flow field, we note that the difference in wall heat transfer coefficients between DNS and LES is significant. This is consistent with the higher turbulent intensities obtained with DNS in the reattachment region presented in Figure 5.7. The prediction of the wall heat transfer rate is dependent not only on the flow field but also on the accurate evolution of the gradient at the wall. In LES the selective structure function model may not exhibit the correct asymptotic behaviour near the wall, and this will affect the predicted near wall gradients. The model appears to be inadequate near the wall in view of the better agreement with experiment

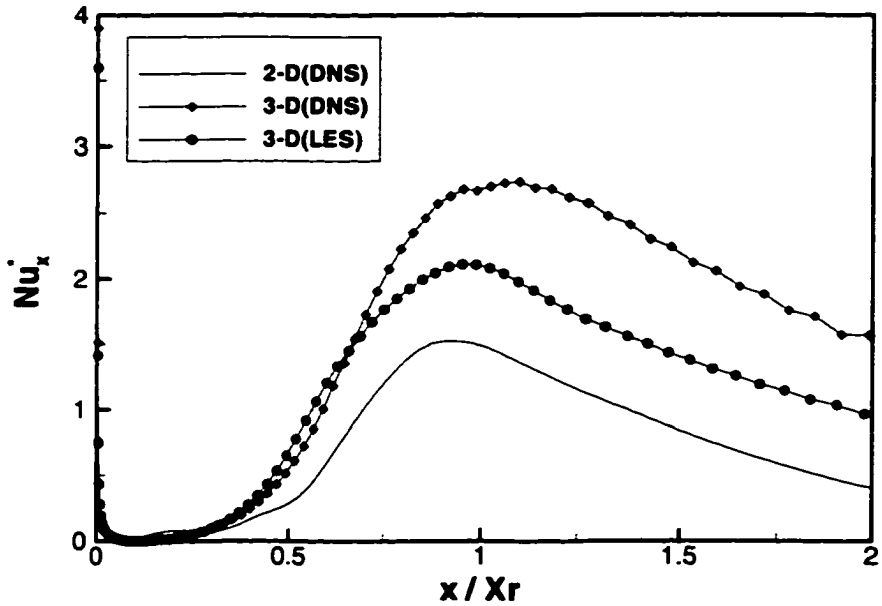

Figure 6.8: The mean Nusselt number distributions in terms of the normalized mean Nusselt number, Nu_x^*

of the DNS value of Nu_r.

The total heat transfer rate over a plate length $L = 2\overline{X}_r$, $q_L = \frac{1}{2L}\int_0^L q_x dx$ is about 2.5% and 6.3% higher for 3-D(LES) and 3-D(DNS), respectively, than in the two-dimensional simulations. The increase is primarily due to the enhancement obtained downstream of reattachment. For instance, 8.7% and 26% of enhancement are found for 3-D(LES) and 3-D(DNS) respectively, when comparing the total heat transfer between $\overline{X}_r$ and $2\overline{X}_r$, i.e. $q_{1-2} = \frac{1}{\overline{X}_r}\int_{\overline{X}_r}^{2\overline{X}_r} q_x dx$. This leads to the idea of optimizing the heat transfer along the plate by reducing the size of the separation bubble and hence the region of low heat transfer rate. This can be accomplished, for example, by triggering earlier transition by introducing an acoustic perturbations upstream of the leading edge [22, 24].

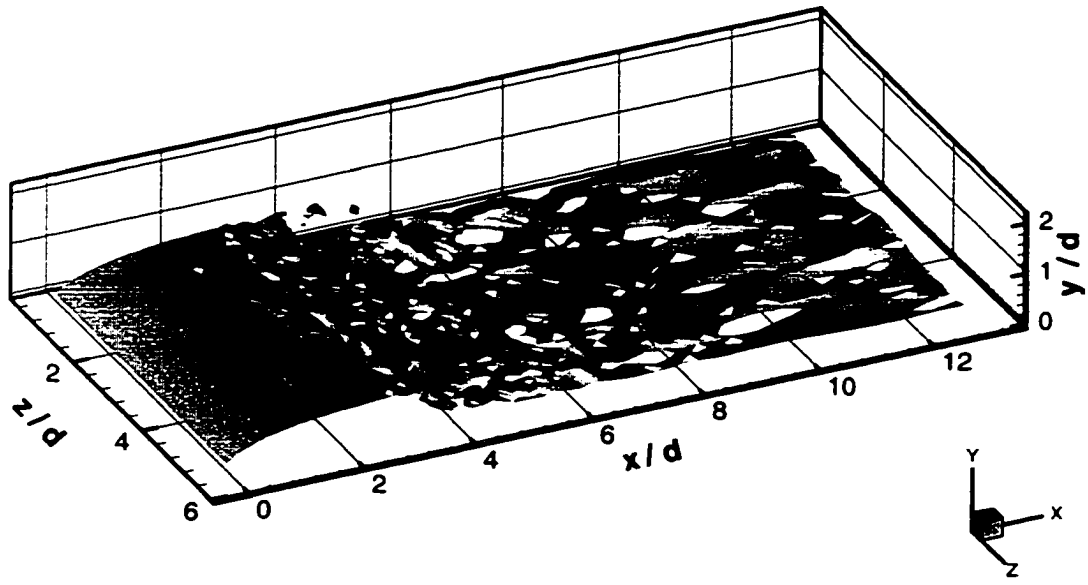

Figure 6.9: Instantaneous thermal structure: 3-D(DNS)

In order to present the heat augmentation clearly, Nu_x is expressed in terms of the normalized mean Nusselt number (Figure 6.8), $Nu_x^* = (Nu_x - Nu_m)/Nu_m$ where Nu_m is the minimum Nusselt number downstream of the leading edge. Compared with 2-D(DNS), the augmentation is approximately 36%, for 3-D(LES), and approximately 75%, for 3-D(DNS). The lower augmentation predicted by the 3-D(LES) is due to the dissipative effect of the subgrid scale model on the smaller scale structures and the associated turbulent mixing.

The instantaneous temperature field from 3-D(DNS) is shown in Figure 6.9. The structure of the temperature field correlates well with the spanwise vorticity presented in Figure 5.11, and exhibits the same two-dimensionality in the first half of the sep-

aration bubble, and rapid amplification of three-dimensional disturbances after the middle of the separation bubble. The formation, close to the surface, of elongated streaks of alternating cold and hot fluid that are characteristic of thermal boundary layers is clearly shown in the reattached flow region after $x/d \simeq 6.0$. These streaks are of course absent in the two-dimensional simulation and hence the lower turbulent mixing and wall heat transfer rates in this case.

6.4 Closing Remarks

The convective heat transfer calculations are performed in two and three-dimensional simulations at low and moderate Reynolds number. The results of two-dimensional simulations at low Reynolds number are in excellent agreement with Djilali [3]. For the unsteady transitional regime ($Re_d = 1{,}000$), the large scale vortices have a strong correlation with the temperature field and the local instantaneous Nusselt number attains a local peak slightly upstream of the vortex. It was found that the large scale vortices play an important role in the transport of energy.

In the three-dimensional simulation, the predicted mean heat transfer rate is further increased. This is due to the break-up process which reduces the large scale structures to smaller three-dimensional structures and results in more turbulent mixing. The non-dimensional temperature profiles exhibit an unusual kink in the separation bubble. The increase of total mean heat transfer coefficient in three-dimensional simulation is found to be less than 7% on the upper surface over a plate length of $L = 2\overline{X}_r$. However, significant enhancement is obtained at a region downstream of the mean reattachment point.

Chapter 7

CONCLUSIONS AND RECOMMENDATIONS

7.1 General Conclusion

The flow and convective heat transfer over a "prototype" separated flow (bluff rectangular plate) have been investigated numerically using direct numerical simulation (DNS) and large eddy simulation (LES). The simulations were performed in two and three-dimensions over a range of Reynolds numbers spanning the laminar, unsteady transitional and fully turbulent regimes. Several subgrid scale models were used for the LES including SFM, SSFM and SM, and their performance were evaluated and compared to the classical turbulence model. All simulations presented in this study were performed over integration times of the order of 30 "flow-through" times to ensure statistically stationary conditions. Such long integration times are required due to the long residency time of flow particles in the recirculating flow region.

In the case of two-dimensional steady and laminar flow, the expected quasi-linear variation of the reattachment length with the Reynolds number is clearly reproduced. The slopes from simulations obtained with both QUICK and CDS discretization schemes are comparable to the experimental data. As the Reynolds number increases, the flow is radically altered due to the onset of unsteadiness. This unsteadiness gradually propagates upstream until the entire separated shear layer becomes unstable. The onset of unsteadiness is delayed when the QUICK scheme is employed.

The two-dimensional unsteady transitional flow simulations ($Re_d = 1,000$) reproduce quantitatively some of the features of the measured mean longitudinal velocity profiles and pressure distributions and provide some insight into the complex and pseudo-periodic patterns of vortex formation, merging and shedding, which occur in the separated and reattaching flow region. Wavelet transform analysis of the simulations yields main characteristic shedding frequency and the dynamic patterns that are in reasonable agreement with observations. The limitations of the two-dimensional simulations are however evident in the large discrepancies in the quantitative prediction of mean velocity profiles, pressure distributions and turbulence statistics. This is due to the artificial constraint of two-dimensionality which prevents the break-up of the strong spanwise structures that occur in the actual flow.

The importance of the inherent three-dimensionality of the flow is clearly shown in the three-dimensional simulations at $Re_d = 1{,}000$. Both DNS and LES were performed at this Reynolds number. There is no marked difference between the two simulations, except in the reattachment region where the dynamics of the flow are slightly different due to insufficient resolution for the DNS. The three-dimensional simulations result in a much more complex flow pattern and capture well the main characteristics such as the large scale (low-frequency) unsteadiness, the oscillation of the instantaneous

reattachment points, and the pseudo-periodic shedding of large scale vortices. During the initial transient period, Kelvin-Helmholtz type instability is clearly identified in the separated shear layer. As the flow progresses in time, break-up of the two-dimensional structure eventually takes place, and results in a flow pattern with much less coherence than in the two-dimensional simulations.

The high Reynolds number, Re_d = 50,000, simulations were all performed using LES. The performance of three subgrid scale models was examined: Smagorinsky (SM), structure function (SFM) and selective structure function (SSFM) model. Throughout the flow, the mean flow and turbulence statistics obtained with SSFM are in very good agreement with the experimental data obtained at the same Reynolds number and blockage ratio in low free stream turbulence. The important role played by large scale unsteadiness is illustrated, for example, in the recovery region where the LES streamwise velocity profiles do not suffer from the commonly observed velocity defect obtained with RANS computation.

The SSFM simulations produce separated shear layer instabilities, dynamical patterns, and structures which are physically consistent with the flow visualization of Saathoff and Melbourne [7]. Both SFM and SM introduce dissipation and delay the break-up and three-dimensionalization of the separated shear layer. Detailed analysis of the flow bring to light the alternating patterns of gradual growth of the separation bubble followed by sudden bursts and vortex shedding from the reattachment zone. The intermittent nature of the flow can also be deduced from the wavelet analysis. The characteristic frequencies obtained from the simulations are in good agreement with spectral analysis of experimental signals. Finally, using the coherent structure identification technique of Jeong and Hussian [94], the large scale structures in the reattachment region are clearly identified as horseshoe vortices.

The bluff plate is a generic module that occurs in many heat transfer calculations. To close this study, the numerical investigation is extended to convective heat transfer at $Re_d = 1{,}000$. The large scale vortices and the three-dimensionality are shown to play an important role in energy transport. The induced rotational motion from large scale vortices both transports heated fluid away from the surface and entrains ambient fluid towards the surface. The intermediate and small three-dimensional structures results in enhanced transport and turbulent mixing. The maximum heat transfer rate is found to occur around the mean reattachment point which is consistent with previous experimental and numerical investigations.

The present investigation shows that LES yields a clear improvement over RANS in predicting mean flow statistics in all regions of the flow field. Furthermore, LES provides insight into the large scale dynamics and associated unsteady features. However, the computational cost of LES is high and, despite the very satisfactory level of agreement, several issues need to be addressed in future work before LES can be used with full confidence for simulating complex separated flows.

7.2 Recommendations for Future Work

- At very high Reynolds number, the portion of turbulent energy constrained in the subgrid scale range becomes increasingly important if affordable grid resolution is maintained. SGS models based on the "Very Large Eddy Simulation" would be very useful in this context and the implementation and assessment of "dynamic" models that account for effects such as backscatter need to also be investigated.

- Alternatives to the wall function and damping function treatment used in this current investigation need to be investigated, and more accurate approaches need to be developed. The fluid dynamics and turbulent transport in the case examined here are largely dominated by the free shear layers and, hence despite the approximate nature of the wall model, the flow is well simulated. However, accurate near-wall modelling is crucial to the reliable prediction of wall shear stress and heat transfer rate, quantities which are in engineering practice of more immediate interest than the flow field. An alternative approach could be the use of an embedded grid, on which a simplified set of parabolized equations, including a turbulence model, is solved separately close to the surface [76].

- In term of numerical requirements, the non-dissipative spatial discretizations such as CDS, are recommended for DNS and LES. However, the CDS is dispersive, and in the vicinity of stagnation regions and sharp geometric discontinuities, such as the leading edge of a bluff rectangular plate or airfoil, the very high gradients introduce numerical oscillations even with carefully designed grid distributions. The procedure used here, i.e. use of mixed QUICK-CDS discretiztaions, was validated but is somewhat ad-hoc. A more systematic procedure that is based on limiters should be investigated.

References

[1] Ota T., Asano Y., and Okawa J. Reattachment length and transition of the separated flow over blunt flat plates. *Bulletin of the JSME*, 24:941–947, 1981.

[2] Lane J.C. and Loehrke R.I. Leading edge separation from a blunt plate at low Reynolds number. *Journal of Fluids Engineering*, 102:494–496, 1980.

[3] Djilali N. Forced laminar convection in an array of stacked plates. *Numerical Heat Transfer. Part A*, 25:393–408, 1994.

[4] Tafti D.K. and Vanka S.P. A numerical study of flow separation and reattachment on a blunt plate. *Physics of Fluids*, A3(7):1749–1759, 1991.

[5] Hillier R. and Cherry N.J. The effect of stream turbulence on separation bubbles. *Journal of Wind Engineering and Industrial Aerodynamics*, 8:49–58, 1981.

[6] Kiya M. and Sasaki K. Free stream turbulence effect on a separation bubble. *Journal of Wind Engineering and Industrial Aerodynamics*, 14:375–386, 1983.

[7] Saathoff P.J. and Melbourne W.H. Effects of free-stream turbulence on surface pressure fluctuations in a separation bubble. *Journal Fluid Mechanics*, 337:1–24, 1997.

[8] Djilali N. and Gartshore I.S. Effect of leading-edge geometry on a turbulent separation bubble. *AIAA Journal*, 30(2):559–561, 1991.

[9] Cherry N.J., Hillier R., and Latour M.E.M.P. The unsteady structure of two-dimensional separated and reattaching flows. *Journal Wind Engineering and Industrial Aerodynamics*, 11:95–105, 1983.

[10] Cherry N.J., Hillier R., and Latour M.E.M.P. Unsteady measurements in a separated and reattaching flow. *Journal of Fluid Mechanics*, 144:130–46, 1984.

[11] Kiya M. and Sasaki K. Structure of a turbulent separation bubble. *Journal of Fluid Mechanics*, 137:83–113, 1983.

[12] Djilali N. and Gartshore I.S. Turbulent flow around a bluff rectangular plate. part I: Experimental investigation. *Journal of Fluids Engineering*, 113:51–59, 1991.

[13] Eaton J.K. and Johnston J.P. Low frequency unsteadiness of a reattaching turbulent shear layer. In *Turbulent Shear Flow 3*, pages 162–170. Springer-Verlag, Berlin, 1982.

[14] Kiya M. and Sasaki K. Structure of large-scale vortices and unsteady reverse flow in the reattaching zone of a turbulent separation bubble. *Journal of Fluid Mechanics*, 154:463–491, 1985.

[15] Tafti D.K. and Vanka S.P. A three-dimensional numerical study of flow separation and reattachment on a blunt plate. *Physics of Fluids*, A3(12):2887–2909, 1991.

[16] Djilali N., Gartshore I.S., and Salcudean M. Turbulent flow around a bluff rectangular plate. part II: Numerical prediction. *Journal of Fluids Engineering*, 113:60–67, 1991.

[17] Mullisen R.S. and Loehrke R.I. A study of flow mechanisms responsible for heat transfer enhancement in interrupted-plate heat exchangers. *Journal of Heat Transfer*, 108:377–385, 1986.

[18] Amon C.H., Majumdar D., Herman C.V., Mayinger F., Mikic B.B., and Sekulic D.P. Numerical and experimental studies of self-sustained oscillatory flows in communicating channels. *International Journal of Heat and Mass Transfer*, 35:3115–3129, 1992.

[19] Hiramatsu M., Ishimasu T., and Ohkouchi T. Numerical analysis of innerfins for intercoolers. *JSME International Journal. Series B*, 35(3):406–412, 1992.

[20] Ota T. and Kon N. Heat transfer in the separated and reattached flow on a blunt flat plate. *Journal of Heat Transfer*, 94:459–462, 1974.

[21] Ota T. and Kon N. Heat transfer in the separated and reattached flow over blunt flat plates : Effects of nose shape. *Journal of Heat Transfer*, 22:197–206, 1979.

[22] Hourigan K., Welch L.W., Thompson M.C., Cooper P.I., and Welsh M.C. Augmented forced convection heat transfer in separated flow around a blunt flat plate. *Experimental Thermal and Fluid Sciences*, 4:182–191, 1991.

[23] Hwang K.S., Sung H.J., and Hyun J.M. Mass transfer measurements from a blunt-faced flat plate in a uniform flow. *International Journal of Heat and Fluid Flow*, 17(2):179–182, 1996.

[24] Hwang K.S., Sung H.J., and Hyun J.M. Flow and mass transfer measurements for a flat plate of finite thickness in pulsating flow. *International Journal of Heat and Mass Transfer*, 41:2827–2836, 1998.

[25] Tafti D.K. Vorticity dynamics and scalar transport in separated and reattached flow on a blunt plate. *Physics of Fluids*, A5(7):1661–1673, 1993.

[26] Sparrow E.M., Kang S.S., and Chuck W. Relation between the points of flow reattachment and maximum heat transfer for regions of flow separation. *International Journal of Heat and Mass Transfer*, 30:1237–1245, 1987.

[27] Djilali N., Gartshore I.S., and Salcudean M. Calculation of convective heat transfer in recirculating turbulent flow using various near-wall turbulence models. *Numerical Heat Transfer. Part A*, 16:189–212, 1989.

[28] Liepman H.W. The rise and fall of ideas in turbulence. *American Scientist*, 67:221–228, 1979.

[29] Bradshaw P. Turbulence: the chief outstanding difficulty of our subject. *Experiments in Fluids*, 16:203–216, 1994.

[30] Tennekes H. and Lumley J.L. *A First Course in Turbulence.* The MIT Press, 1972.

[31] Hussain A.K.M.F. Coherent structure and turbulence. *Journal of Fluid Mechanics*, 173:304–356, 1986.

[32] Brown G.L. and Roshko A. On density effects and large structure in turbulent mixing layers. *Journal of Fluid Mechanics*, 64:775–816, 1974.

[33] J.O. Hinze. *Turbulence.* McGraw-Hill, 1975.

[34] Kline S.J., Reynolds W.C., Schraub F.A., and Runstadler P.W. The structure of turbulent boundary layers. *Journal of Fluid Mechanics*, 30:741–773, 1967.

[35] Moin P. and Kim J. Tackling turbulence with supercomputers. *Scientific American*, 276:62–68, 1997.

[36] Kim J., Moin P., and Moser R. Turbulence statistics in fully developed channel flow at low Reynolds number. *Journal of Fluid Mechanics*, 177:133–166, 1987.

[37] Wang L.P., Chen S., Brasseur J.G., and Wyngaard J.C. Examination of hypothesis in Kolmogorov refined turbulence theory through high-resolution simulations. Part 1. Velocity field. *Journal of Fluid Mechanics*, 309:113–156, 1996.

[38] Ferziger J.H. Higher-level simulation of turbulent flows, Computational methods for turbulent, transonic and viscous flows. J. A Essers, Hemisphere, 1983.

[39] Ferziger J.H. Large eddy simulation. In *Large eddy simulation of complex engineering and geophysical flows*, pages 19–33. Cambridge University Press, New York, 1993.

[40] Lesieur M. and Metais O. New trends in large-eddy simulations of turbulence. *Annual Review of Fluid Mechanics*, 28:45–82, 1996.

[41] Piomeli U., Cabot W.H., Moin P., and Lee S. Subgrid-scale backscatter in turbulent and transitional flows. *Physics of Fluids*, A3(7):1766–1770, 1991.

[42] Comte P. Ducros F. and Lesieur M. Large-eddy simulation of transition to turbulence in a boundary layer developing spatially over a flat plate. *Journal of Fluid Mechanics*, 326:1–36, 1996.

[43] Deardorff J.W. A numerical study of three-dimensional turbulent channel flow at large Reynolds number. *Journal of Fluid Mechanics*, 41:453–480, 1970.

[44] Moin P. and Kim J. Numerical investigation of turbulent channel flow. *Journal of Fluid Mechanics*, 118:341–377, 1982.

[45] Ciofalo M. and Collins M.W. Large-eddy simulation of turbulent flow and heat transfer in plane and rib-roughened channels. *International Journal for Numerical Methods in Fluids*, 15:453–489, 1992.

[46] Arnal M. and Friedrich R. Large eddy simulation of a turbulent flow with separation. In *Turbulent Shear Flow 8*, pages 169–187. Springer-Verlag, Berlin, 1993.

[47] Siveira Neto A., Grand D., Metais O., and Lesieur M. A numerical investigation of the coherent vortices in turbulence behind a backward-facing step. *Journal of Fluid Mechanics*, 256:1–25, 1993.

[48] Moinat P. and Djilali N. Large eddy simulations of separated flows: Effect of inlet conditions. In *Proceeding of the CFD 96, Fourth Annual Conference of the CFD Society of Canada*, pages 255–262, Ottawa, 1996.

[49] Ghosal S., Lund T., Moin P., and Akselvoll K. A dynamic localization model for large-eddy simulation of turbulent flow. *Journal of Fluid Mechanics*, 286:229–255, 1995.

[50] Werner H. and Wengle G. Large eddy simulation of turbulent flow over and around a cube in a plate channel. In *Turbulent Shear Flow 8*, pages 155–168. Springer-Verlag, Berlin, 1993.

[51] Kogagi T., Kobayashi T., and Taniguchi N. Large eddy simulation of flow around a rectangular cylinder. *Fluid Dynamics Research*, 20:11–24, 1997.

[52] Rodi W., Ferziger J.H., Breuer M., and Pourquie M. Status of large eddy simulation: Results of a workshop. *Journal of Fluids Engineering*, 19:248–262, 1997.

[53] Yang K.S. and Ferziger J.H. Large-eddy simulation of turbulent obstacle flow using a dynamic subgrid-scale model. *AIAA Journal*, 31(8):1406–1413, 1993.

[54] Breuer M. Large-eddy simulation of the subcritical flow past a circular cylinder: Numerical and modelling aspects. *International Journal for Numerical Methods in Fluids*, 28:1281–1302, 1998.

[55] Hassan Y.A., Pruitt J.M., and Steininger D.A. A perspective on large eddy simulation of problems in the nuclear industry. *Nuclear Technology*, 112:324–330, 1995.

[56] Piomeli U., Moin P., and Ferziger J.H. Model consistency in large eddy simulation of turbulent channel flows. *Physics of Fluids*, 31(7):1884–1891, 1988.

[57] Moinat P. and Djilali N. On the application of large eddy simulations to high-Reynolds number separated flow. Technical report, University of Victoria, Victoria, Canada, 1998.

[58] Germano M., Piomelli U., Moin P., and Calbot W.H. A dynamic subgrid-scale eddy viscosity model. *Physics of Fluids*, A3(7):1760–1765, 1991.

[59] Lilly D.K. A proposed modification of Germano subgrid-scale closure method. *Physics of Fluids*, A4(3):633–634, 1992.

[60] Speziale C.G. Turbulence modeling for time-dependent RANS and VLES:A review. *AIAA Journal*, 36(2):173–184, 1998.

[61] Reynolds O. On the dynamical theory of incompressible viscous fluids and the determination of the criterion. *Philosophical Transactions of Royal Society of London, Series A*, 186:123–164, 1895.

[62] Nallasamy M. Turbulence models and their applications to the prediction of internal flows: A review. *Computers and Fluids*, 15:151–194, 1987.

[63] Ferziger J.H. Approaches to turbulent flow computation: Application to flow over a obstacle. *Journal of Wind and Industrial Aerodynamics*, 35:1–19, 1990.

[64] Launder B.E. Second-moment closure: present... and future? *International Journal of Heat and Fluid Flow*, 10(4):282–299, 1989.

[65] Hanjalic K., Launder B.E., and Schiestel R. Multiple time scale in turbulent transport modeling. In *Turbulent Shear Flow 2*, pages 36–49. Springer-Verlag, 1980.

[66] Kim S.W. Calculation of divergent channel flows with multiple time scale turbulence models. *AIAA Journal*, 29:547–554, 1991.

[67] Zeidan E. and Djilali N. Three-dimensional computational of separated flow around surface mounted prismatic obstacles with a multi-scale turbulence model. *Computational Fluid Dynamics Journal*, 7(1):27–41, 1998.

[68] F.M. White. *Viscous Fluid Flow.* McGraw-Hill, second edition, 1991.

[69] Leonard A. Energy cascade in large-eddy simulations of turbulent fluid flows. *Advances in Geophysics*, 18(A):237–248, 1974.

[70] Schumann U. Subgrid scale model for finite difference simulations of turbulent flows in plane channel and annuli. *Journal of Computational Physics*, 18:376–404, 1975.

[71] Clark R.A., Ferziger J.H., and Reynolds W.C. Evaluation of subgrid-scale models using an accurately simulated turbulent flow. *Journal of Fluid Mechanics*, 91:1–16, 1979.

[72] Smagorinsky J. General circulation experiments with the primitive equations. *Monthly Weather Review*, 91:99–164, 1963.

[73] Lilly D.K. The representation of small-scale turbulence in numerical simulation experiments. In *Proceedings IBM Scientific Computing Symposium Enviromental Sciences*, pages 195–210, New York, 1967. IBM.

[74] Van Driest E.R. On turbulent flow near a wall. *Journal of Aeronautical Sciences*, 23:1007–1011, 1956.

[75] Piomeli U. and Zang T.A. Large eddy simulation of transitional channel flow. *Computer Physics Communications*, 65(1/3):224–230, 1991.

[76] Balaras E., Benocci C., and Piomelli U. Two-layer approximate boundary conditions of large-eddy simulations. *AIAA Journal*, 34(6):1111–1119, 1996.

[77] Piomelli U., Ferziger J., and Moin P. New approximate boundary conditions for large eddy simulations of wall-bounded flows. *Physics of Fluids*, A1(6):1061–1068, 1989.

[78] Grand D., Coulon N., Magnaud J.P., and Villand M. Computation of flows with distributed resistance and heat sources. In Iwasa Y., Tamai N., and Wada A., editors, *Proceeding of International Symposium on Refined Flow Modelling and Turbulence Measurements*, Tokyo, Japan, 1988. Universal Academic Press.

[79] Patankar S.V. *Numerical Heat Transfer and Fluid Flow.* Taylor and Francis, 1980.

[80] Ferziger J.H. and Peric M. *Computational Methods for Fluid Dynamics.* Springer-Verlag, 1996.

[81] Leonard B.P. A stable and accurate convective modeling procedure based on quadratic upstream interpolation. *Computer Methods in Applied Mechanics and Engineering*, 19:59–98, 1979.

[82] Leonard B.P. Order of accuracy of QUICK and related convection-diffusion schemes NASA Technical Memorandum 106402. Technical report, Institute for Computational Mechanics in Propulsion, Lewis Research Center, Ohio, 1993.

[83] Mittal R. and Moin P. Suitability of upwind-biased finite difference schemes for large-eddy simulation of turbulent flow. *AIAA Journal*, 35(8):1415–1417, 1997.

[84] Williamson J.H. Low-storage Runge-Kutta schemes. *Journal of Computational Physics*, 35:48–56, 1980.

[85] Kim J. and Moin P. Application of a fractional-step methods to incompressible Navier-Stokes equations. *Journal of Computational Physics*, 59:308–323, 1985.

[86] Golub G.H. and Van Loan C.F. *Matrix Computations.* The Johns Hopkins University Press, 3 edition, 1996.

[87] Van Der Vorst H.A. and Dekker K. Conjugate gradient type methods and preconditioning. *Journal of Computational and Applied Mathematics*, 24:73–87, 1988.

[88] Kaasschieter E.F. Precontioned conjugate gradients for solving singular systems. *Journal of Computational and Applied Mathematics*, 24:265–275, 1988.

[89] Farge M. Wavelet transforms and their applications to turbulence. *Annual Review of Fluid Mechanics*, 24:395–457, 1992.

[90] Arnal M. and Friedrich R. On the effects of spatial resolution and subgrid-scale modeling in the large-eddy simulation of a recirculating flow. In *Proceeding of the 9th GAMM - Conference on Numerical Methods in Fluid Mechanics*, Lausanne, 1991.

[91] Ferziger J.H. Direct and large-eddy simulation: Application to complex and stratified flows. In *Proceeding of the CFD 97 conference, Fifth Annual Conference of the CFD Society of Canada*, pages 1–14, Victoria, 1997.

[92] Le H., Moin P., and Mahesh K. Direct numerical simulation of turbulent flow over a backward-facing step. *Journal of Fluid Mechanics*, 330:349–374, 1998.

[93] Bernal L.P. and Roshko A. Streamwise vortex structure in plane mixing layers. *Journal of Fluid Mechanics*, 170:499–525, 1986.

[94] Jeong J. and Hussain F. On the identification of a vortex. *Journal of Fluid Mechanics*, 285:69–94, 1995.

[95] Jeong J., Hussain F., Schoppa W., and Kim J. Coherent structures near the wall in a turbulent channel flow. *Journal of Fluid Mechanics*, 332:185–214, 1997.

[96] Shah R.K. and London A.L. Laminar flow force convection in ducts. *Advances of Heat Transfer,suppl. 1*, pages 153–189, 1978.

[97] Liandrat J. and Marlet-Bailly. The wavelet transform: Some applications to fluid dynamics and turbulence. *European Journal of Mechanics, B/Fluids*, 9(1):1–19, 1990.

[98] Higushi H., Lewalle J., and Crane P. On the structure of two-dimensional wake behind a pair of flat plates. *Physics of Fluids*, 6(1):297–305, 1994.

[99] Lewalle J. Wavelet analysis of experimental data: Some methods and their underlying physics. In *25th AIAA Fluid Dynamics Conference*, pages 1–10, Colorado, 1994.

Appendix A

The Discretized Governing Equations

Substituting the source terms from Table 3.2 into equation (3.4), the discretized momentum equations over each control volumes are obtained from the volume and surface approximations (3.5) and (3.6).

x-momentum equation

$$\begin{aligned}\frac{\partial \hat{U}}{\partial t} = &-\frac{1}{\rho}\frac{[P]^{east} - [P]^{west}}{dxp} \\ &+\frac{\left[\nu\frac{\partial U}{\partial x} + \nu_t(\frac{\partial U}{\partial x} + \frac{\partial U}{\partial x}) - UU\right]^{east} - \left[\nu\frac{\partial U}{\partial x} + \nu_t(\frac{\partial U}{\partial x} + \frac{\partial U}{\partial x}) - UU\right]^{west}}{dxp} \\ &+\frac{\left[\nu\frac{\partial U}{\partial y} + \nu_t(\frac{\partial U}{\partial y} + \frac{\partial V}{\partial x}) - VU\right]^{north} - \left[\nu\frac{\partial U}{\partial y} + \nu_t(\frac{\partial U}{\partial y} + \frac{\partial V}{\partial x}) - VU\right]^{south}}{dy} \\ &+\frac{\left[\nu\frac{\partial U}{\partial z} + \nu_t(\frac{\partial U}{\partial z} + \frac{\partial W}{\partial x}) - WU\right]^{top} - \left[\nu\frac{\partial U}{\partial z} + \nu_t(\frac{\partial U}{\partial z} + \frac{\partial W}{\partial x}) - WU\right]^{bottom}}{dz}\end{aligned} \tag{A.1}$$

y-momentum equation

$$\frac{\partial \hat{V}}{\partial t} = -\frac{1}{\rho}\frac{[P]^{north} - [P]^{south}}{dyp} + \frac{\left[\nu\frac{\partial V}{\partial x} + \nu_t(\frac{\partial U}{\partial y} + \frac{\partial V}{\partial x}) - UV\right]^{east} - \left[\nu\frac{\partial V}{\partial x} + \nu_t(\frac{\partial U}{\partial y} + \frac{\partial V}{\partial x}) - UV\right]^{west}}{dx} + \frac{\left[\nu\frac{\partial V}{\partial y} + \nu_t(\frac{\partial V}{\partial y} + \frac{\partial V}{\partial y}) - VV\right]^{north} - \left[\nu\frac{\partial V}{\partial y} + \nu_t(\frac{\partial V}{\partial y} + \frac{\partial V}{\partial y}) - VV\right]^{south}}{dyp} + \frac{\left[\nu\frac{\partial V}{\partial z} + \nu_t(\frac{\partial V}{\partial z} + \frac{\partial W}{\partial y}) - WV\right]^{top} - \left[\nu\frac{\partial V}{\partial z} + \nu_t(\frac{\partial V}{\partial z} + \frac{\partial W}{\partial y}) - WV\right]^{bottom}}{dz} \quad \text{(A.2)}$$

z-momentum equation

$$\frac{\partial \hat{W}}{\partial t} = -\frac{1}{\rho}\frac{[P]^{top} - [P]^{bottom}}{dzp} + \frac{\left[\nu\frac{\partial W}{\partial x} + \nu_t(\frac{\partial U}{\partial z} + \frac{\partial W}{\partial x}) - UW\right]^{east} - \left[\nu\frac{\partial W}{\partial x} + \nu_t(\frac{\partial U}{\partial z} + \frac{\partial W}{\partial x}) - UW\right]^{west}}{dx} + \frac{\left[\nu\frac{\partial W}{\partial y} + \nu_t(\frac{\partial V}{\partial z} + \frac{\partial W}{\partial y}) - VW\right]^{north} - \left[\nu\frac{\partial W}{\partial y} + \nu_t(\frac{\partial V}{\partial z} + \frac{\partial W}{\partial y}) - VW\right]^{south}}{dy} + \frac{\left[\nu\frac{\partial W}{\partial z} + \nu_t(\frac{\partial W}{\partial z} + \frac{\partial W}{\partial z}) - WW\right]^{top} - \left[\nu\frac{\partial W}{\partial z} + \nu_t(\frac{\partial W}{\partial z} + \frac{\partial W}{\partial z}) - WW\right]^{bottom}}{dzp} \quad \text{(A.3)}$$

The continuity and energy equations are also summarized as,

energy equation

$$\frac{\partial \hat{T}}{\partial t} = \frac{\left[(\alpha + \alpha_t)\frac{\partial T}{\partial x} - TU\right]^{east} - \left[(\alpha + \alpha_t)\frac{\partial T}{\partial x} - TU\right]^{west}}{dx} + \frac{\left[(\alpha + \alpha_t)\frac{\partial T}{\partial y} - TV\right]^{north} - \left[(\alpha + \alpha_t)\frac{\partial T}{\partial y} - TV\right]^{south}}{dy} + \frac{\left[(\alpha + \alpha_t)\frac{\partial T}{\partial z} - TW\right]^{top} - \left[(\alpha + \alpha_t)\frac{\partial T}{\partial z} - TW\right]^{bottom}}{dz} \quad \text{(A.4)}$$

continuity equation

$$\frac{[\hat{U}]^{east} - [\hat{U}]^{west}}{dx} + \frac{[\hat{V}]^{north} - [\hat{V}]^{south}}{dy} + \frac{[\hat{W}]^{top} - [\hat{W}]^{bottom}}{dz} = 0 \qquad \text{(A.5)}$$

Appendix B

The Wavelet Transform Analysis

The one-dimensional continuous wavelet transform is a linear integral transform that associates a function $Wf(s,\tau)$ with a signal $g(t)$ and $\psi^*_{s,\tau}$(t), according to the definition [89],

$$Wf(s,\tau) = \int_{-\infty}^{\infty} \psi^*_{s,\tau}(t)g(t)dt \tag{B.1}$$

and

$$\psi^*_{s,\tau}(t) = (\frac{1}{\sqrt{s}})\psi(\frac{t-\tau}{s}) \tag{B.2}$$

where $Wf(s,\tau)$ is the wavelet transform function and $g(t)$ is a time series signal. $\psi(t)$ is the basic analyzing wavelet (also refereed to as "mother wavelet"). Stretching (or dilating) by the scale **s** and translating with location τ, this mother wavelet yields a "daughter wavelet", $\psi_{s,\tau}(t)$. The asterisk $(*)$ in equation B.2, denotes its complex conjugate. The normalizing constant $(\frac{1}{\sqrt{s}})$ is chosen so that the energy in the dilated wavelet function is the same for all scales.

The wavelet energy spectrum can be defined as a distribution of the energy in the signal $g(t)$ over the wavelet scales. This form allows the energy in each wavelet scale to be interpreted in a manner analogous to the Fourier energy spectrum.

$$E(s) = \int_{-\infty}^{\infty} |Wf(s,\tau)|^2 d\tau \tag{B.3}$$

In this study, two wavelet families are selected for the mother wavelet, the Morlet and the Mexican hat wavelet. The Morlet wavelet provides good spectral accuracy and is useful for detecting periodicity in the signal. Information about both amplitude and phase can be extracted since the wavelet is complex. The Morlet wavelet shown in Figure B.1 together with its Fourier transform, is given by,

$$\psi(t) = e^{-t^2/2} e^{-i\omega_o t}, \qquad \omega_o \geq 5 \tag{B.4}$$

The Mexican hat is the classical second derivative of the Gaussian function and is defined as,

$$\psi(t) = (t^2 - 1)e^{-t^2/2} \tag{B.5}$$

The Mexican hat wavelet is good for detecting local increase or decrease of the signal and the localization of inflexion points (edges or the discontinuity point). The Mexican hat wavelet is shown in Figure B.2 together with its Fourier transform

Wavelet analysis is based on the concepts of time and duration rather than frequency (f), which, in this case, is a secondary quantity, obtained from the repetition of particular events. For quasi-periodic events, a frequency can however be calculated by using the relationship between the equivalent Fourier period (λ_p) and the wavelet scale (s).

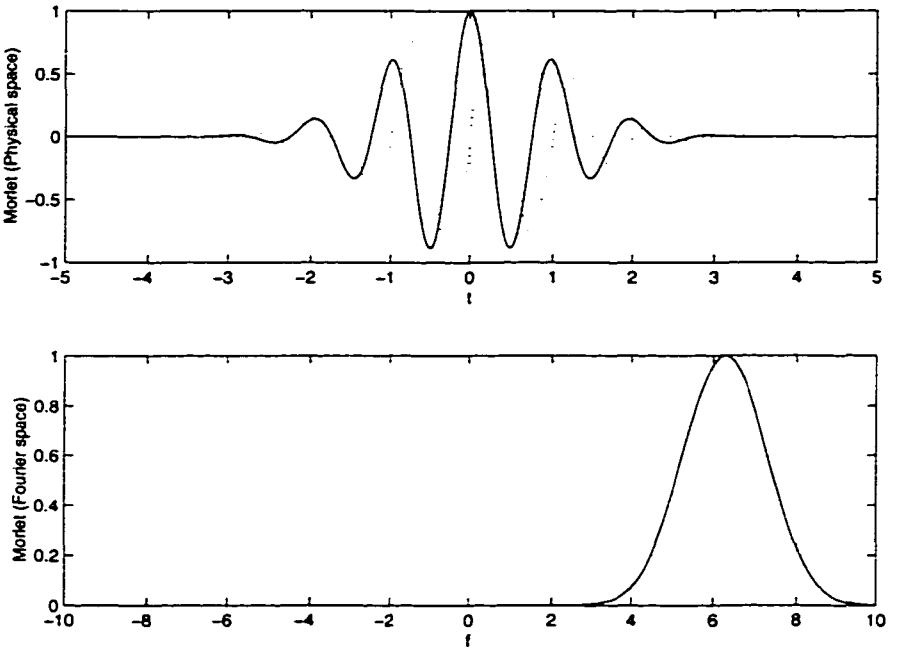

Figure B.1: (top) The Morlet wavelet with $\omega_o = 2\pi$, solid line for real part and dot-dashed line for imaginary part; (bottom) the spectrum of Morlet wavelet

Morlet wavelet:

$$\lambda_p = \frac{4\pi s}{\omega_o + \sqrt{2 + \omega_o^2}} \tag{B.6}$$

Mexican hat wavelet:

$$\lambda_p = \frac{4\pi s}{m + 0.5} \tag{B.7}$$

In this investigation, the Morlet wavelet is used with $\omega_o = 2\pi$, giving $\lambda_p = 0.988s$. This indicates that for the Morlet wavelet with $\omega_o = 2\pi$, the wavelet scale is nearly equivalent to the Fourier period. However, the Fourier period is about 4 times the

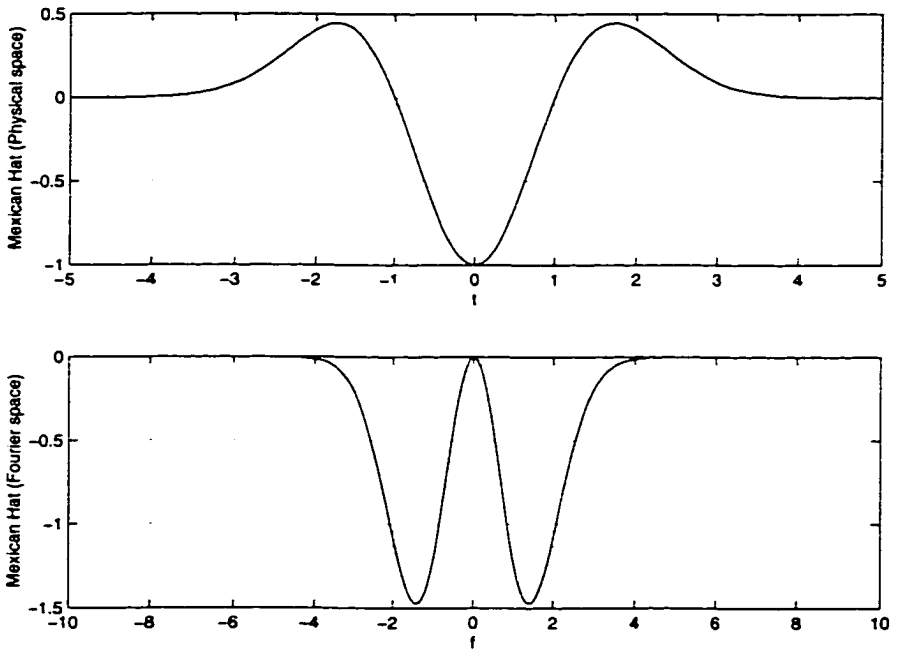

Figure B.2: (top) The Mexican hat wavelet; (bottom) the spectrum of Mexican hat wavelet

wavelet scale for the Mexican hat wavelet ($m = 2$ for the Mexican hat wavelet). Further details on the theoretical basis of wavelet analysis and possible applications are avaliable in Ref. [89, 97, 98, 99]. The wavelet analysis was performed using a Matlab toolbox in which the Morlet wavelet is avaiable. The Mexican wavelet was implemented by the author into Matlab.